A Study of Anthraquinone Structural Changes for Aqueous Redox Flow Ballery Materials

HARVARD UNIVERSITY
Graduate School of Arts and Sciences

DISSERTATION ACCEPTANCE CERTIFICATE

The undersigned, appointed by the

Department of

have examined a dissertation entitled

A Study of Anthraquinone Structural Changes for Aqueous Redox Flow Battery Materials

presented by Emily Faye Kerr

candidate for the degree of Doctor of Philosophy and hereby certify that it is worthy of acceptance.

Signature _____

Typed name: Prof. Roy G. Gordon

Signature _____

Typed name: Prof. Michael J. Aziz

Signature _____

Typed name: Prof. Eric N. Jacobsen

Date: September 5, 2022

A Study of Anthraquinone Structural Changes for Aqueous Redox Flow Battery Materials

A dissertation presented

by Emily Faye Kerr

to

the Department of Chemistry and Chemistry and Chemical Biology

in partial fulfillment of the requirements for the degree of

Doctor of Philosophy

in the subject of Chemistry

Harvard University

Cambridge, Massachusetts

September

2022

Dissertation Advisor: Professor Roy Gordon Emily Faye Kerr

A Study of Anthraquinone Structural Changes for Aqueous Redox Flow Battery Materials

Abstract

The transition away from fossil-fuel-based electricity production is critical for cutting the emissions of climate change causing carbon dioxide emissions. Renewable energy sources, including solar and wind energy, are now cost-competitive with fossil fuels. This has generated serious interest in energy storage technologies to help manage the intermittency of these energy sources. Redox flow batteries provide a promising technology for providing grid-scale energy storage.

Chapter 1 describes the current state of renewable energy and energy storage in electricity generation. The design and current state of redox flow batteries are discussed.

Chapter 2 details the synthesis and characterization of a new anthraquinone, 2,6-D2PEAQ. A novel method of installing branched side chains to improve the aqueous solubility of anthraquinones is presented. Cell studies demonstrating a daily capacity fade of <0.02%/day are described.

Chapter 3 describes the properties of the anthraquinone BEAQ, which forms a gel in aqueous solutions rather than the high-concentration homogenous solutions seen from similarly structured anthraquinones. The characterization of the gel is described. A potential application in gel batteries is presented.

Chapter 4 uses a simpler single branched-chain substituted anthraquinone (2-2PEAQ) to study the decomposition and potential regeneration of highly-soluble anthraquinones. The

synthesis and characterization of 2-2PEAQ are discussed and cell testing to give a fade rate of <0.05%/day is presented. The capacity fade was decreased to <0.01%/day through the use of electrochemical regeneration strategies in the cell. Finally, the effect of the substitution position of an ether-linked side chain on the anthraquinone is explored by comparing the performance of 2-2PEAQ to the isomer 1-2PEAQ in cell testing and through post-cycling analysis.

Chapter 5 describes chemical characterization studies of four commercial anthraquinones, including cyclic voltammetry, thermal decomposition, and solubility measurements. The limitations that would need to be overcome to make these anthraquinones good candidates for further study are described.

Table of Contents

Table of Figures

Acknowledgments

I am writing these acknowledgments last of all the sections of this thesis, but they were the section I started mentally planning first. It has taken the efforts and generosity of a great many people for me to reach this point, and I am grateful for the opportunity to thank many of them here.

I would like to offer my sincerest gratitude to my advisor, Roy Gordon, who has created a welcoming lab where I have always had the opportunity to learn new skills alongside curious, dedicated, and passionate people. Roy has been a dedicated advisor who has modeled a keen interest in applying science to address real problems, a deep curiosity about a huge range of topics, and an enduring concern for the happiness and well-being of his students.

I would also like to thank Dr. Michael Aziz, whose lab has been instrumental collaborators throughout the flow battery project. Mike has modeled a deep understanding of the fundamental principles underlying our experiments, an insistence on careful and well-thought-out experimental design, and clear and careful scientific communication.

To round out my thesis committee, I would like to thank Eric Jacobsen for his feedback, advice, and expertise over the past few years.

Among my lab mates, there have been too many who have provided advice, expertise, and companionship for me to thank each of you to thank by name, but I would like to specifically thank Dr. Zhijiang Tang, Dr. Kiana Amini, Dr. Yan Jing, Thomas George, and Daniel Pollack, with whom I have worked particularly closely or for a particularly long time, for their extensive experimental help, advice, and companionship over the past few years. Thanks is

also owed to Teri Howard and Patricia McGarry, our lab admins who were instrumental to keeping everything running and providing unceasing moral and logistical support.

I would also like to acknowledge those without whom I would never have made it to graduate school in the first place. Again, there are far too many teachers, family members, and friends in this category to list individually, but I would like to particularly thank the Chemistry department at Xavier University, my undergraduate institution for providing a strong grounding in my chemical education. Particularly noteworthy are Dr. Supaporn Kradtap Hartwell and Dr. Richard Mullins, both of whom have continued to provide me advice, mentorship, and opportunities long after my undergraduate graduation. Also of note is Ms. Helena Louzonis, who was the first to tell me I could excel in chemistry back in AP Chemistry (Please be assured that I did, eventually, memorize my polyatomic ions).

Last, but certainly not least, I would like to thank my family, particularly my mom and dad who have always modelled a curiosity about the universe and have provided a constant refuge over the past few years. Thanks also to my siblings: Sam, Ian, Jeff, and Zoe, who have never doubted in my ability, have tried to understand what I've been working on over the course of graduate school, and have always been willing partners for a weekend adventure.

For those who I do not have the space to list by name but who have nonetheless taught me, been taught by me, researched with me, sailed with me, camped with me, fenced with me, and otherwise been an important part of my life, I leave my appreciation for the multitude of acts of encouragement and support that made it possible to write this thesis.

Chapter 1 Introduction

1.1 The current state of renewable energy and energy storage capacity

The threats posed by climate change require a global transition to energy production that does not result in the production of greenhouse gases like carbon dioxide. A significant portion of current carbon dioxide emissions is the result of electricity production, which the EPA estimates produce 25% of the CO_2-equivalents the United States emits.[1] Fortunately, the cost of installing solar or wind power has decreased significantly over the past several decades and the cost of these technologies is now competitive with burning coal or natural gas.[2] Climate think tank Ember estimates that in 2021, 10% of electricity was generated by either solar or wind power.[3] The annual installation of both solar and wind energy continues to grow rapidly as the cost per kilowatt hour continues to decline (Figure 1.1). As the solar and wind industries have grown, the annual installations of these low-carbon energies have grown at an increasing rate while costs continue to decrease and are now competitive with fossil fuel sources of electricity.[2]

a.

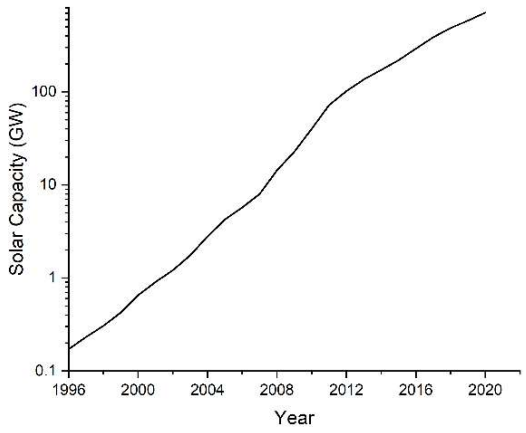

b.

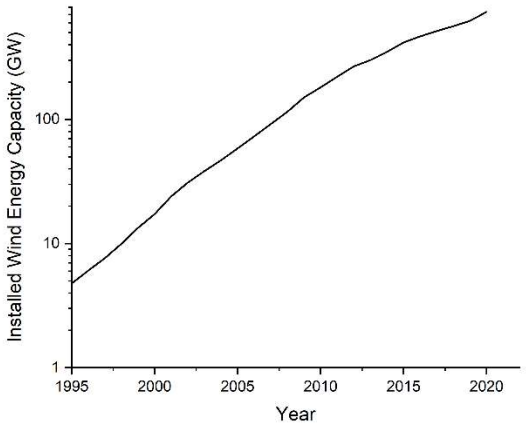

c.

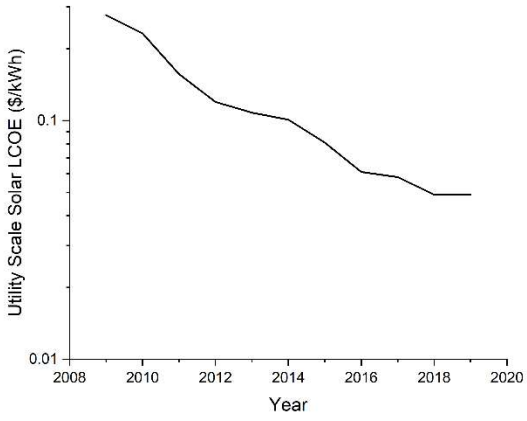

d.

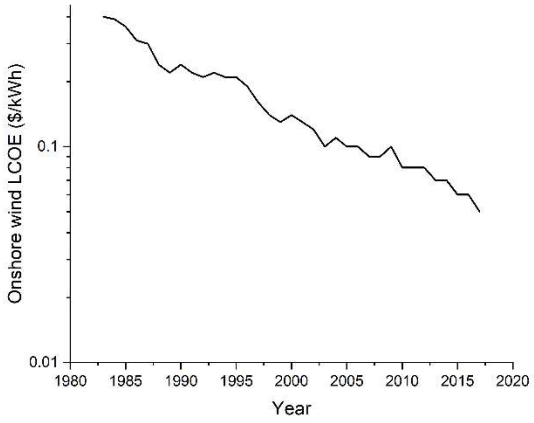

Figure 1.1: Cost and installed capacity of renewable energy. a. Gigawatts of solar power installed internationally from 1996 to 2020.[4] b. Installed wind capacity worldwide since 1995 including both onshore and offshore wind turbines.[4] c. The worldwide average cost per kWh for 100 mW fixed tilt utility-scale solar installations from 2009-2020.[5] d. Cost per kWh of onshore wind from 1983 to 2016.[6] Data for graphs a,b, and d originally compiled by "Our World in Data."[7]

However, while solar and wind energy are providing increasingly inexpensive electricity, both forms of renewable energy are challenged by their inherent intermittency. Unlike a fossil-fuel-powered power plant, which can be rapidly turned on or off to meet electricity demand, solar and wind installations only produce electricity in the presence of sunlight or appropriate wind speeds. Figure 1.2 shows the power produced by a wind installation (blue top graph), solar (red, middle graph), and the power demand by consumers (green, bottom graph).

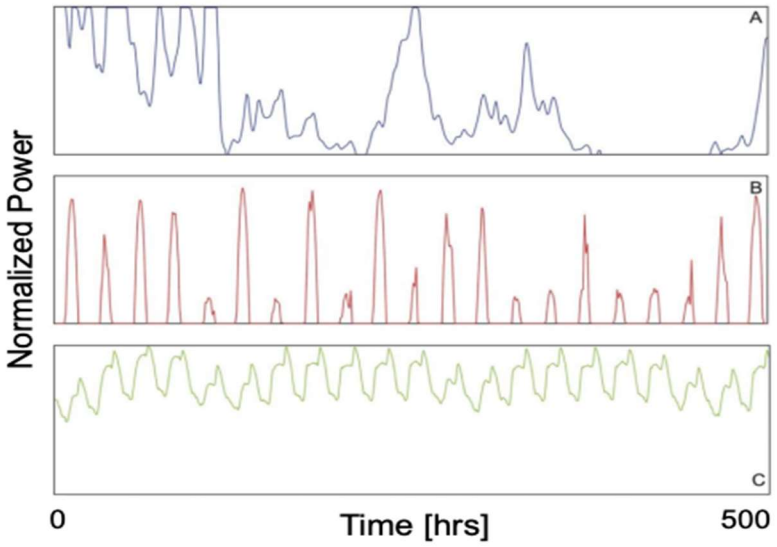

Figure 1.2: Intermittency of energy production compared to energy demand. The top blue curve shows the normalized power produced by a 1.5 MV wind turbine in Wilhelminadorp, Netherlands. The middle red curve shows solar PV power produced by an installation in Boston, Massachusetts with periodic peaks and shifts occurring during day and night respectively, and periods of lower production occurring on cloudy or rainy days. The bottom green trace shows electricity demand over three weeks in the UK that follows a periodic pattern through each day and week.[8]

As intermittent sources of energy become more abundant, energy storage can help match the supply to the demand. Today the energy storage landscape is dominated by pumped hydropower, which was estimated to make up about 93% of utility-scale energy storage in 2021.[9] However pumped hydroelectric storage is geographically limited to areas with appropriate elevation differences and is not a viable solution to meet the increasing needs of energy storage.

The use of electrochemical energy storage has been expanding. This is driven largely by the rapidly decreasing cost of lithium-ion batteries, which is projected to continue.[10] While lithium-ion batteries boast impressive energy density, they also have significant drawbacks for grid-scale use. Despite ongoing research into new cathode materials, they're reliant on metals that can be expensive, lacking in earth abundance, and plagued by sociopolitical challenges.[11] They are also at risk of thermal runaway processes that pose a danger due to the flammable electrolytes in the battery.[12] Finally, the power and energy of a lithium-ion battery are coupled to each other – requiring multiple battery packs to be linked in parallel for high-energy projects. This leads to an increased cost for large lithium-ion installations.

While lithium-ion batteries are currently the predominant method of electrochemical energy storage for grid-scale applications, comprising over 90% of both power and energy installation over the last decade, alternative battery designs are generating increased interest. In the last few years, annual installations of flow batteries have begun to increase, although they still make up a small total amount of new storage installations with 33 MWh being installed between 2017 and 2020 in the United States (Figure 1.3).[13]

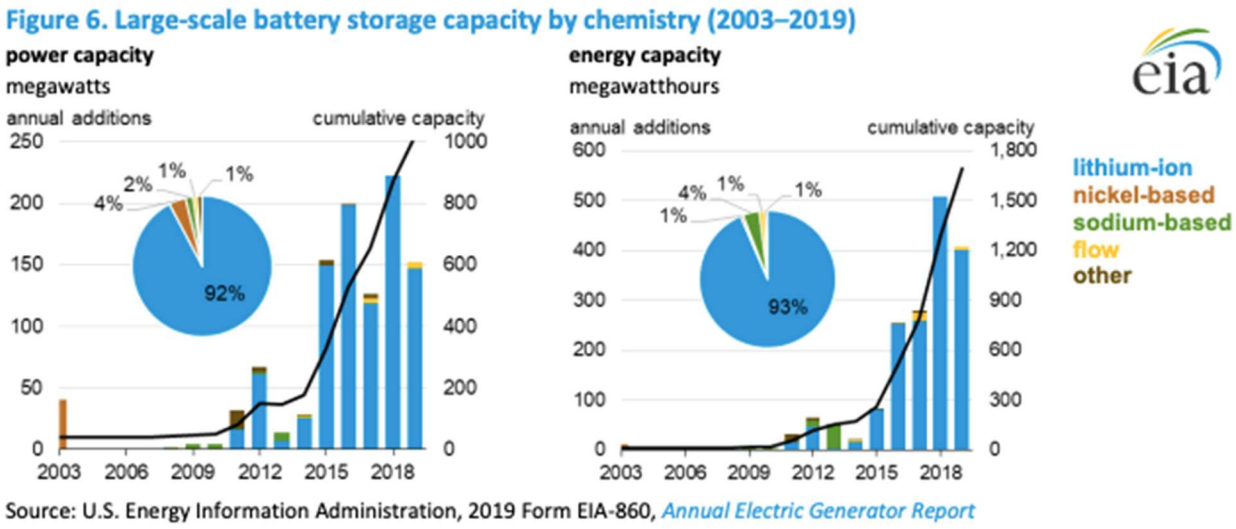

Figure 1.3: Cumulative installed capacity of battery technologies. However, flow batteries have begun to see commercial installations in recent years. Image credit to the Department of Energy.[14]

1.2 Introduction to redox flow batteries

Redox flow batteries function by separating the electroactive material into two separate tanks. The electroactive components are dissolved either in water or an organic solvent, although water is often used to take advantage of its high conductivity with dissolved salts, low cost, and excellent safety profile. To charge the battery, the liquid in these tanks can be pumped through to an electrode where the negolyte (the electrolyte with a more negative potential) is reduced and the posolyte (the electrolyte with a more positive potential) is oxidized before being pumped back to their tanks. When it is necessary to extract energy from the battery, the material can then be pumped from the tanks to the electrode where the negolyte is oxidized and the posolyte reduced. To keep the electroactive species separated from each other, a membrane or other separator is used. Often, this will be an ion exchange membrane to slow the rate at which

charged species in the electrolyte can cross to the other side of the battery. The basic structure of a redox flow battery is shown in Figure 1.4.

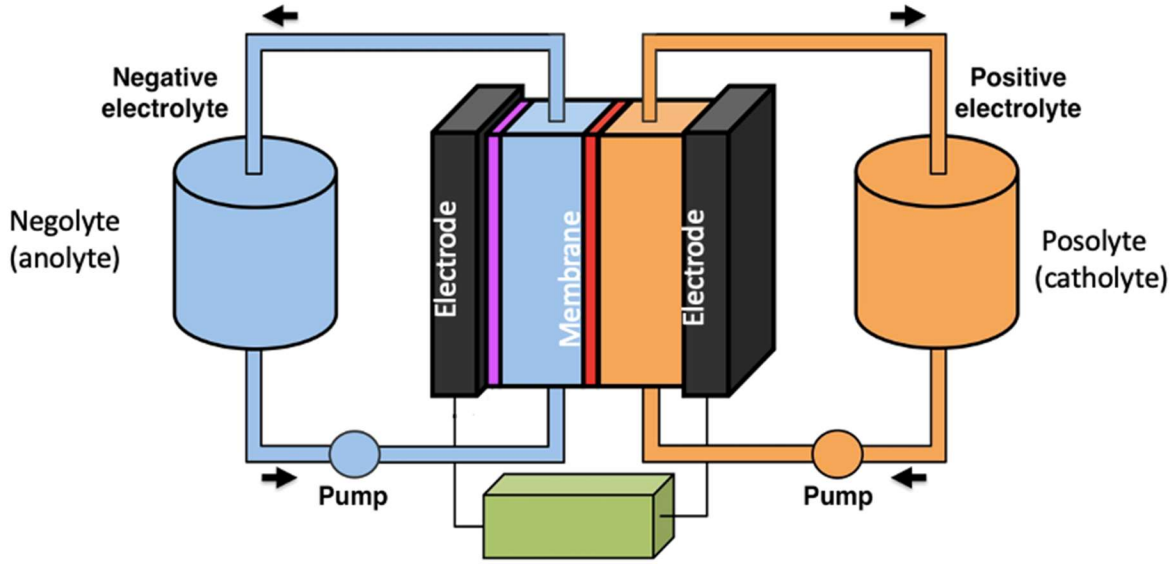

Figure 1.4: Diagram of a redox flow battery. Image modified from Wikimedia user Earth-Rare.[15]

Because the architecture of redox flow batteries stores the electroactive materials in reservoirs separate from the battery stack containing the electrodes, membranes, and current collectors, it is possible to decouple power and energy. Energy can be increased by increasing the tank size without re-engineering and increasing the cost of the battery stack itself. This leads to redox flow batteries becoming potentially less expensive than solid-electrode batteries for larger installations as the cell stack becomes a smaller component of the cost of the flow battery relative to the cost of the electrolyte (Figure 1.5)

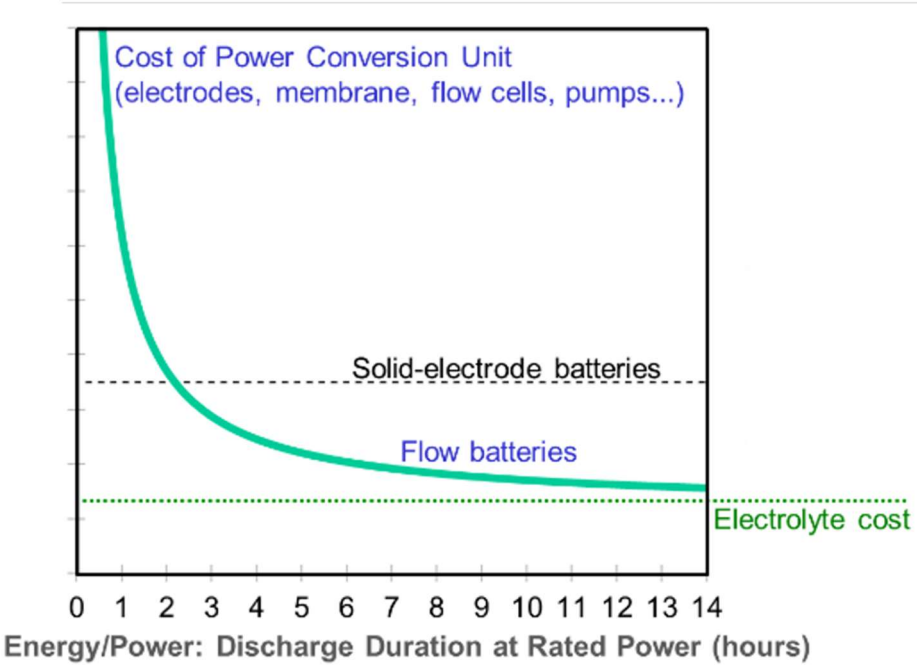

Figure 1.5: Cost of flow vs. solid electrode batteries as a function of discharge duration.[16]

The most common electrolytes in redox flow batteries are vanadium compounds. Vanadium has the advantageous property of having four reasonably accessible redox states: +2, +3, +4, and +5. This allows vanadium to be dissolved in sulfuric acid and serve as an electroactive material on both the posolyte and the negolyte side of a battery. This decreases the challenge of electrolytes passing through the membrane to the wrong side of the battery. The half-reactions involved are shown in Equation 1.1 below:

$$V^{2+} \longrightarrow e^- + V^{3+}$$

$$VO_2^+ + 2H^+ + e^- \longrightarrow VO^{2+} + H_2O$$

Equation 1.1

While vanadium is a promising electrolyte and has engendered several large-scale installations[17, 18], it does face a few challenges. Batteries compete with, steel, high-strength

aerospace materials, and chemical catalysts for vanadium resources. Additionally, vanadium flow batteries are limited to operating temperatures of less than 40°C, above which VO_2^+ is prone to precipitating out as V_2O_5 and removing itself from the redox reaction.[19] Vanadium also is an expensive and highly variable cost component of the batteries (Figure 1.6).

a. b.

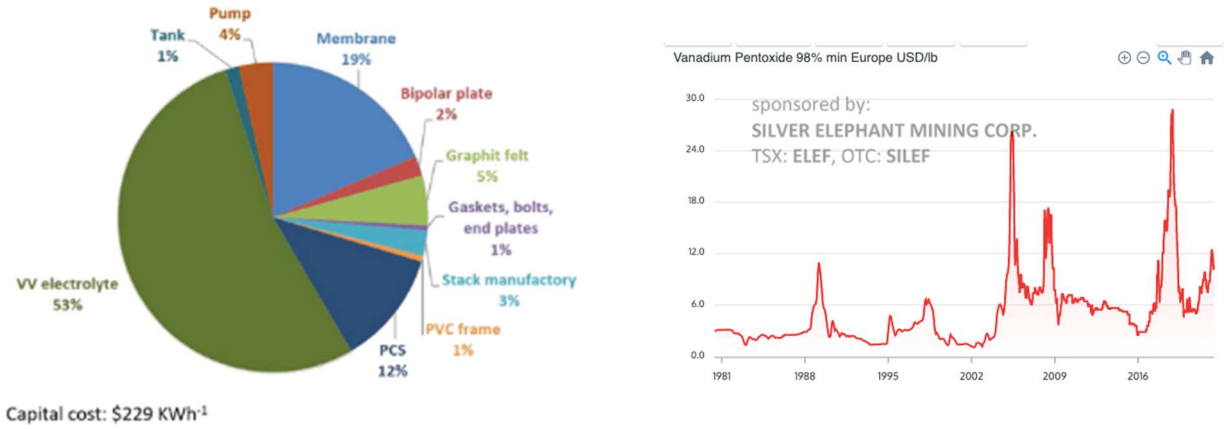

Figure 1.6: Cost of vanadium for flow battery applications. a. Total cost of a flow battery broken down by component in a model of a 1 MW battery.[20] b. The cost of vanadium pentoxide, a common precursor for the vanadium used in flow batteries since 1981.[21]

Figure 1.6 shows a 2015 estimate of the cost of each component of a 1 MW 8-hour vanadium redox flow battery, for which the vanadium electrolyte constitutes an estimated 53% of the total cost. In addition to making up a significant chunk of the total price of the battery, vanadium prices move quickly from as low as $2/lb. to as high as $28/lb of vanadium pentoxide. This volatility is in part due to its limited applications with over 90% of worldwide vanadium production being used in steel production and a limited number of producers, with most vanadium coming from China, Russia, and South Africa.[22] Less expensive electroactive

alternatives are attractive to help bring redox flow batteries below the Department of Energy's goal to decrease long-duration energy storage costs by 90% over the decade starting in 2020.[23]

Organic molecules are an attractive alternative to vanadium. They are composed principally of carbon, hydrogen, and oxygen with nitrogen, phosphorus, and sulfur occasionally also being used. These elements are generally abundantly and cheaply available in the form of commercially available feedstock chemicals. Organic synthesis can be used to modify molecules for desirable reduction potentials, high solubility, and good stability under cell cycling conditions. At this point, a wide variety of redox-active organics have been synthesized and demonstrated in redox flow batteries. Particularly promising molecules include quinones and quinone derivatives[24-46], phenazines[47-50] and other azo-aromatic compounds[51], and viologens[52-55] for low-potential negolytes. These are often paired with benzoquinones, TEMPO derivatives[50, 56-60], and iron inorganic or organometallic[61-64] complexes as posolytes.

1.3 Prior work on anthraquinone electrolytes for redox flow batteries

Benzoquinones, as well as their derivatives, have attracted particular interest as redox-active materials for flow batteries. Various quinone compounds have been used for their accessible redox chemistry by both humans and nature for applications as varied as hydrogen peroxide production, electron transport in cellular respiration, and photosynthesis.[65, 66]

Quinones, as well as the related naphthoquinones (with one aromatic ring attached to the quinone core) and anthraquinones (with aromatic rings attached to both sides of the quinone core), undergo redox chemistry through a two-electron process. Under acidic conditions, where the pH in the solution is lower than the pK_a of the phenolic oxygens in the reduced quinone, this electron transfer is paired with the transfer of two protons (Figure 1.7)

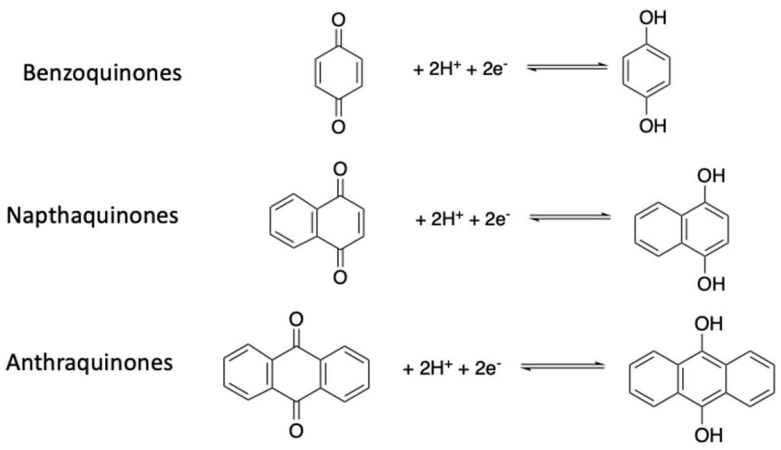

Figure 1.7: Quinone and quinone derivative electrochemistry. In acidic conditions, the quinone ring undergoes an electrochemical two-electron reduction to create the structures shown on the right.

Anthraquinones have proved particularly useful as negolytes for redox flow batteries. This is in part due to their already abundant use in the dye industry which provides several different scaffolds with interesting properties to be used in batteries themselves or to be synthetically modified using methods that have been developed for the synthesis of dyes.[67, 68] Additionally, the electron-donating effect of the two aromatic rings abutting the quinone central ring in anthraquinones tends to drive the reduction potential down toward the lower end of the water splitting window, allowing a high battery voltage when paired with a suitable posolyte. To improve water solubility, anthraquinones are often designed with solubilizing groups attached (see Table 1). Often carboxylate, phosphonate, sulfonate, or ammonium groups will be used so that the charge on the functional group at the appropriate pH will increase the water solubility. To improve stability, molecules often have aliphatic chains linking the solubilizing group to the

main aromatic system.[29] Table 1 shows a list of quinone flow battery molecule candidates reported in the literature.

Table 1.1: Quinone, Naphthoquinone, and Anthraquinone Chemistries Reported For Flow Battery Use

Molecule name	Molecule Structure	Reduction Potential	Maximum reported solubility	Best reported capacity fade (%/day)
2,6-DHAQ[25, 69, 70]	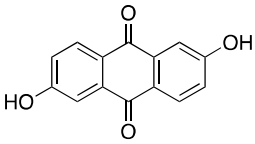	-680 (pH 14)	>0.6 (pH 14)	8 (without electrochemical regeneration) .29 (with electrochemical regeneration)
2,6-DBEAQ[29]	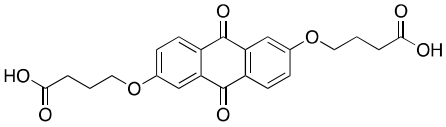	-515 (pH 14)	0.6 M (pH 12) 1.1 M (pH 14)	0.04
2,6-DPPEAQ[33]	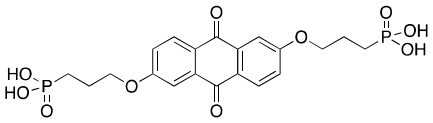	0.47 V (pH 9 unbuffered) −0.49 V (pH 12 unbuffered) -390 (pH 9 buffered) -470 (pH 12 buffered)	0.75 (pH 9)	0.014
1,8-PEGAQ[30]	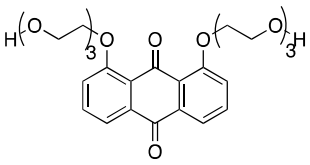	−430 (pH 7) −520 (pH 14)	miscible	0.5

2-AQS[26]	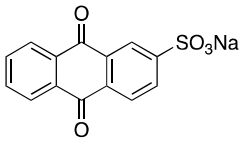	0.187 (pH NL)	> 1 M in acid form	19
AQDS[32 26, 71-74] (multiple cations reported)	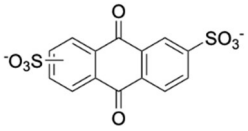	-186 (pH 7)	1.9	0
Lawsone[37]	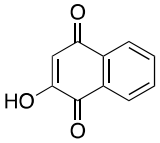	-424 (pH NL)	NL	0.06
2,3-DHAQ[45]	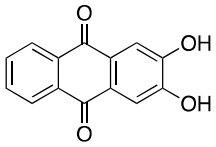	-629	0.7 (pH 13.5)	0.45
2,3-HCNQ[36]	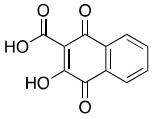	-509 (pH 14)	1.2 M (pH 14)	3.4
Bislawsone[75]	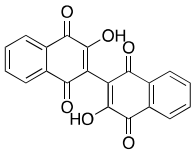	-551 (pH 14)	0.56 (pH 14)	0.74/0.55 (.5/.1 M cell)
DHBQ[27]	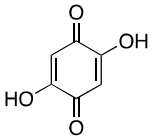	-720 (pH 14)	1.4	9
1,8- BDFAQ[46]	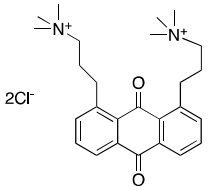	-534 (pH 7)	1.07 (neutral water) 0.52 (2 M KCl)	0.88
DMOBQ[76]	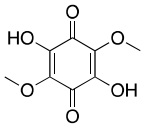	-700 (pH 14)	NL	35
DMBQ[76]	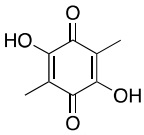	-730 (pH 14)	NL	22
AQDP[29]	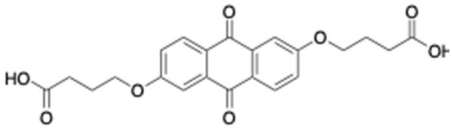	-456 (pH 14)	1 (pH 12)	0.128
ARS[77]	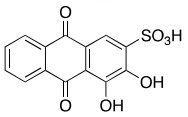	0.082 (1 M H_2SO_4)	3.12 (pH 6-10)	16

2,6-N-TSAQ[44]	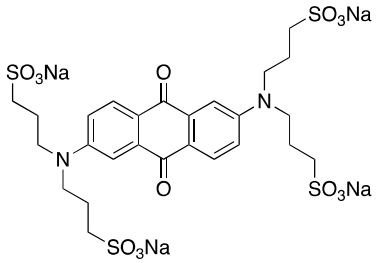	-620 (pH 12+)	0.45 (pH 14)	.025
AMA[78]	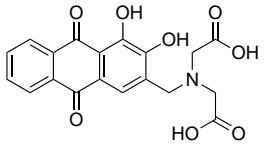	-670 mV (pH 14)	0.46 (pH 14)	.81

Chapter 2 Increasing the solubility and stability of electroactive compounds

Abstract

Previous reports have found that anthraquinone negolytes can be stabilized by connecting solubilizing groups to the anthraquinone core through an ether linkage and an aromatic chain. However, this strategy opened up the possibility of decomposition by side chain loss. In this chapter, I describe a strategy for preventing this decomposition mechanism and dramatically improving the solubility of anthraquinones by using chiral branched aliphatic chains to connect a carboxylate solubilizing group through an ether linkage. The resulting molecule displayed extremely slow capacity fade and high energy density.

2.2 Background and motivation

In 2016, 2,6-DBEAQ (2,6-**d**i**b**utyrate **e**ther **a**nthra**q**uinone) was published and demonstrated the ability to significantly stabilize anthraquinones by attaching solubilizing groups through ether-linked side chains.[29] This molecule, however, was found to experience capacity fade at a rate of about 0.04%/day in cell cycling tests. Analysis of molecular decomposition showed that one decomposition route was the loss of the ether-linked side chains through either an S_n2 or S_NAr reaction (Figure 2.1). The resulting decomposition product is still likely electroactive; however, the increased electron density in the aromatic ring system from the electron-donating phenoxide is likely to create a lower potential molecule. Previous work has

shown that anthraquinones with more negative potentials tend to decompose more rapidly.[70] The monoalkylated molecule is therefore likely to decompose more quickly than the parent molecule.

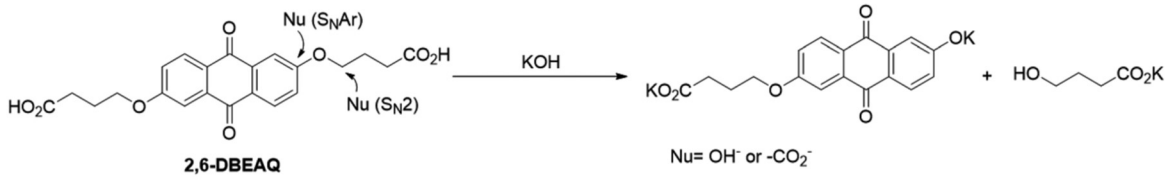

Figure 2.1: Possible decomposition routes of 2,6-DBEAQ. The proposed decomposition by side-chain loss of DBEAQ. Decomposition may occur by either S_n2 or S_nAr routes and the nucleophile may be either hydroxide ion (at high pH) or carboxylate from the solubilizing group (at more moderate pH). Image credit: Ji, 2014[33]

A variety of techniques have since been reported to prevent side chain loss. These techniques include replacing the carboxylate solubilizing group with a phosphate solubilizing group, allowing both acceptable solubility at lower pH (where the concentration of hydroxide is lower) and removing a weak nucleophile (carboxylate) from any intermolecular reactions.[33] Another approach involved replacing the ether-linkage with nonhydrolyzable carbon linkages.[43] However, no approach had focused on limiting side chain hydrolysis through modification of the straight-carbon chain linking the ether to the carboxylate group.

2.3 Synthesis and solubility studies of 2,6-di-2-propionateanthraquinone

To slow side-chain loss as a decomposition mechanism, an anthraquinone was designed using a one-carbon long side chain with a methyl branch. The rationale for this design was to increase the steric hindrance at the aliphatic carbon adjacent to the ether group to slow any

substitution reaction at that carbon. The shorter side chain was also designed to pose a barrier to intramolecular attack by the carboxylate group by removing flexibility from the side chain and forcing strained configurations to reach the susceptible carbons. While not the primary goal in the molecular design, this synthesis is also able to utilize a starting material (methyl 2-bromopropionate) that is cheaper than the original 2,6-DBEAQ molecule (which used methyl 4-bromobutyrate).

This molecule, named 2,6-D2PEAQ (2,6-**d**i-**2**-**p**ropionate **e**ther **a**nthra**q**uinone) was synthesized using alkylation with a secondary alkyl bromide which resulted in an ester that easily precipitated out of solution and was filtered and hydrolyzed into the final product without further purification (Figure 2.2). The resulting carboxylic acid was then precipitated with hydrochloric acid, dried, and used for cell testing. A complete account of the synthetic procedure is in Appendix 1.

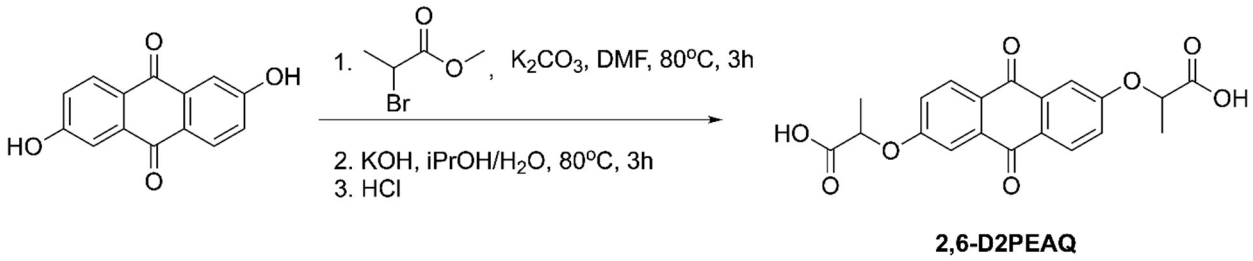

Figure 2.2: Synthetic procedure for the synthesis of 2,6-D2PEAQ

2,6-D2PEAQ was subjected to solubility tests using sodium, potassium, and ammonium counterions. While it showed a solubility of <0.1 M when ammonium was used as the cation, the solubility in both sodium and potassium counterion was extremely high; between 1.5 and 2.1 M when measured at both pH 7 and pH 12. While the solubility was not measured quantitatively at

other pH ranges, no precipitation was seen at a concentration of 1.5 M at any pH between 7 and 12 with either potassium or sodium counterion, leading to the conclusion that this is the lower bound on solubility. Notably, this is a considerable improvement over the solubility of 2,6-DBEAQ, which had a solubility of <0.1 M in pH ranges lower than 12 or when sodium instead of potassium counterion was used. In conditions where it was soluble, it showed only 0.6 M solubility at pH 12 with potassium counterion and 1.1 M at pH 14.[29] The high solubility at lower pH is an attractive feature of 2,6-D2PEAQ because ferrocyanide, a common and inexpensive posolyte in alkaline organic flow batteries, is more soluble when the pH is closer to 7, allowing a greater energy density in the battery overall.

To understand better the dramatic solubility improvements of 2,6-D2PEAQ an analog without the methyl branch was synthesized (appendix A) by a similar method. This molecule, 2,6-DEEAQ (2,6-**di**e**e**thanoic **e**ther **a**nthra**q**uinone) showed a much lower solubility (Figure 2.3), leading to the conclusion that adding the branching functionality to 2,6-D2PEAQ aided in improved solubility. While the reason for this is unknown, it may be related to the 3D structure created at the branched carbon making crystallization more unfavorable and improving solubility. Alternatively, the methyl group creates chiral centers on each of the two branches. Because racemic starting material was used to synthesize 2,6-D2PEAQ the resulting product is a mixture of two enantiomers and a diastereomer. It has been reported that chirality can impact the

favorability of crystallization, and this may contribute to the high solubility of 2,6-D2PEAQ.[79, 80]

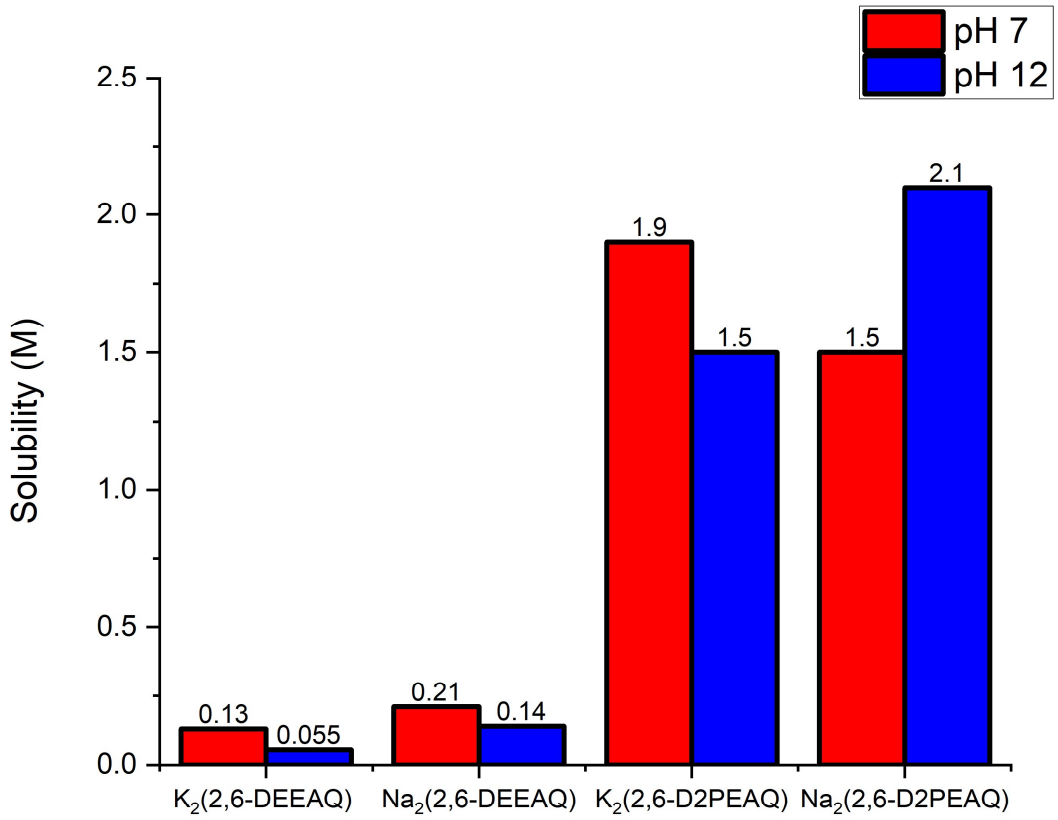

Figure 2.3: Solubility of 2,6-D2PEAQ and 2,6-DEEAQ. The solubility of both 2,6-D2PEAQ and 2,6-DEEAQ was measured in both sodium and potassium counterions at both pH 7 and 12 in their oxidized form. The reduced form was not tested due to experimental challenges posed by its oxidation by ambient oxygen, but it is expected to be similar or more soluble due to the two additional negative charges on each molecule. UV-Vis calibration curves and spectra for saturated solutions were collected by Thomas George.

2.4 Thermal and photostability studies of 2,6-D2PEAQ

To analyze the efficacy of the branched side chain at preventing side chain loss, 2,6-D2PEAQ was subjected to thermal decomposition analysis. This analysis is done before cell testing of potential flow battery compounds to facilitate an understanding of molecular stability with a minimal amount of synthesized electrolyte and to separate decomposition routes that are caused by thermal decomposition from those that are caused by changes in the molecule on electrochemical charging and discharging.

To test decomposition, 0.1 M solutions of 2,6-D2PEAQ were heated in a laboratory oven for 1 week at 95 ºC at a variety of pH values. This high temperature was chosen to maximize the decomposition of 2,6-D2PEAQ without boiling the water it was dissolved in. Figure 10 shows the results of the oxidized form decomposition studies at pH 7, 12, and 14. While some NMRs show a small peak at 1.78 ppm, this peak is generally small. No new aromatic peaks were seen that would indicate a monoalkylated product had formed.

a.

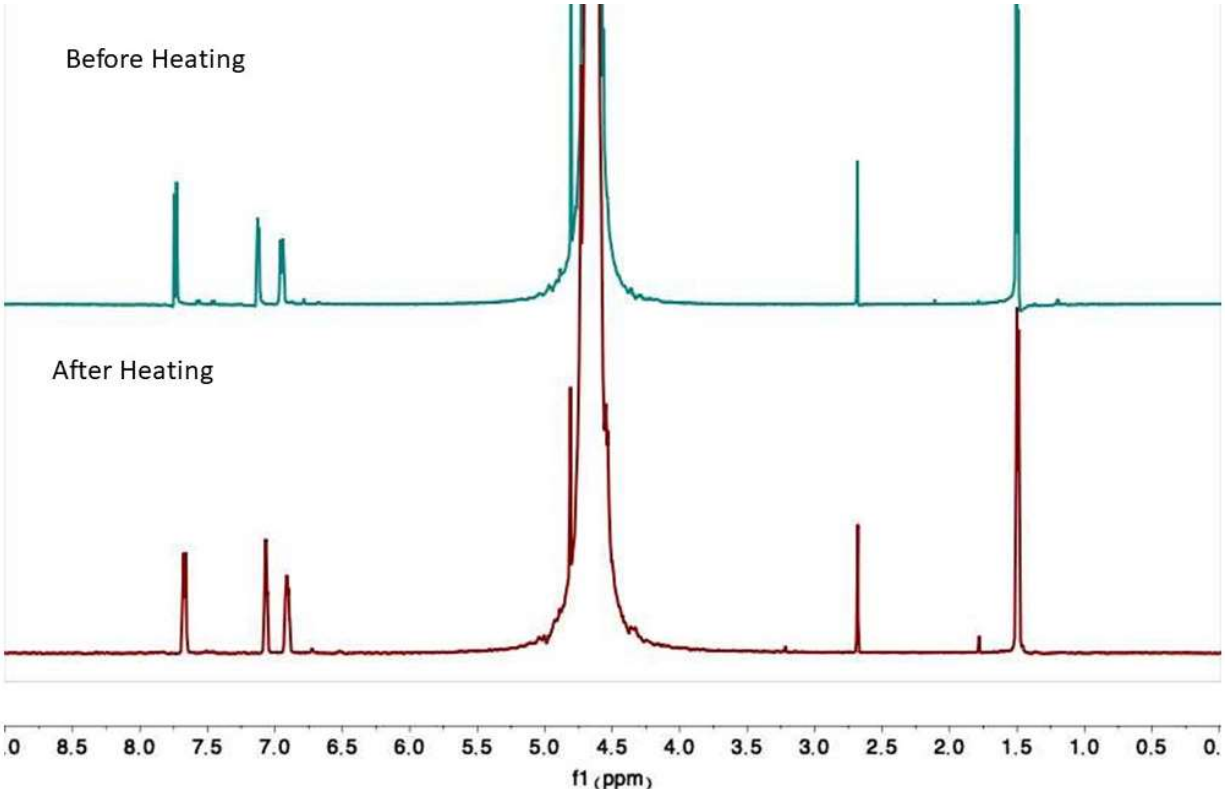
Before Heating
After Heating
8.5 8.0 7.5 7.0 6.5 6.0 5.5 5.0 4.5 4.0 3.5 3.0 2.5 2.0 1.5 1.0 0.5
f1 (ppm)

b.

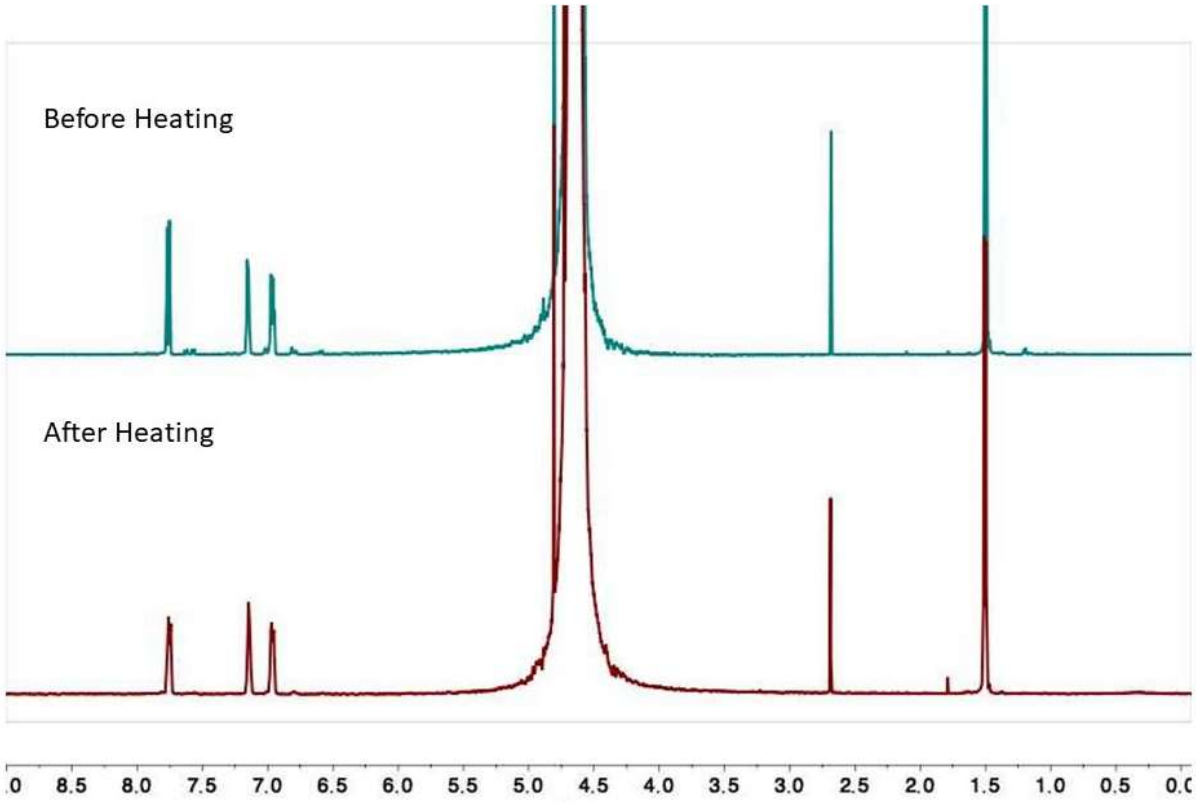
Before Heating
After Heating
8.5 8.0 7.5 7.0 6.5 6.0 5.5 5.0 4.5 4.0 3.5 3.0 2.5 2.0 1.5 1.0 0.5

c.

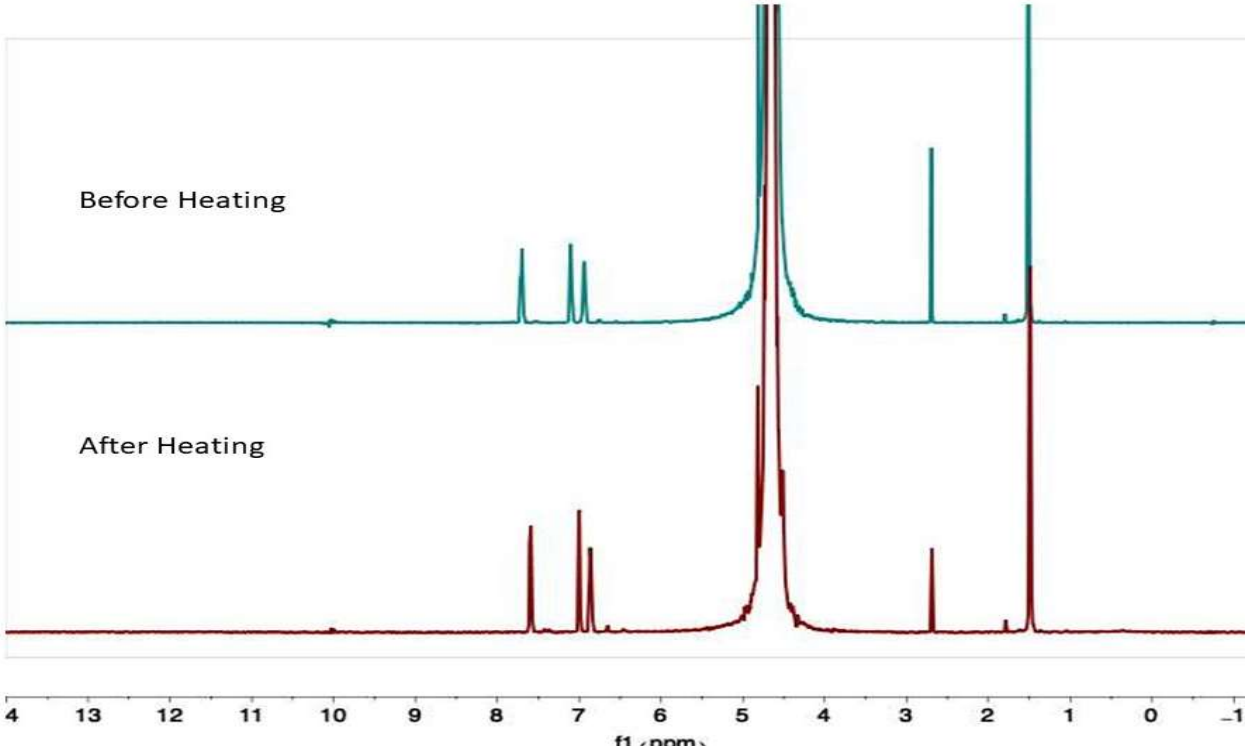

Figure 2.4 Thermal decomposition study of D2PEAQ. NMR spectra before and after 0.1 M 2,6-D2PEAQ stored in a. pH 7, b. pH 12, and c. pH 14 solutions at 95 ºC for one week.100 µL of the cooked solution was then diluted with 500 µL of D_2O. NMR spectra were obtained on a 500 MHz Varian Unity Inova500 NMR.

Anthraquinones have been known to decompose by different routes in both the oxidized and the reduced forms, often by different mechanisms.[81] In order to probe decomposition pathways that may be affecting the reduced form of 2,6-D2PEAQ a 0.1 M solution was charged in a glovebox and stored at pH 12 for 1 week at 95 ºC. To prevent oxygen penetration, which would revert the reduced form to oxidized anthraquinone, the FEP vial containing the solution was enclosed in a mason jar that was inverted and placed in a small pool of water in a larger mason jar. After the heating period was completed, the material was re-oxidized by agitating the

solution with ambient air for 30 minutes. This was done to ensure good shimming for a clear NMR spectrum because reduced anthraquinones often show peak broadening due to semiquinone radical formation even when efforts are made to protect them from oxygen exposure. No new peaks were found on the NMR after heating, leading to the conclusion that 2,6-D2PEAQ does not experience rapid thermal decomposition in the reduced form (Figure 2.5).

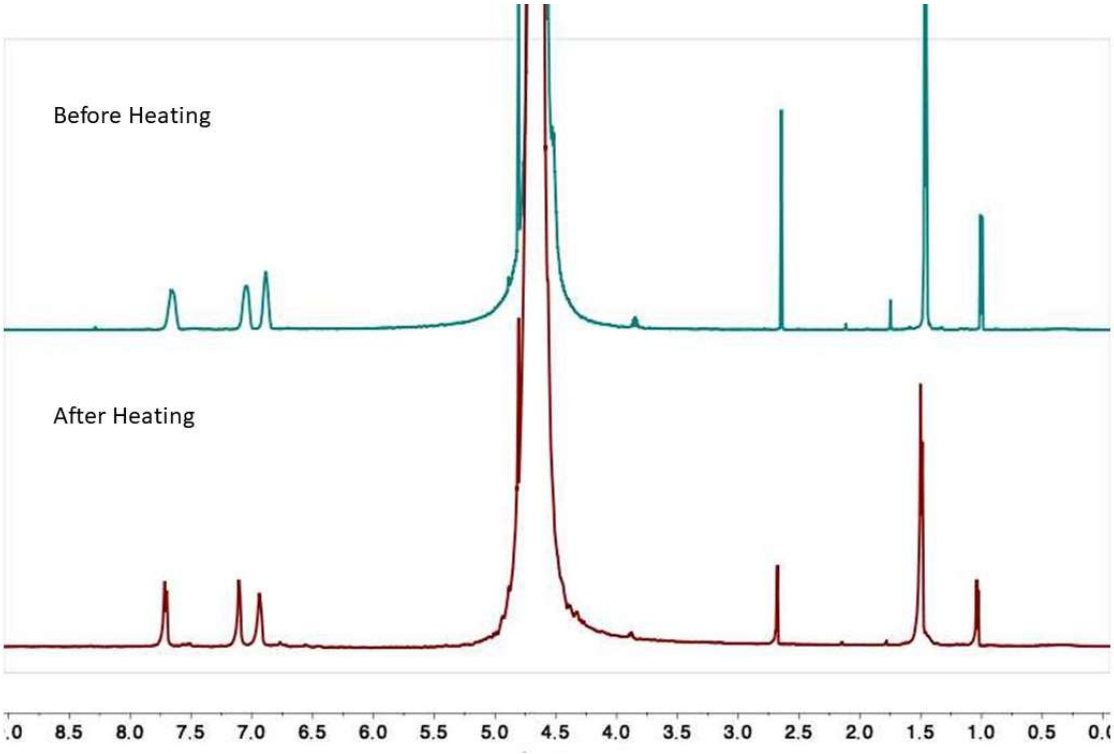

Figure 2.5: Thermal decomposition of 2,6-D2PEAQ in the reduced form. ^{1}H NMR of 2,6-D2PEAQ in the oxidized form before and after being heated at 95 ºC for a week in the reduced form.

While minimal decomposition was seen when 2,6-D2PEAQ was exposed to heat, the molecule was also tested when exposed to light. To accelerate any photochemical decomposition

reactions, 0.1 M solutions of 2,6-D2PEAQ were sealed in vials and floated in a large tub of water to maintain a near-constant temperature. The vials and the water bath were exposed to a 500 W lightbulb for one week. As a control, identical vials of 2,6-D2PEAQ were prepared and wrapped in aluminum foil. This experiment showed significant decomposition under light, leading to the recommendation that this material be tested in low-light conditions or protected from light. (Figure 2.6)

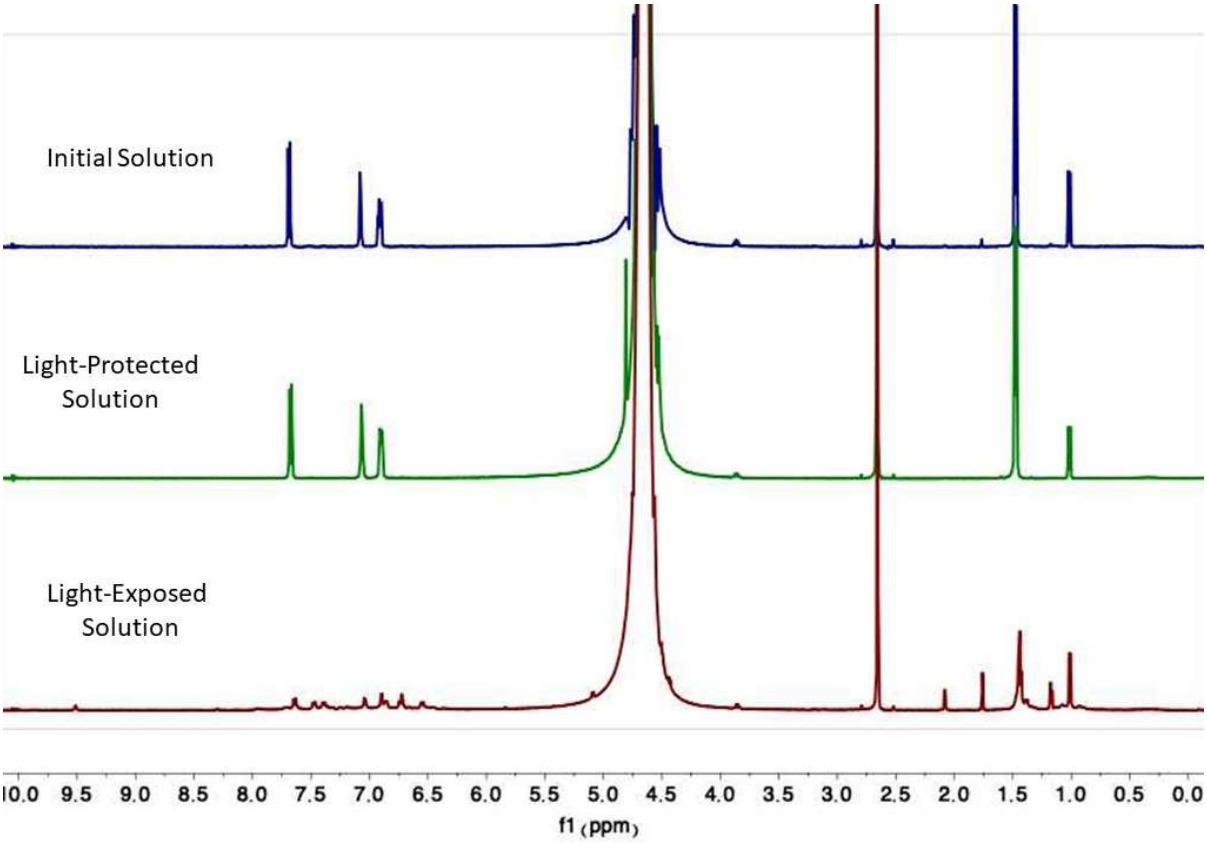

Figure 2.6: Photochemical decomposition of 2,6-D2PEAQ. 0.1 M solutions were exposed to a 100W light for 1 week either protected by an aluminum foil wrapping (green) or exposed to the light (red).

2.5 Electrochemical characterization

To assess the feasibility of 2,6-D2PEAQ as a flow battery electrolyte candidate, a cyclic voltammogram was obtained to determine the voltage and provide some preliminary information on the electrochemical kinetics of the molecule. At pH 14 the reduction potential of 2,6-D2PEAQ was determined to be -445 mV v. SHE (Figure 2.7). When paired against potassium ferrocyanide, a common posolyte for alkaline organic flow batteries, a total cell voltage of 951 mV is achievable.

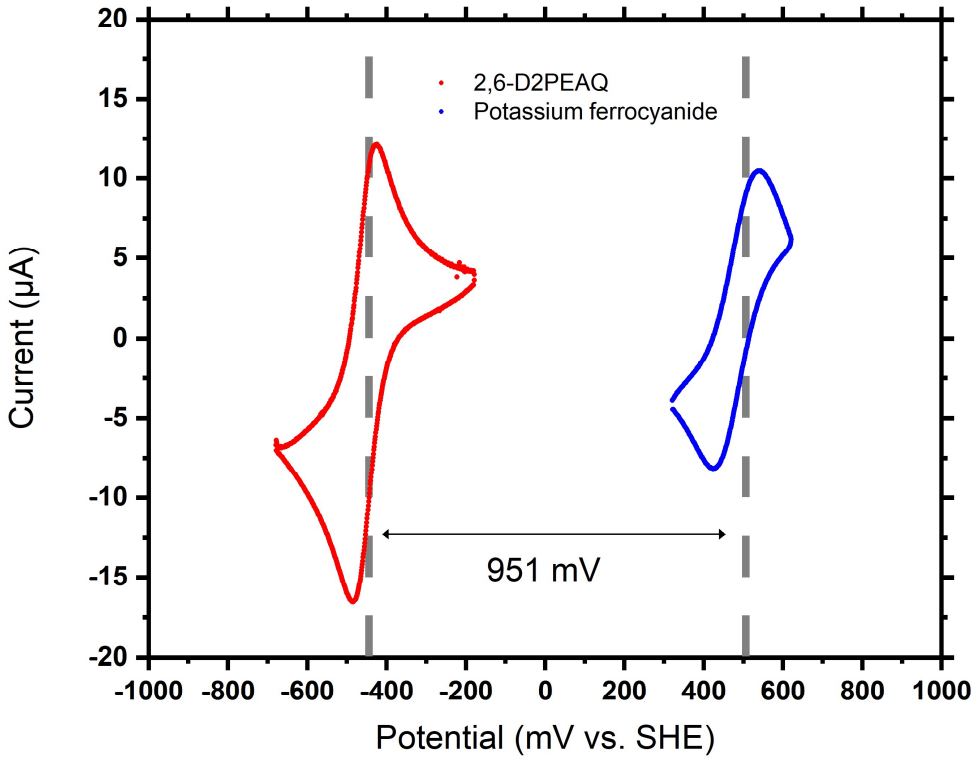

Figure 2.7: Cyclic Voltammetry of 2,6-D2PEAQ (red) paired with potassium ferrocyanide (blue) at pH 14.

Because 2,6-D2PEAQ is soluble at moderate pH ranges, the initial reduction reactions at moderate pH ranges are proton-coupled. As the reduction process increases the hydroxide ion concentration in the solution, the pH in the solution swings up until it reaches a pH where the reduction becomes a 2-electron 0-proton process. To probe how the redox reaction affected the pH of the solution, a Pourbaix diagram was prepared to determine the effect of pH on the reduction potential. Because the potential is dependent on the reaction quotient according to the Nernst equation and because anthraquinone reduction uses up protons at low to moderate pH ranges, the reduction potential is expected to be dependent on pH. In a theoretical system, the slope of the reduction potential v pH curve is -59 mV/pH unit when the two-electron reaction is coupled with two protons and -29 mV/pH where the reaction is coupled with one proton. The Pourbaix diagram showed that 2,6-D2PEAQ undergoes 2-electron 1-proton reduction from about pH 7.5 to pH 11, above which range it is proton decoupled and below which two protons participate in the reduction (Figure 2.8a).

The pH-swing behavior was studied in a cell setup containing 0.1 M 2,6-D2PEAQ and a ferrocyanide posolyte was prepared by Dr. Shijian Jin. This cell used a pH meter to measure the pH of the negolyte reservoir as the cell was charged and discharged. The pH in the discharged form quickly increased from 7 to 9, reflecting the very small increase in hydroxide ion concentration required to increase the pH by one unit at moderate pH values. After that initial shift, the pH cycled reversibly between pH 9 and 12. Because ferrocyanide solubility is higher at lower pH, it is beneficial that the pH does not increase over the course of cell cycling (Figure 2.8b).[82, 83]

a. b.

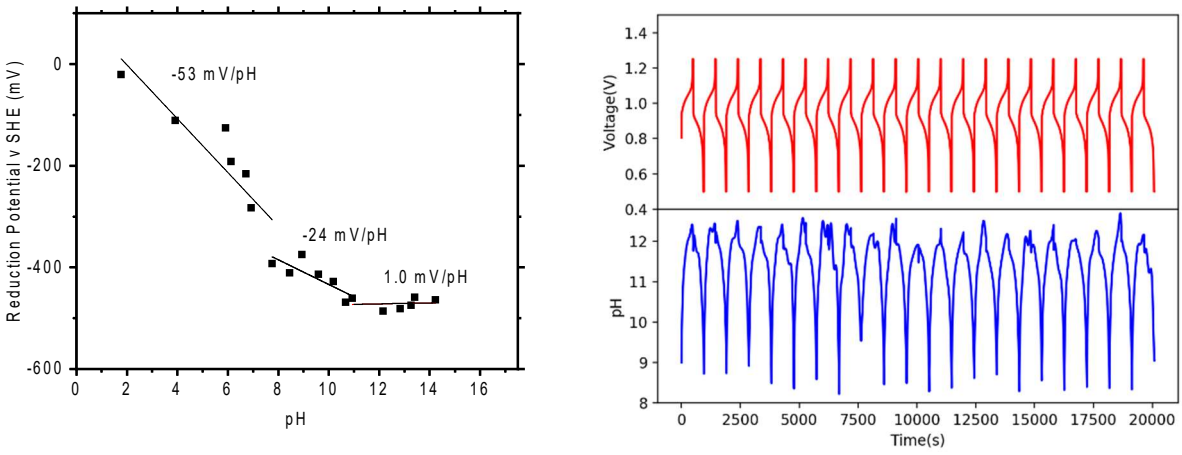

Figure 2.8: Pourbiax diagram and pH-swing cell of 2,6-D2PEAQ. a. Pourbaix diagram of 2,6-D2PEAQ. All reduction potentials between pH 2 and pH 12 are measured in an appropriate buffered solution to prevent local pH swings near the electrode. Reduction potentials are measured using cyclic voltammetry in 1 mM 2,6-D2PEAQ b. pH swing cell of 2,6-D2PEAQ. pH-swing cell run and graph prepared by Dr. Shijian Jin.

Rotating disk electrode measurements performed by Dr. Kiana Amini were used to determine the diffusion coefficient and rate constant of 2,6-D2PEAQ. To determine the diffusion coefficient, the limiting current at different rotation rates was obtained from linear sweep voltammograms and plotted against the square root of the rotation according to the Randles-Sevich equation (Equation 2)[84] The slope was used to extract the diffusion coefficient, 2.75 * 10^{-6} cm^2/s.

$$i_p = 2.69 * 10^5 * n^{\frac{3}{2}} * A * D^{\frac{1}{2}} * C_i * v^{\frac{1}{2}}$$

Equation 2.1: The Randles-Sevcik equation. i_p is the limiting current (A), n is the number of electrons transferred, A is the electrode area (cm^2), D is the diffusion coefficient (cm^2/s), C is the concentration (mol/mL), and v is the scan rate (Figure 2.9a and 2.9b).

The rate constant was constructed by plotting the rotating disk electrode on a Koutecký-Levich plot and performing a Tafel analysis (Equation 2.2)[84]. The kinetic rate constant was found to be 3.40×10^{-3} cm s^{-1} (Figures 2.9c and 2.9d)

$$i = nk^0FCe^{(\frac{\alpha F\eta}{RT})}$$

Equation 2.2: The Tafel equation where i is current, n the number of electrons, k^0 the rate constant (s^{-1}), F is the Faraday constant, C is the concentration (M), R is the gas constant, and T is the temperature.

a.

b.

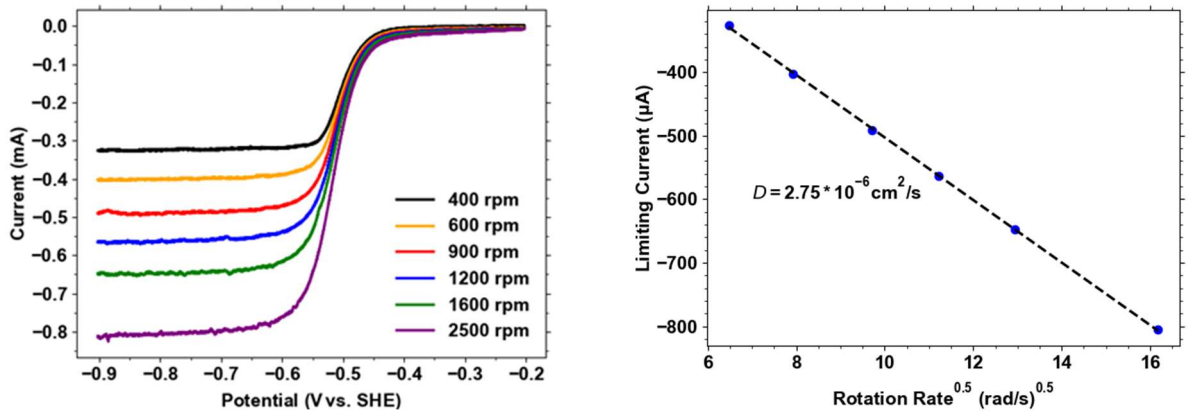

c.

d.

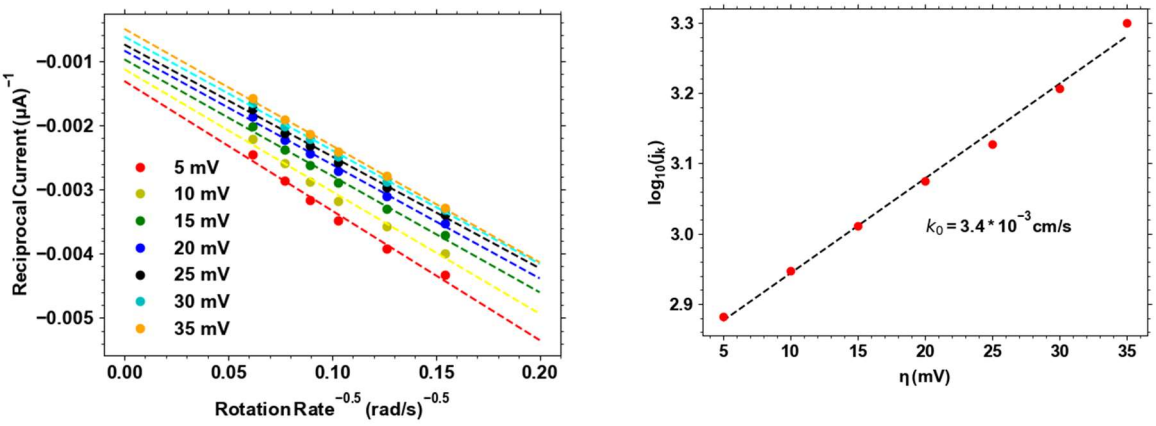

Figure 2.9: Rotating Disk Voltammetry of 2,6-D2PEAQ. a. Current at different rotation rates v Potential. b. Linear graph of limiting current vs. the square root of rotation rate used to calculate the diffusion coefficient. c. Plot of square root against the reciprocal current. d. Tafel analysis was used to produce the kinetic rate constant of the 2,6-D2PEAQ reduction reaction. Graphs and data were produced by Dr. Kiana Amini.

2.6 Cell cycling studies of 2,6-D2PEAQ

2,6-D2PEAQ was initially tested at pH 7 at a 0.1 M concentration. The posolyte comprised 0.2 M of potassium ferrocyanide. 7 mL of 2,6-D2PEAQ was used against 30 mL of posolyte. The excess of posolyte ensured that any changes in the cell capacity during cycling were caused by changes to the negolyte by having several equivalents of potassium ferrocyanide. An E-620K membrane was used. To minimize potassium ferrocyanide crossover through the membrane, 0.15 M potassium ferrocyanide was added to the negolyte.

The cell was cycled at a constant current until it reached a pre-set potential on both charge and discharge. This was followed by a constant potential hold to avoid changes in internal resistance affecting the capacity accessed by the cell. When the potential holds were initially set at 0.6 V on discharge and 1.5 V on charge, the capacity faded at about 0.11%/day. However, when the voltage cutoffs were changed to 0.5 and 1.4 V on discharge and charge respectively the capacity fade decreased to 0.03%/day. A further decrease to 0.02%/day was seen when the upper voltage limit was lowered to 1.25 V. The coulombic efficiency of this cell was consistently high at 99.97% or higher (Figure 2.10).

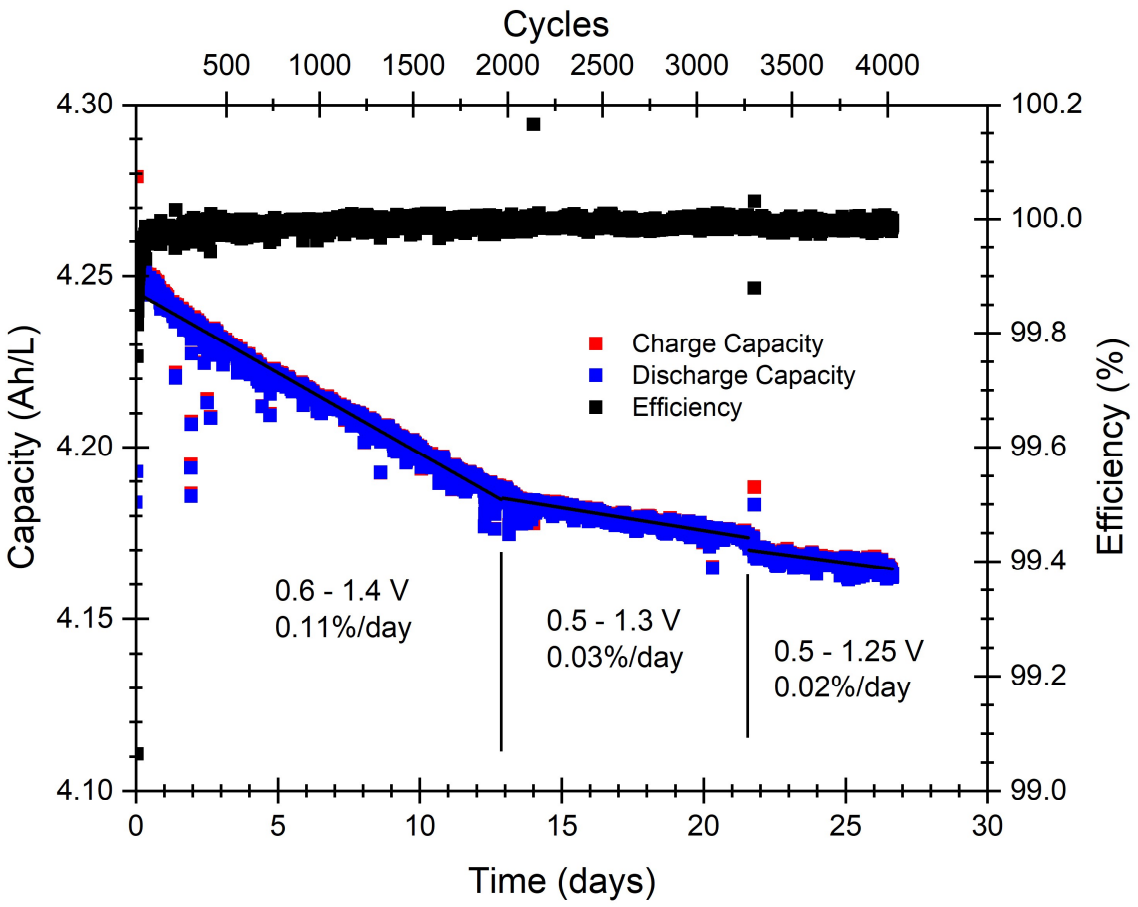

Figure 2.10: 0.1 M cell of 2,6-D2PEAQ. 2,6-D2PEAQ cycled at 0.1 M. Black vertical lines indicate changes in current cutoffs. The cell was assembled and managed by Dr. Zhijiang Tang, with prepared electrolyte solutions.

Because 2,6-D2PEAQ showed good performance at 0.1 M, higher concentration cells were prepared. An initial 0.5 M cell showed erratic capacity access. While the exact cause of this is unknown, the capacity fluctuations were found to correlate well with the changing temperature in the lab. To alleviate this, the 0.5 M cell was run at 40 °C with an Omega CS8DBPT PID controller to allow control of the temperature. This cell continued to show extremely slow capacity fade, measuring 0.01%/day over a 13.5 day period and indicating that the capacity fade

of 2,6-D2PEAQ did not measurably increase when the temperature was increased from room temperature (Figure 2.11). This suggests that, at a larger scale, active cooling would not be necessary to maintain the stability of 2,6-D2PEAQ.

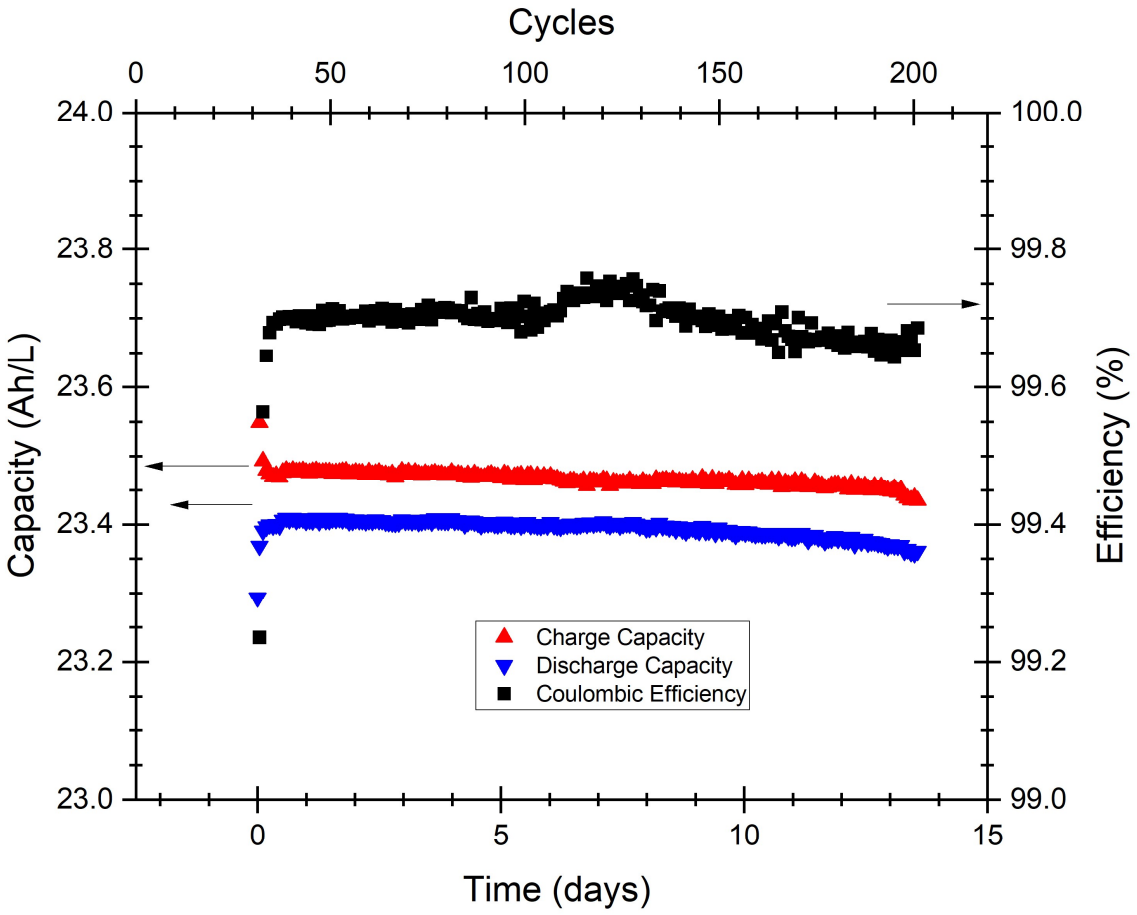

Figure 2.11: 0.5 2,6-D2PEAQ cell. At 0.5 M 2,6-D2PEAQ faded at 0.01%/day over a 13.5 day period at 40 ºC. Cell was prepared and managed by Dr. Zhijiang Tang with prepared electrolyte solutions.

The high solubility of 2,6-D2PEAQ makes it an attractive candidate for high-concentration flow batteries where it can provide a high volumetric capacity and energy density.

1.1 M was chosen for the 2,6-D2PEAQ concentration in a high concentration cell. This concentration was chosen to maximize the number of electrons in the reservoir without encountering the challenges associated with accessing the full capacity by material becoming stuck on reservoir walls or clogging tubing at the high viscosities that occur at higher 2,6-D2PEAQ concentrations.

A cell was prepared using a 1.1 M (5.3 mL) 2,6-D2PEAQ capacity-limiting negolyte and 30 mL of 0.6 M sodium ferrocyanide, 0.4 M potassium ferrocyanide, and 0.2 M sodium ferricyanide posolyte at an initial pH of 7. This cell was cycled for 27 days and demonstrated a capacity fade rate of 0.018%/day from day 6 to the end of cycling on day 27 (Figure 2.12), extrapolating to a loss of capacity of only 6.6%/year. The coulombic efficiency remained high at 99.8%

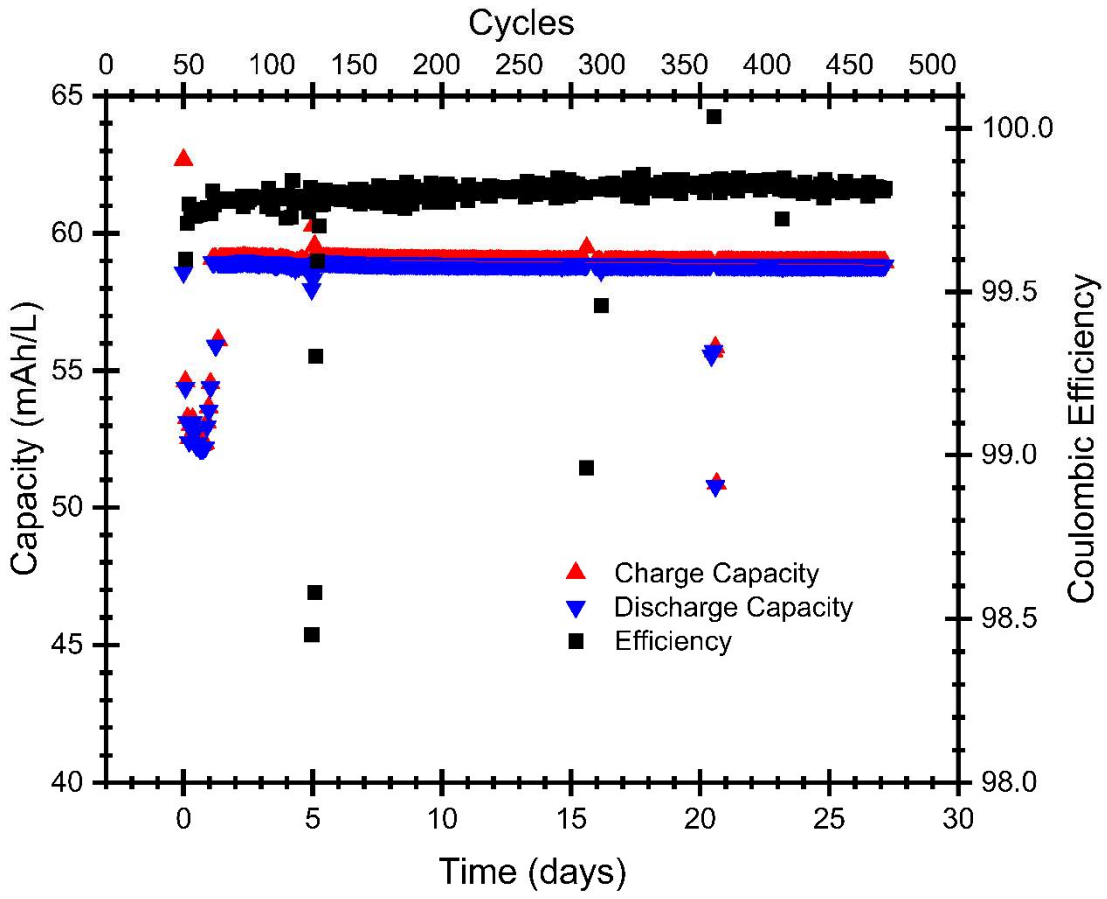

Figure 2.12: 1.1 M cell of 2,6-D2PEAQ. The dip on day 5 is attributed to a disruption in nitrogen flow to the glove bag. The cell was assembled and managed by Dr. Zhijiang Tang, with prepared electrolyte solutions.

The same cell set-up was used to collect polarization curves and determine the power density of the cell (Figure 12.13a). The maximum power density of the cell was found to be 0.16 W/cm^2 at a current density of 300 mW/cm^2 and 100% state of charge. This cell was further used to determine if the open-circuit voltage varied with the state of charge (Figure 12.13b). Charge-discharge voltage profiles were used to compare the accessed capacity to the theoretical capacity (1124 C) and to determine whether any unexpected redox activity might be occurring (Figure 2.13c) the curves show all the capacity is accessed at 150 mW/cm^2 and higher current densities,

with less than full capacity being accessed at lower current densities. A single plateau is observed on all voltage profiles, corresponding to the oxidation and reduction of 2,6-D2PEAQ. No additional plateaus that may indicate other redox reactions occurring are seen. Finally, the coulombic efficiency, round-trip energy efficiency, and round-trip voltage efficiency were measured at increasing current densities (Figure 2.13d). The round-trip efficiencies generally decreased at increasing current densities. At 20 mA/cm^2 round-trip voltage efficiency was 92.9% and round-trip energy efficiency was 92.1%. At 200 mA/cm^2 the round-trip voltage efficiency was 48.8% and the round-trip energy efficiency was 48.7%. Coulombic efficiencies were over 99% for all measurements.

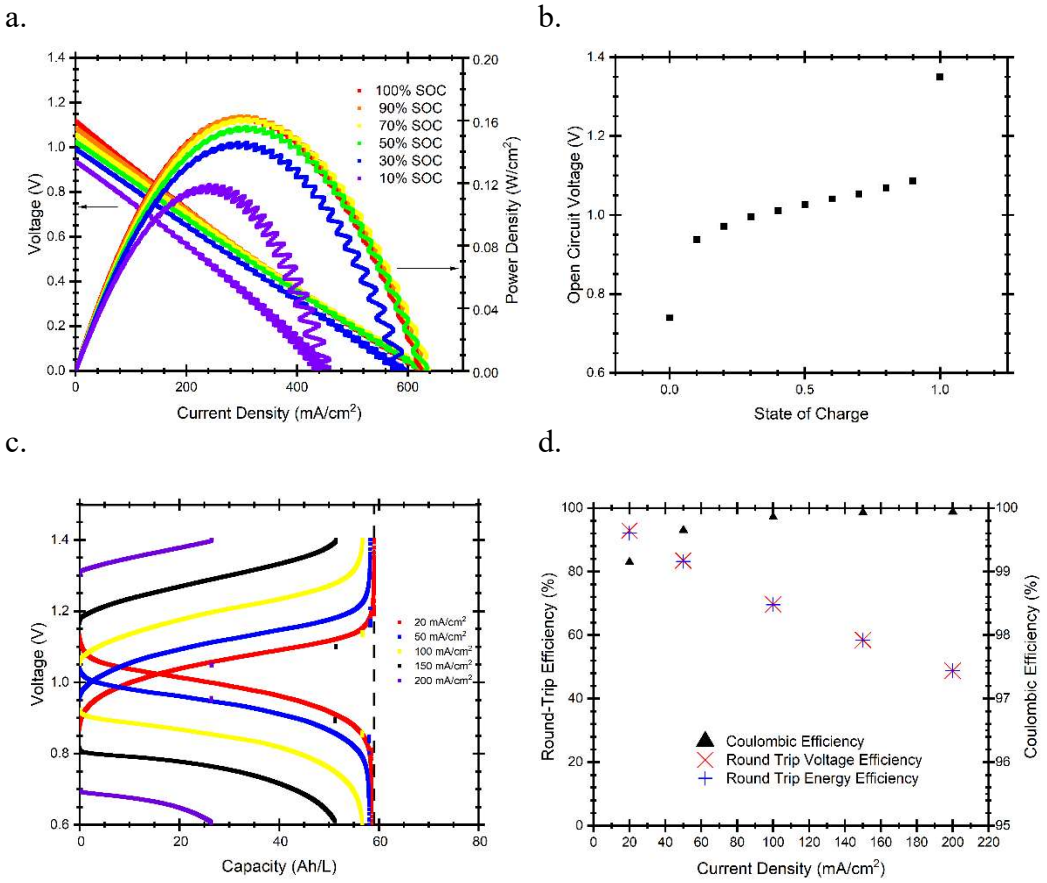

Figure 2.13: Cell performance of 2,6-D2PEAQ. Cell performance studies of 2,6-D2PEAQ at 1.1 M and 40 ºC. a. Polarization curves and power densities. b. Open Circuit voltage with increasing state of charge. c. Charge and discharge voltage profiles. d. Efficiencies at differing states of charge. Cell prepared and managed by Dr. Zhijiang Tang.

The high-energy density of 2,6-D2PEAQ, facilitated by its high solubility, is a major strength of the molecule. To demonstrate this, a "nearly-balanced" cell was prepared by Thomas George using a minimal excess of posolyte to maximize the energy density of the cells (Figure 2.14). For electrolytes, this cell used 4.5 mL of 1.1 M 2,6-D2PEAQ and 14 mL of 1.0 M

ferrocyanide. Because 1.0 M is near the upper solubility limit of potassium ferrocyanide, a mixture of sodium and potassium counterions was used in a ratio of 3:7 sodium: potassium to ensure no precipitation of the posolyte.[82, 83] This cell demonstrated 0.02%/day capacity fade (7.3%/year) over a period of 14 days. It demonstrated an energy density of 13.63 Wh/L and a volumetric capacity of 14.34 Ah/L.

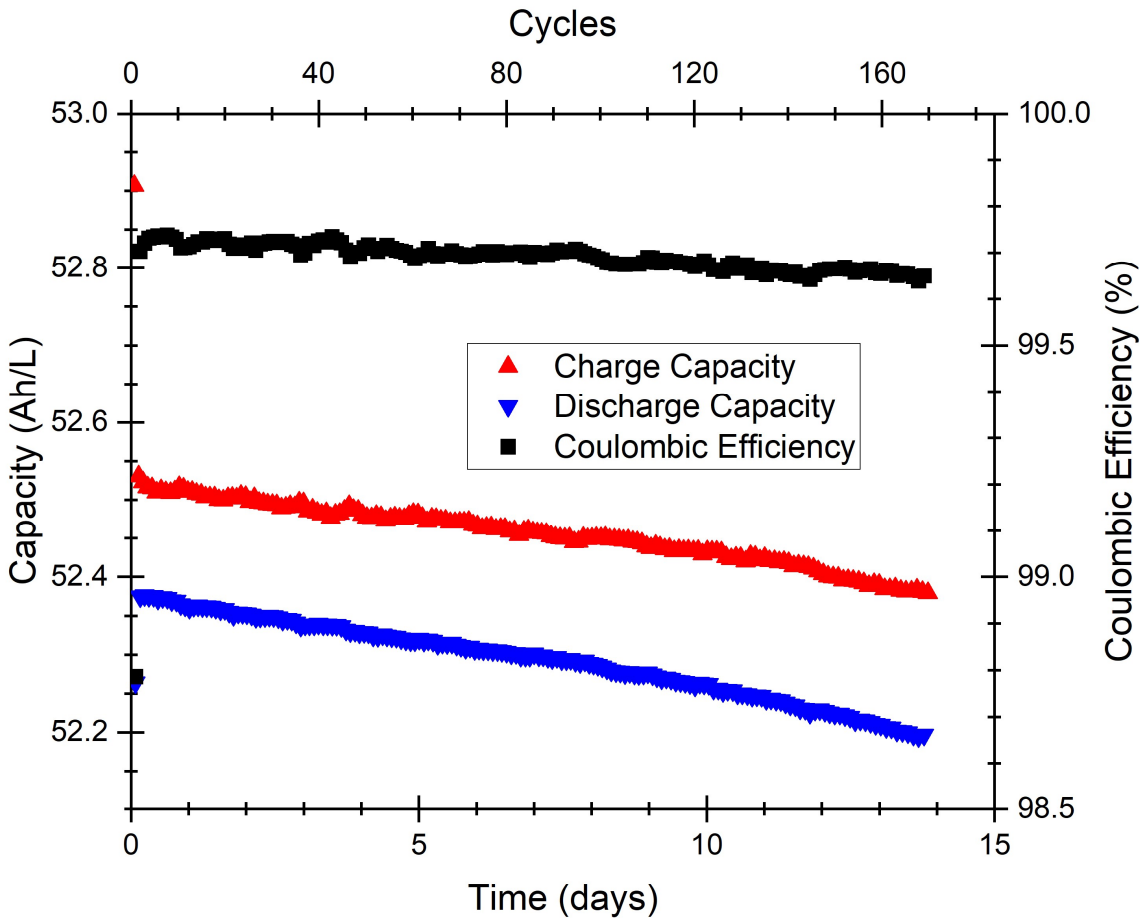

Figure 2.14: Nearly balanced cell of 2,6-D2PEAQ. Cell was run by Thomas George.

To compare the performance of 2,6-D2PEAQ to previously reported organic molecules in aqueous flow batteries, Figure 2.15 compares the demonstrated volumetric capacity of the negolyte and the capacity fade for each negolyte candidate reported in the aqueous organic flow battery literature. 2,6-D2PEAQ showed the slowest capacity fade for any molecule with a

volumetric capacity over 55 Ah/L and the highest volumetric capacity for any molecule fading more slowly than 0.5%/day, with the exception of the fluorenone compound named 4C7FL. However, that fluorenone was cycled without potentiostatic holds, which are used to ensure capacity fade measurements are accurate and not affected by internal changes in cell resistance. When the fluorenone was run with potentiostatic holds, a fade rate higher than 2,6-D2PEAQ was reported.

Figure 2.15: Comparison of energy density and capacity fade of flow battery negolytes. Demonstrated volumetric capacity of the negolyte and capacity fade rate for reported organic redox flow batteries are plotted. Cells that were cycled without capacity holds are depicted with hollow circles. In cases where the original paper did not report capacity fade in time-denominated terms, an estimate was made using the reported current density and electrode size. When the same negolyte was reported by multiple papers, the lowest reported fade rate was used. When multiple cells utilizing the same chemistry were reported in a single paper, the highest concentration cell was included (There were no cases in which the highest reported concentration had a significantly higher fade rate than lower-concentration cells). Cells that ran with less than 0.1 M electrons in the negolyte or for fewer than 10 cycles were excluded. Cells that used electrochemical capacity recovery strategies are marked with an asterisk. Data from[24, 26, 27, 29, 30, 33, 36-38, 43, 45-49, 51, 55, 64, 70, 75-78, 85-99]

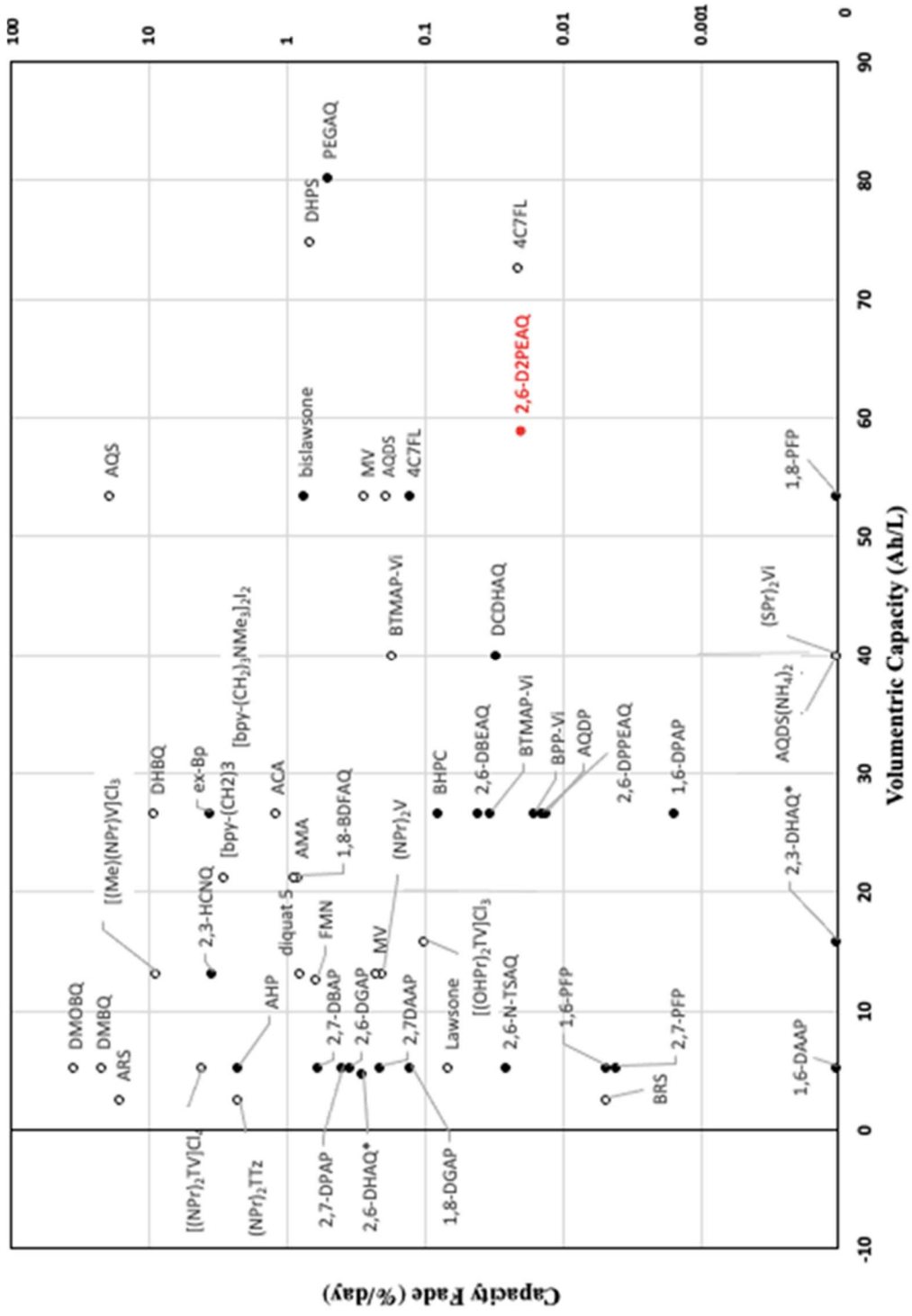
Capacity Fade (%/day)
Volumentric Capacity (Ah/L)
100
10
1
0.1
0.01
0.001
0
-10
0
10
20
30
40
50
60
70
80
90
DMOBQ
DMBQ
ARS
[(Me)(NPr)V]Cl3
AQS
DHBQ
ex-Bp
2,3-HCNQ
[bpy-(CH2)3
[bpy-(CH2)3NMe3]2I2
ACA
AHP
diquat 5
AMA
1,8-BDFAQ
FMN
2,7-DBAP
2,6-DGAP
MV
(NPr)2V
2,7DAAP
BHPC
Lawsone
[(OHPr)2TV]Cl3
2,6-N-TSAQ
2,6-DBEAQ
DCDHAQ
BTMAP-Vi
BPP-Vi
AQDP
1,6-PFP
2,6-DPPEAQ
1,6-DPAP
2,7-PFP
BRS
1,6-DAAP
2,3-DHAQ*
AQDS(NH4)2
(SPr)2Vi
1,8-PFP
BTMAP-Vi
bislawsone
MV
AQDS
4C7FL
DHPS
PEGAQ
4C7FL
2,6-D2PEAQ
[(NPr)2TV]Cl4
(NPr)2TTz
2,7-DPAP
2,6-DHAQ*
1,8-DGAP

2.7 Conclusion

2,6-D2PEAQ achieves high solubility through the use of a branched side chain that hinders precipitation and results in a solubility 10X higher than the unbranched analog. The branched side chain also improves the stability of the molecule, allowing cell cycling to be performed at high concentrations with fade rates of 0.02%/day.

When compared to other reported flow battery negolytes, 2,6-D2PEAQ has demonstrated the highest energy density of extremely slow-fading molecules. Additionally, it also demonstrates the slowest fade rate of any molecule that has been tested at negolyte densities of >55 Ah/L.

Chapter 3: 2-BEAQ – A hydrogel-forming anthraquinone

Abstract:

2-BEAQ was synthesized with the goal of creating a molecule that was cheaper than 2,6-DBEAQ with similar high stability. The single-side chain results in a molecule that shows gel-like properties. Characterization of the gel was carried out and it was utilized in a gel battery to achieve a maximum power density of 11.2 μW/μL in a hard-sided battery.

3.2 Motivation and synthesis of 2-BEAQ

For anthraquinones to be commercially viable flow battery electrolytes, they must be able to be synthesized at an adequately low cost.[100] Although making molecules more stable increases the maximum possible synthetic cost by decreasing the frequency with which degraded electrolyte needs to be replaced, 2,6-DBEAQ is still estimated to be too expensive for redox flow batteries. This is partly due to the high cost of the starting material 2,6-dihydroxyanthraquinone.

An attempt to prepare a less-expensive molecule was made by replacing 2,6-dihydroxyanthraquinone with 2-hydroxyanthraquinone. While it's challenging the estimate the cost of chemicals at large scales due to changes in the cost of production at scale and high levels of variation between suppliers and across time, 2-hydroxyanthraquinone is generally cheaper and available at larger scales than 2,6-dihydroxyanthraquinone from most suppliers (Table 3.1). There have also been reported syntheses of 2-hydroxyanthraquinone using phenol and phthalic anhydride as starting materials, which are both inexpensive feedstock chemicals.[101,

[102] This route also has the benefit of halving the stoichiometric amount of side chain needed. The resulting anthraquinone was named 2-BEAQ (**b**utyric **e**ther **a**nthra**q**uinone).

Table 3.1: Comparison of lab-scale costs of 2-hydroxyanthraquinone and 2,6-dihydroxyanthraquinone

	2-hydroxyanthraquinone cost	2,6-dihydroxyanthraquinone cost
Millipore Sigma	$96.80 for 25g	$234.00 for 5g
AK Scientific	$543 for 100g	$798 for 25g
Astatech	$464 for 100g	$557 for 100g
Biosynth/Carbosynth	$577.50 for 100g	$346.50 for 10g
Ambeed	$88 for 25g	$546 for 100g

Prices as of June 11, 2022. Because equivalent sizes of different chemicals are often not available, the largest available size from each supplier was chosen. Suppliers were chosen based on having publicly available pricing for each chemical.

2-BEAQ was prepared by reacting 2-hydroxyanthraquinone with ethyl 4-bromobutyrate, using potassium carbonate as a base. This was followed by vacuum filtration and hydrolysis and

potassium hydroxide to produce the final product (Figure 3.1. full synthetic details in Appendix A).

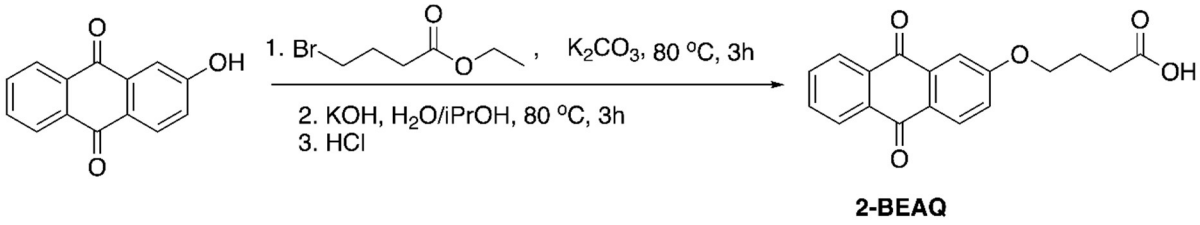

Figure 3.1: Synthesis of 2-BEAQ. 2-BEAQ was synthesized by the addition of an ethyl 4-bromobutyrate to 2-hydroxyanthraquinone followed by hydrolysis and precipitation with hydrochloric acid.

3.3 Gel-behavior and characterization of 2-BEAQ

Upon preparing a 0.1 M solution of BEAQ at pH 14, it was found that the material dissolves to form a gel. This gel persisted when the pH was lowered by the addition of acid. Further studies showed that 2-BEAQ was able to form a gel at concentrations ranging from 0.5% to 6% by mass in pH 14 solution (Figure 3.2). Gels at 0.5% and 1% 2-BEAQ by mass showed delayed gelation, while gels at higher concentrations formed instantly. At 0.25% 2-BEAQ concentration no gel formed, and a seemingly Newtonian solution was observed. The solutions exhibited shear-thinning behavior and a transition to solution-like behavior at increased temperatures.

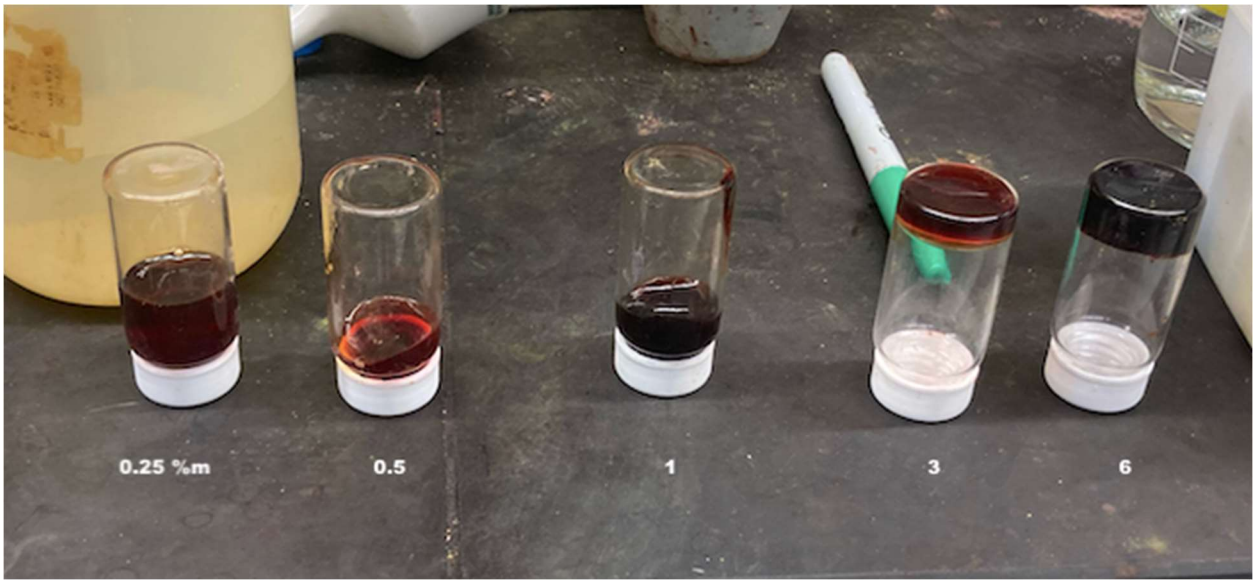

Figure 3.2: Gelation of 2-BEAQ. BEAQ solutions at 0.25 to 6% BEAQ by mass. All solutions over 0.25% show gelation behavior. Solutions over 3 % by mass are rigid enough to adhere to the top of the glass scintillation vials.

Prior research has demonstrated that select anthraquinones act as small molecule gelators in either organic solvents[103-109] or water[110, 111]. Supramolecular hydrogelators in general have been used in sensors, biomaterials and display technologies.[112] Anthraquinones have been used as chromophores and in display technologies, particularly when covalently linked to steroid motifs.[103, 110] They have also been demonstrated as sensors[106, 108] and proposed as herbal medications[111].

To test the stability of 2-BEAQ as a gel, thermal decomposition studies were performed. Because 0.1 M BEAQ solution reverts to a solution phase at elevated temperatures, the thermal decomposition studies were carried out both at room temperature (in gel form) and 65 ºC (at which temperature a solution was formed) for one week. Both samples were shielded from light. The elevated temperature sample was seen to reform a gel upon cooling. NMR samples were

taken before and after the heating period in D_2O (Figure 3.3). No new peaks were seen to form during this time period at room temperature, but at 65 ^oC new peaks consistent with side chain loss were observed.

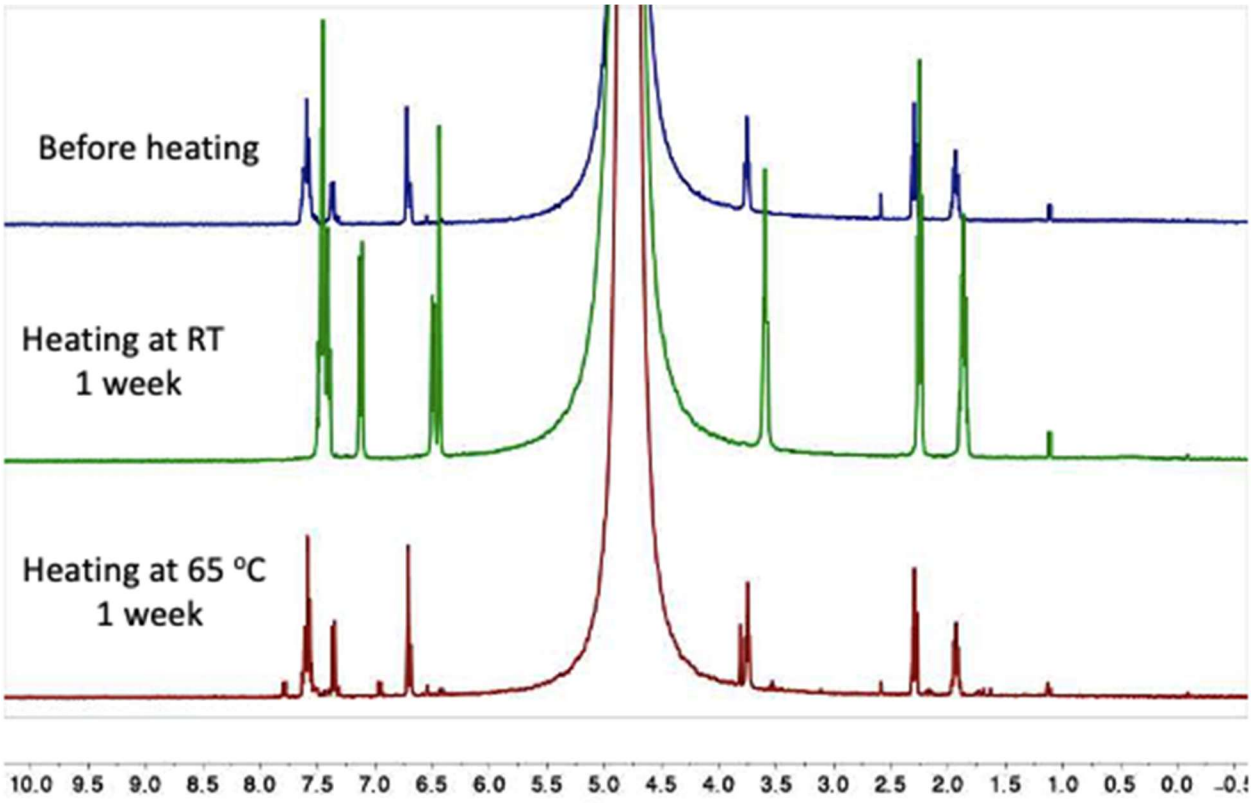

Figure 3.3: Thermal decomposition study of 2-BEAQ. NMRs of BEAQ before and after thermal decomposition studies. Samples were briefly heated until a solution was formed to allow pipetting. Each NMR sample comprises 0.1 mL of 0.1 M BEAQ solution at pH 14 and 0.5 mL of D_2O. The slight shifting of peaks in this sample is attributed to minor fluctuations in pH.

Rheology studies were performed to characterize the BEAQ gel. A 0.1 M pH 14 gel was used. Rheology measurements were collected using a Bard Discovery RH3 rheometer. Measurements of both the storage and loss moduli at different strains and frequencies were collected (Figure 3.4). Both moduli were relatively flat across the range of frequencies studied.

These measurements showed a decrease in both the storage moduli (G') and loss moduli (G'') with increasing temperature. Both values remained relatively constant with frequency but decreased at high oscillation stress values. The storage moduli were higher than the loss moduli at a given temperature at all frequencies and at low oscillation stresses. At oscillation stresses above a certain threshold, which decreases as temperature increases, the loss moduli become higher than the storage moduli as 2-BEAQ transitions into a solution-like state. In gels, the storage modulus exceeds the loss modulus by at least an order of magnitude, which is not the case for 2-BEAQ.[113] Therefore 2-BEAQ can be classified as a weak gel.

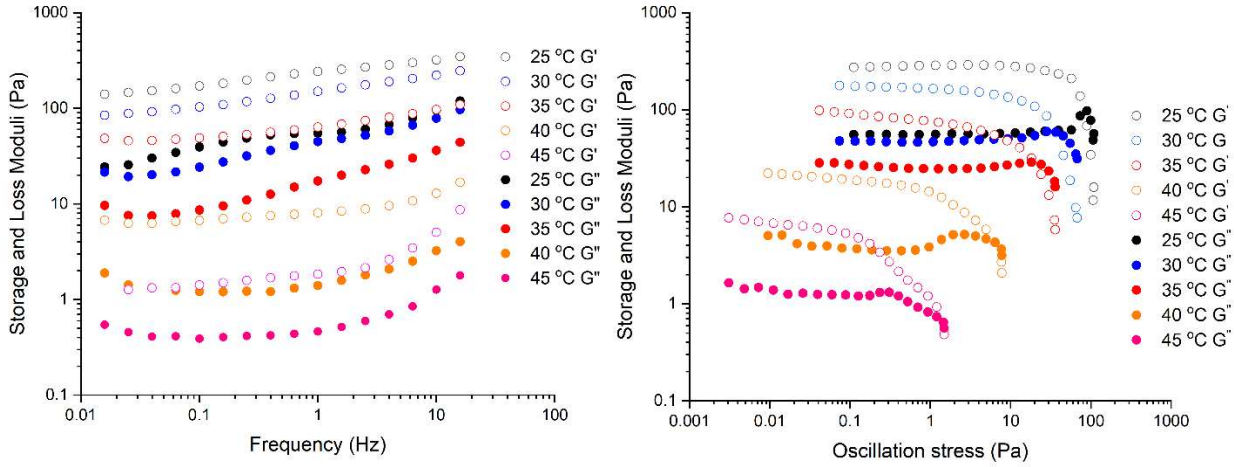

Figure 3.4: Rheology measurements of 2-BEAQ. The storage modulus, represented with hollow circles is larger than the loss modulus, represented by filled circles at each temperature range. Measurements produced in collaboration with Dr. Andrew Wong and Harvard University's Weitzlab Rheology Center

The temperature at which the gel-to-solution transition happened was characterized using differential scanning calorimetry (DSC). A 0.5% by mass sample of BEAQ by mass was placed in an aluminum pan and sealed followed by holding the temperature at 10°C for 10 minutes,

ramping the temperature to 60 ºC at 4 ºC per minute. The temperature was then held for 10 minutes before being ramped back to 10 ºC at 4 ºC/minute. The results are shown in Figure 3.5.

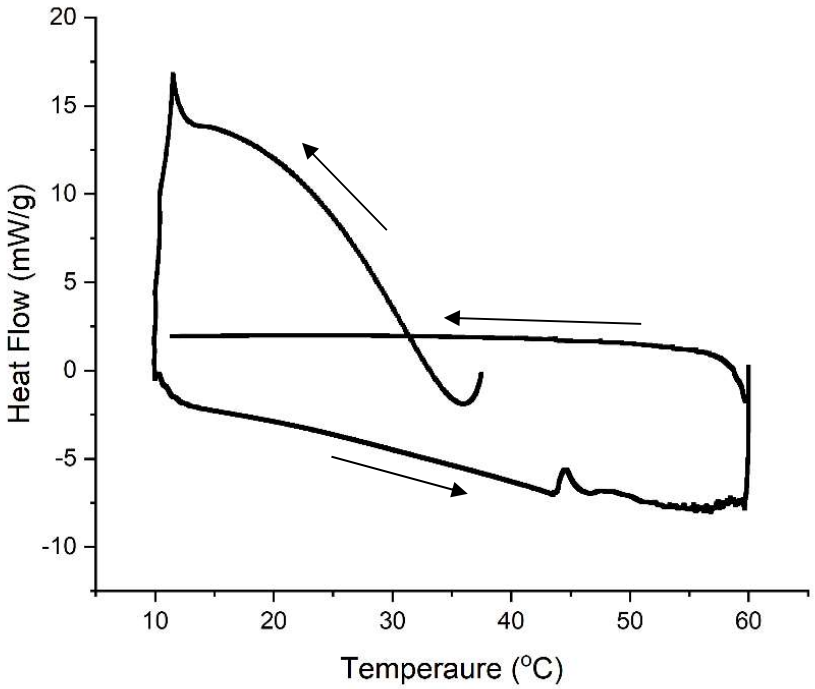

Figure 3.5: Differential Scanning Calorimeter results of 2-BEAQ.

The DSC shows an exothermic peak at 44 ºC upon heating where less heat was needed to flow into the sample to maintain a temperature equal to the control plate. This can be attributed to the heat released when 2-BEAQ transitions to the gel form.

Scanning electron microscopy was used to image a sample of 6% by mass 2-BEAQ that was prepared as a gel in potassium hydroxide at pH 14. The gel was vacuum dried followed by a layer of 10 nm platinum being sputtered on the dried surface. Surface imaging revealed a rough and porous surface with some ribbon-like features at the micrometer scale. Areas of crystallinity

were also observed, which may be attributed to either potassium hydroxide or crystalized anthraquinone (Figure 3.6).

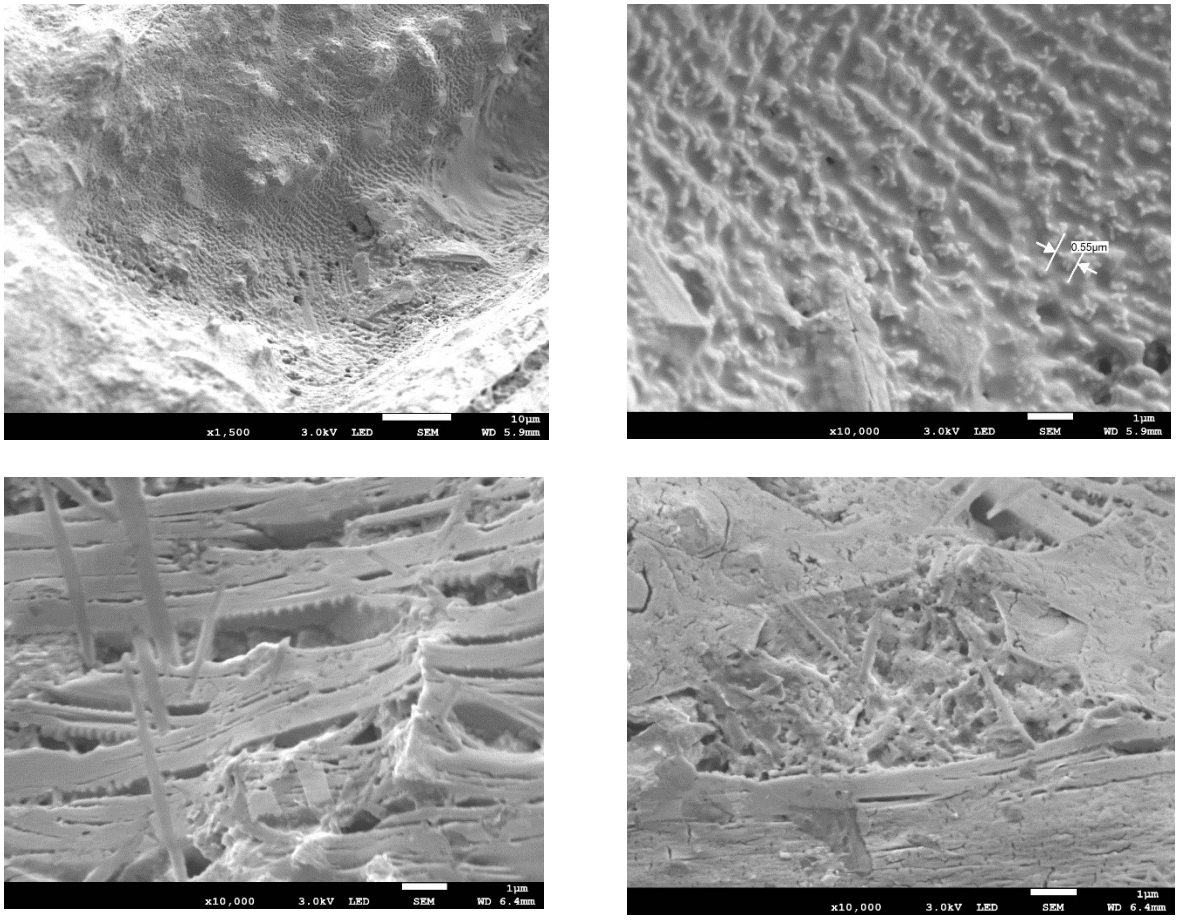

Figure 3.6: SEM of 2-BEAQ. SEM images of 6%/mass2- BEAQ vacuum dried and sputtered with 10 nm of platinum show a rough surface with ribbon-like structures on the micrometer scale. Images acquired with help from Harvard University Center for Nanoscale Systems.

The electrochemical behavior of 2-BEAQ was explored using cyclic voltammetry. A scan rate of 0.1 V/s was applied to a 1 mM solution at pH 14 in KOH. 2-BEAQ behaves like a Newtonian solution at this concentration with no signs of gel-like behavior. The CV showed a reduction potential of -422 mV vs. SHE, which is similar to other ether-linked anthraquinones

including the disubstituted 2,6-DBEAQ.[29] The curve showed a peak separation of 52 mV, indicating quasi-reversible redox kinetics (Figure 3.7). Further rotating disk electrode studies done by collaborators in the lab of Dr. Frank Crespilho found the diffusion coefficient of 2-BEAQ was 3.04 *10^{-6} at pH 14.

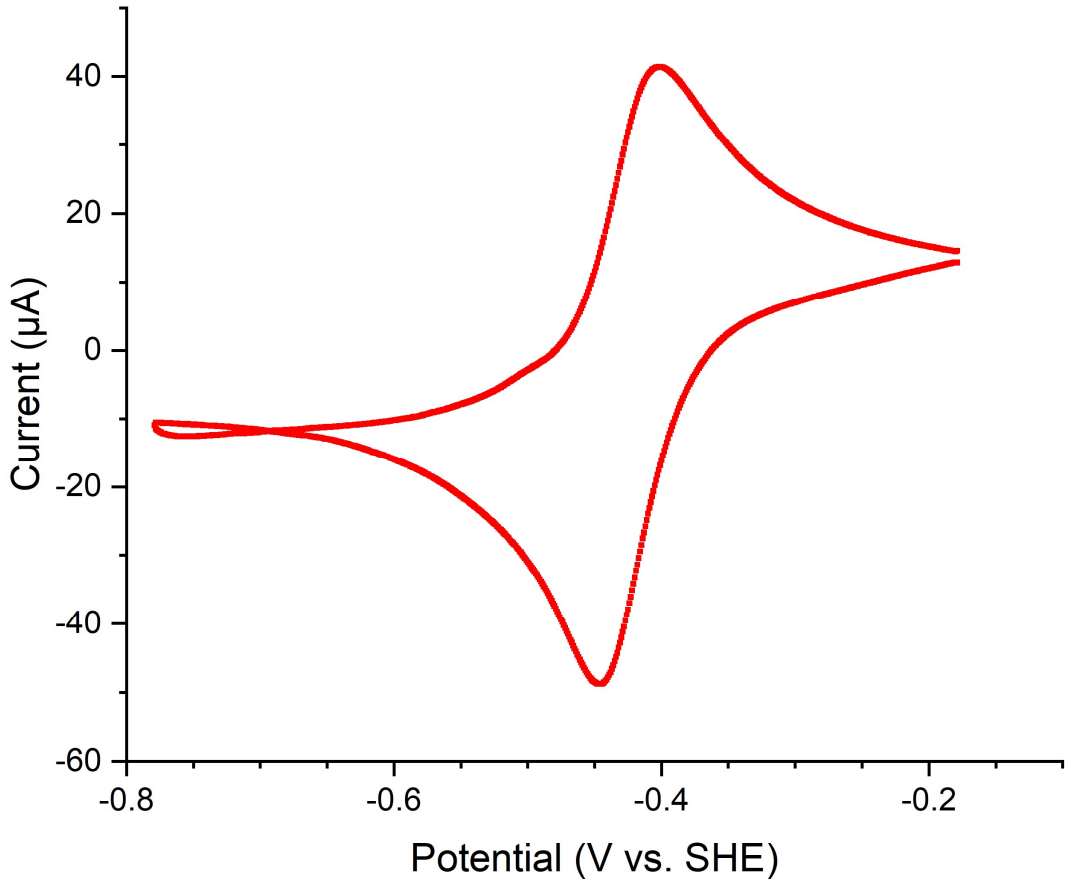

Figure 3.7: CV of 2-BEAQ at pH 14.

In further studies in Dr. Crespilho's lab, 2-BEAQ was observed to change color from a green gel to a more free-flowing red liquid upon charging. spectroelectrochemical studies were done on 2-BEAQ held at different potentials to obtain spectra of the molecule at voltages between -0.4 and -0.9 V (Figure 3.7). At -0.4 V most 2-BEAQ molecules are in their oxidized

form while at -0.9 V most are in the reduced form. The peaks at 425 nm and 474 nm disappear or decrease in size while the two peaks at 251 and 291 begin to merge as the molecules are oxidized. The peaks shift most dramatically between 0.65 V and 0.6 0V against a silver/silver chloride electrode, which is consistent with the reduction potential demonstrated by cyclic voltammetry.

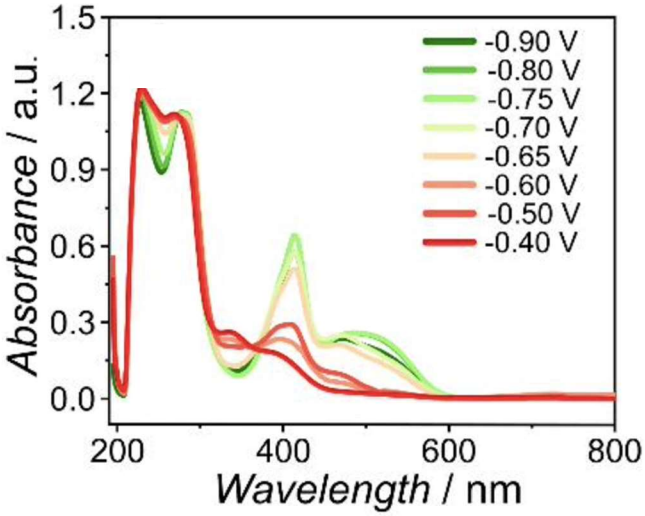

Figure 3.8: Spectroelectrochemistry of 2-BEAQ. UV-Vis spectra of 2-BEAQ were taken at -0.90 to -0.40 V v Ag/AgCl using a homemade flexible carbon fiber working electrode. Increasing potentials show 2-BEAQ as it is converted from the reduced to the oxidized form. Data were collected, processed, and graphed in Dr. Frank Crespilho's lab.

3.4 2-BEAQ as a gel battery electrolyte.

2-BEAQ behaves as a Newtonian fluid only at low concentrations, which makes it an unsuitable candidate for flow batteries at ambient temperatures. However, its gelation properties make it a better fit for flexible battery designs, which have been proposed for wearable devices,

portable devices that are subject to bending and folding, and biomedical applications.[114, 115] Gels have been used to create a variety of components in flexible batteries.[115-121]

To determine the suitability of 2-BEAQ for battery applications, Dr. Andrew Wong tested the resistivity and conductivity of 2-BEAQ. In the absence of heating, a 0.1 M solution of BEAQ in 1 M KOH solution had a resistivity of 5.58 ± 0.33 Ω/cm and a conductivity of 0.180 ± 0.011 S/cm. When 2-BEAQ was heated to its solution form the values were not significantly different, with a resistivity of 5.64 ± 0.29 Ω/cm and a conductivity of 0.177 ± 0.008 S/cm. In addition, 2-BEAQ as a gel exhibits similar conductivities to traditional flow battery electrolytes, including 2-2PEAQ (see Chapter 4) which has a conductivity of 0.163 S/c, at 0.1 M at room temperature (2-2PEAQ conductivity measurement taken by Dr. Kiana Amini).

A preliminary assessment of 2-BEAQ cycling performance was done by cycling a 0.1 M solution of 2-BEAQ (200 μL) at pH 14 in a static cell against 0.5 M potassium ferrocyanide and 0.05 M potassium ferricyanide (900 μL) with a Sigracell GFA-3EA electrode and Nafion 212 membrane. Because static cells do not require the electrolytes to be pumped, this allowed an initial assessment of cell behavior of 2-BEAQ without being hindered by the gel properties of the solution (Figure 3.9). The static cell of 2-BEAQ initially showed a high although volatile efficiency. 2-BEAQ was able to cycle reversibly from 20 hours before the experiment was ended. In that time capacity dropped from 3.2 to 2.8 C, but it is unclear to what extent this is due to electrolyte decomposition as opposed to cell leakage. Over 400 cycles the time the cell spent in each cycle at constant current before hitting the current cutoff and switching to potentiostatic cycling decreased, indicating an increasing cell resistance. The cause of the increased resistance is unknown.

a. b.

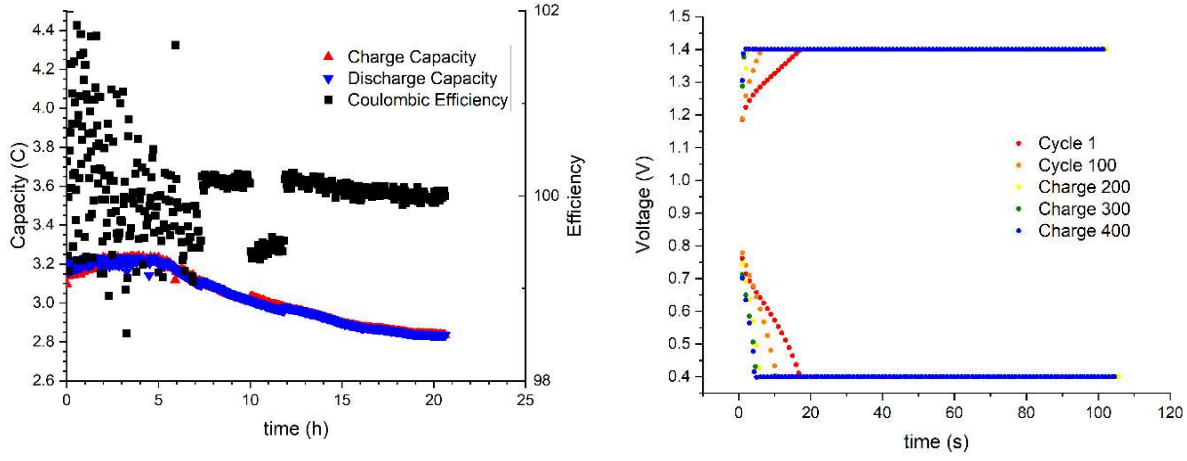

Figure 3.9: Static cell cycling of 2-BEAQ. a. Charge capacity, discharge capacity, and efficiency of 2-BEAQ static cell. b. Voltage vs. time curves at representative cycles. The static cell was run by Dr. Drew Wong.

2-BEAQ was then tested in a gel battery. Because both potassium ferrocyanide and potassium ferricyanide dissolve in water and do not form gels, xanthan gum was used to create a gel for the posolyte side of the battery. 40 mg/mL xanthan gum in 1 M KOH solution with 0.2 M potassium ferrocyanide was used as the posolyte. 100 µL of this gel along with 100 µL of 0.05 M BEAQ in 1 M KOH were separated by a Nafion 212 membrane and flexible carbon fiber array electrodes. Leakage was prevented by the use of Viton gaskets followed by encasing the battery in silicone resin (Figure 3.9). This was encased in a hard acrylic container.

The resulting battery was able to discharge $1.38 * 10^{-3}$ mAh/µL (4.99 mC/µL), of which $8.4 * 10^{-4}$ mAh/µL (3.05 mC/µL) was discharged. This represents access of 52% of the

theoretical capacity on charging and a coulombic efficiency of 61% (Figure 3.10b). The cell was cycled at 40 mA/cm^2 for 200 cycles. An initial rapid loss in capacity was observed followed by more stable cycling from cycle 50 to 200. Polarization curves demonstrated a maximum power density of 11.2 μW/μL at 50% SOC (Figure 3.10c). This is a large enough power to supply energy to wearable sensors including cuffless blood pressure sensors, pressure sensors, and temperature sensors, although the longer-term cycling of the battery would have to be optimized.[122-126] Ten charge and discharge cycles are provided in Figure 3.10d.

a.

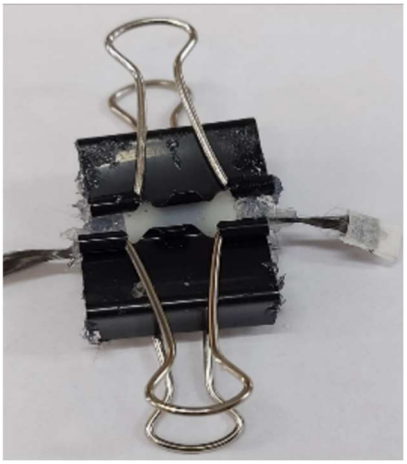

b.

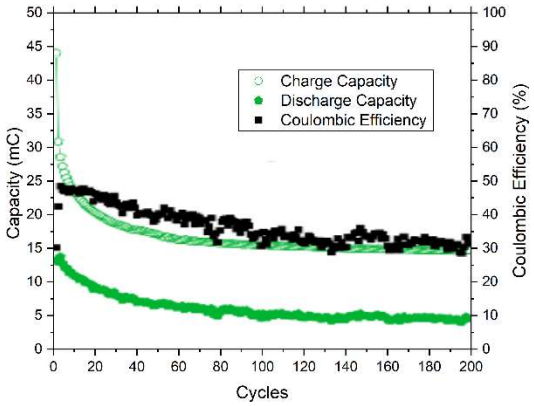

c.

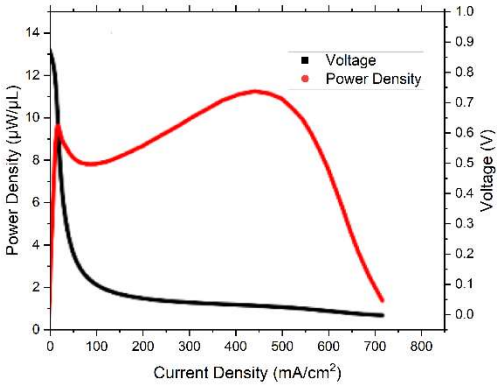

d.

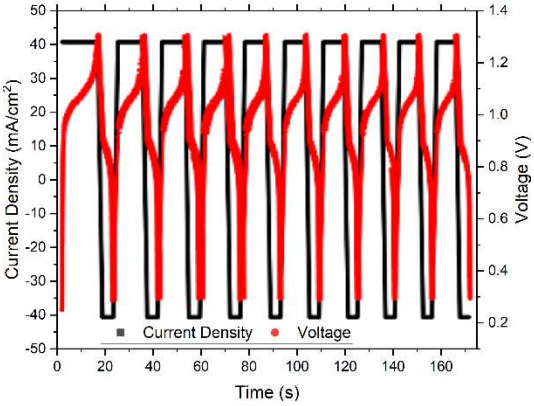

Figure 3.10: 2-BEAQ hard-sided cell cycling performance. a. Photograph of the hard-sided 2-BEAQ/ferrocyanide gel battery. b. Charge and discharge capacity of 2-BEAQ/ferrocyanide gel battery. c. Polarization curves show a maximum power density of 1.12 μW or 11.2 μW/μL at 50% SOC. d. Current and voltage measurements for ten cycles. The battery was designed, prepared, and run and figures were prepared in the lab of Dr. Frank Crespilho. The original axes have been replotted for clarity.

To test the gel-electrolytes in a flexible, rather than hard-sided, battery a second cell was prepared. Instead of a hard acrylic casing, this battery used two rectangular pieces of commercially available waterproof textile and sealed the battery with hydrophobic double-sided tape and silicone resin. An image of this battery is shown in Figure 3.11a. Polarization curves revealed a peak power density of 1.3 µW/µL, much lower than the hard-backed battery (Figure 3.11b).

a. b.

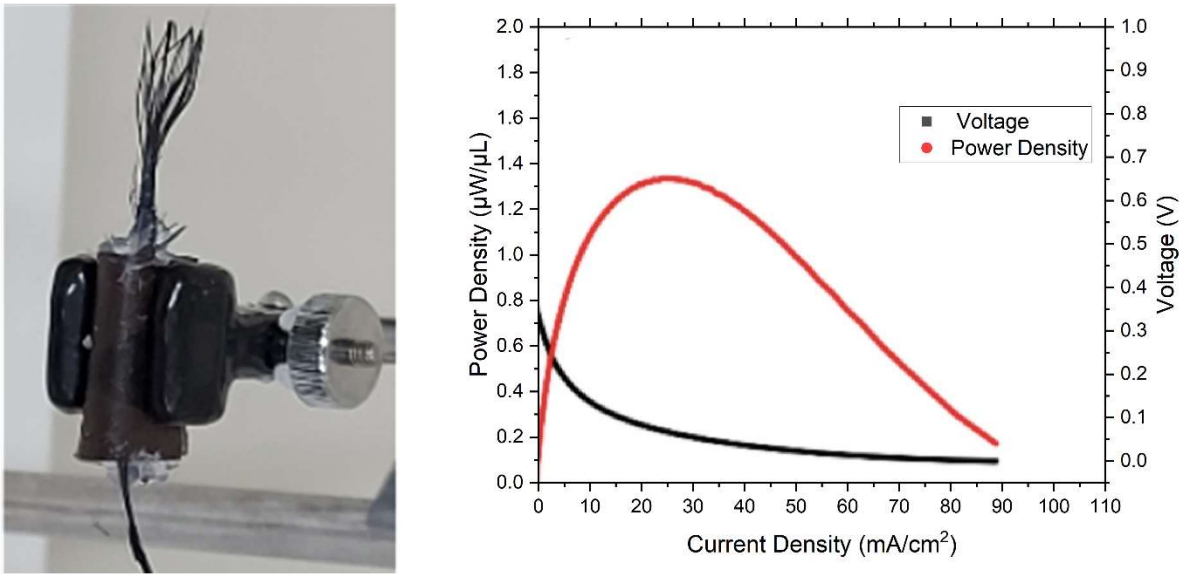

Figure 3.11: Flexible battery performance of 2-BEAQ. a. Photograph of a wearable gel battery containing 2-BEAQ negolyte and ferrocyanide in xantham gum posolyte at pH 14. b. Polarization curves of the flexible gel battery demonstrated a maximum power density of 1.3 µW/µL. The cell was designed and run, and the images are from the lab of Dr. Frank Crespilho. The axes have been replotted for clarity.

3.5 Conclusions

2-BEAQ exhibits unusual solution properties, possibly because of the intermolecular interactions caused by the negatively charged carboxylate on the single side chain interacting in an ordered manner with water molecules and other anthraquinones in alkaline aqueous solutions. This results in a gel-like behavior that makes the molecule unsuitable for traditional flow battery applications because it cannot be pumped. However, it makes the molecule a good fit for flexible batteries. Both a hard-sided and a flexible battery were fabricated. The hard-sided battery was cycled reversibly and demonstrated a maximum power density of 11.2 μW/μL. Further optimization is ongoing to improve the performance of 2-BEAQ when used as an electrolyte in a flexible battery enclosure.

Chapter 4: Search for a cheaper quinone and an understanding of substitution-based stability effects

Abstract

2-2PEAQ, a singly substituted anthraquinone containing a branched side chain, was designed and synthesized to match the strong performance of 2,6-D2PEAQ in a simpler molecular structure. This structure was used to systematically study the decomposition pathways, which were found to be a mix of side chain loss and anthrone formation and to systematically compare the capacity losses of alpha and beta substituted anthraquinones.

4.2 Synthesis and chemical characterization of 2,2PEAQ and 1,2PEAQ

The extremely high solubility demonstrated by 2,6-D2PEAQ (Chapter 2) suggested that the use of a branched side chain might allow singly substituted anthraquinones to maintain a high enough solubility and appropriate solution behavior to be practical electroactive materials in flow batteries. To this end, 2-2-**p**ropionate **e**ther **a**nthra**q**uinone (2-2PEAQ) (Figure 4.1) was synthesized. Synthetic details can be found in Appendix A. While this material did not demonstrate solubility as high as the disubstituted analog, it was found to have a solubility of about 1 M at pH 14 compared to less than 0.1 M for 2-hydroxyanthraquinone with no side chain attached.[127]

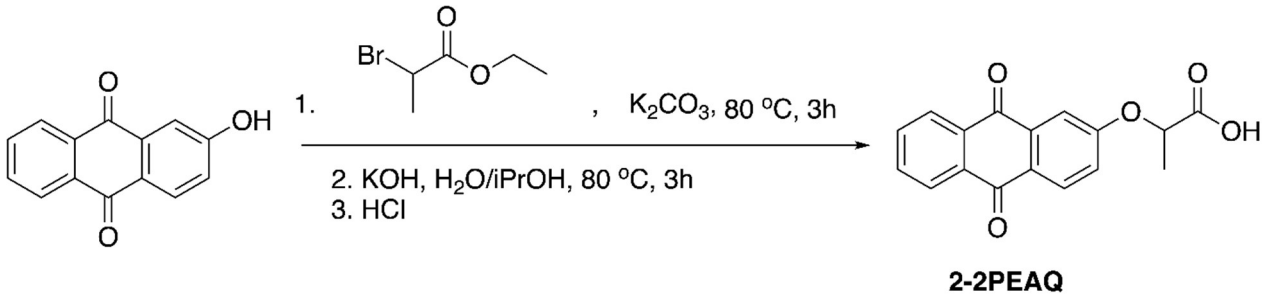

Figure 4.1: Synthesis of 2-2PEAQ. 2-2PEAQ is synthesized in an analogous process to 2,6-D2PEAQ that substitutes the expensive 2,6-dihydroxyanthraquinone starting material with the much cheaper 2-hydroxyanthraquinone.

The stability of 2-2PEAQ was determined by taking NMR spectra before and after heating the sample for 1 week at 65 °C in both the oxidized and the reduced form. Following heating, the reduced form was oxidized by agitating the solution in room air for thirty minutes. 100 µL of each sample was separately diluted with 500 µL of D_2O. The resulting NMRs are shown in Figure 4.2. No new peaks are observed in either post-heating NMR, indicating the 2-2PEAQ is resistant to thermal decomposition on the timescale studied.

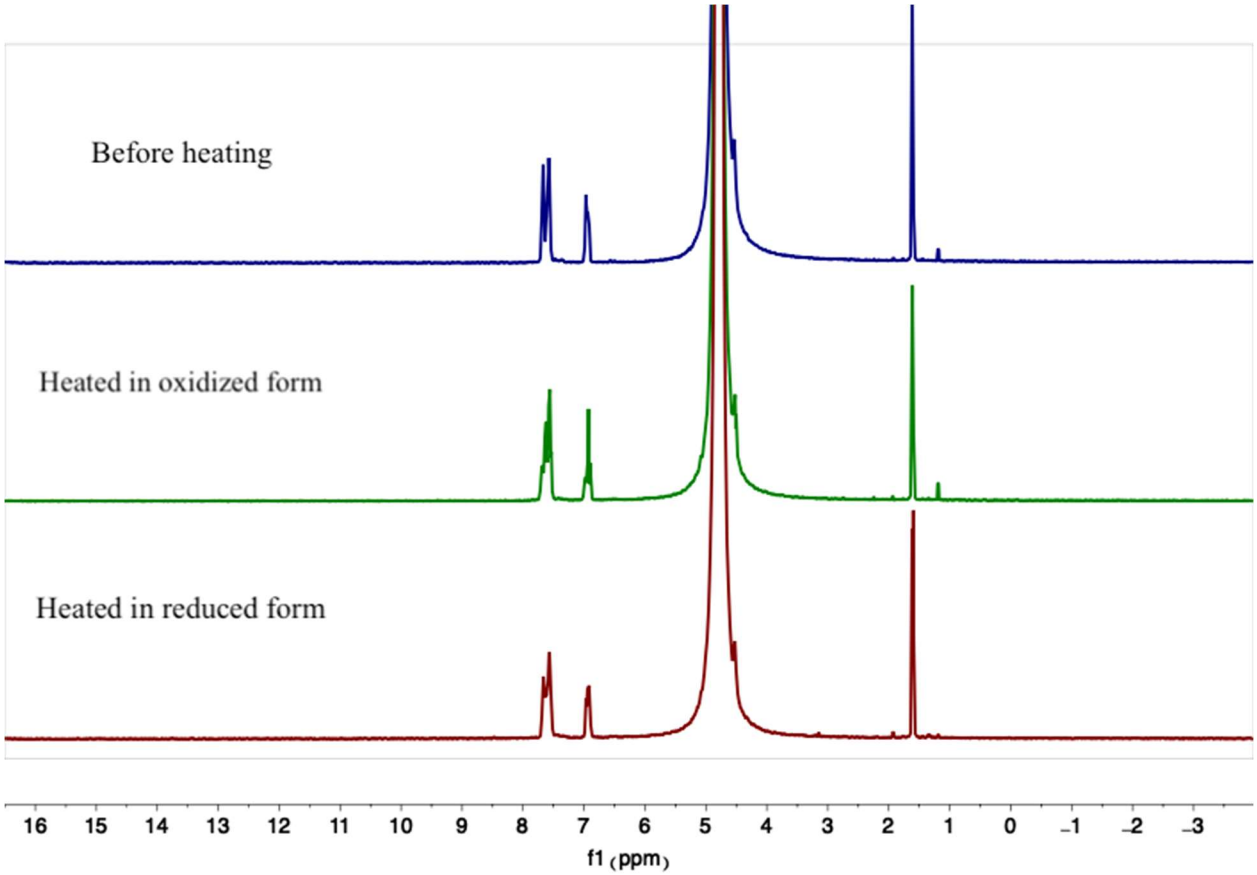

Figure 4.2: Thermal Decomposition of 2-2PEAQ. The blue trace shows a 0.1 M 2-2PEAQ solution at pH 14. The second, green, spectrum shows a 0.1 M sample heated at 65 ºC for 1 week and the bottom, red, spectrum shows a 0.1 M sample that was stored in the reduced form at 65 ºC for 1 week followed by reoxidation by agitating the solution to expose it to air.

The electrochemical properties of 2-2PEAQ were investigated using cyclic voltammetry, A single reversible set of redox peaks was observed. The redox event was centered at -424 mV and had a peak separation of 51 mV. When paired with potassium ferrocyanide (Figure 4.3a) a maximum OCV of 954 mV is estimated. To determine the number of protons involved in the oxidation and reduction of 2-2PEAQ, a Pourbaix diagram was prepared. This indicated a 2-

proton 2-electron process between pH 7 and 10.8. It then transitions to a 1-proton 2-electron process from pH 10.8 to pH 12.5 before becoming proton decoupled above pH 12.5

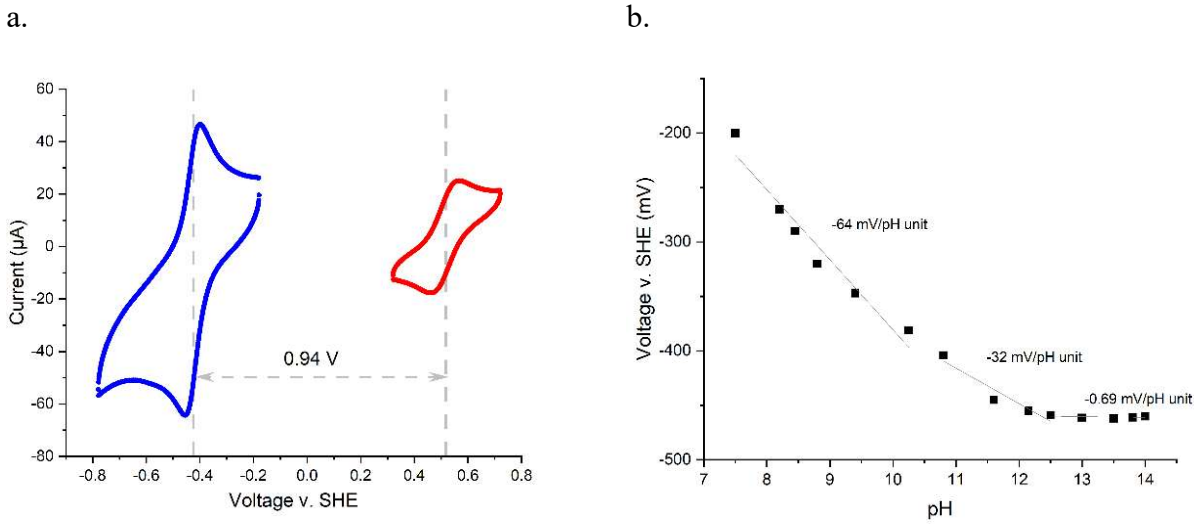

Figure 4.3: Initial Electrochemical characterization of 2-2PEAQ. a. A cyclic voltammogram of 2-2PEAQ (blue) and potassium ferrocyanide (red) Scans were performed at 0.1 V/s in degassed solution at pH 14. A blank scan is subtracted to give the final figure. b. Pourbaix diagram of the reduction potential of 2-2PEAQ against pH. Measurements were taken by Abdulrahman Alfaraidi. All cyclic voltammograms were prepared at 5 mM. All measurements below pH 12 are taken in a buffered solution to prevent pH swings.

The diffusion coefficient and kinetic rate constant for the 2-2PEAQ and its electron transfer reaction were measured using rotating-disk voltammetry as described in Chapter 2, performed by Dr. Kiana Amini. 2-2PEAQ was found to have a diffusion coefficient of 2.23×10^{-6} cm^2 s^{-1} and a kinetic rate constant of 1.75×10^{-3} cm s^{-1}, comparable to other reported anthraquinones (Figure 4.4).

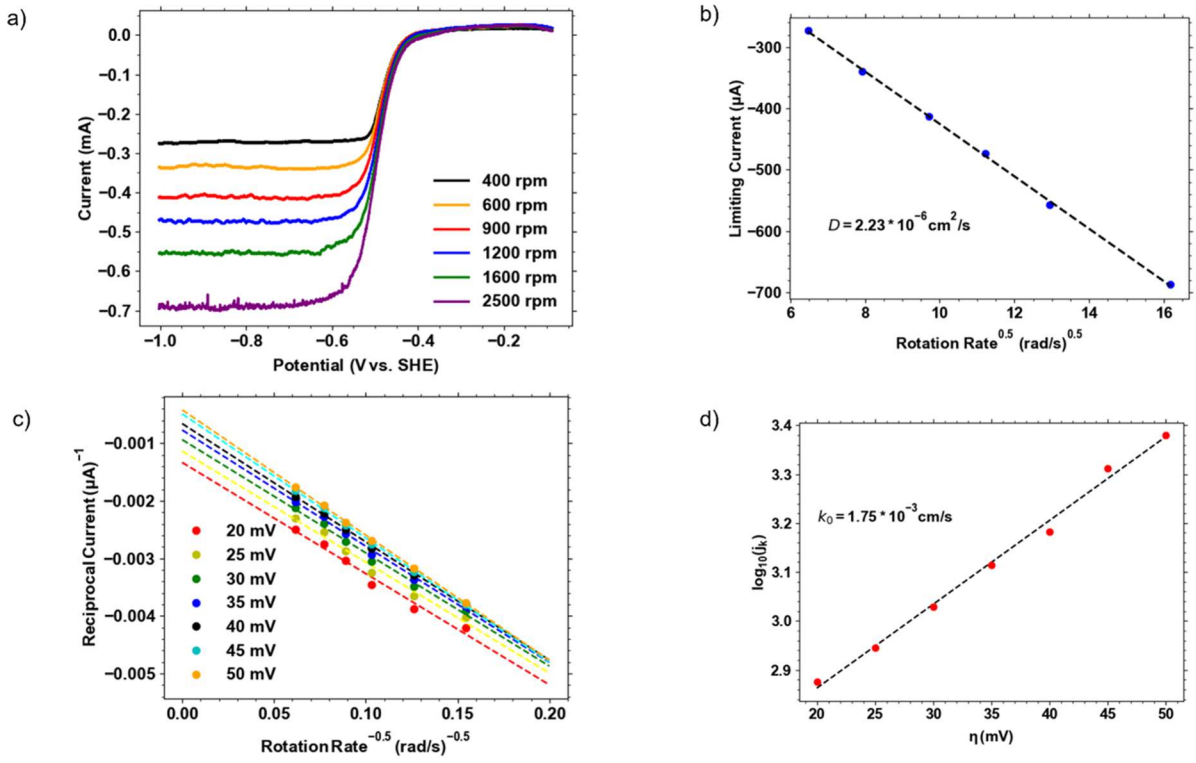

Figure 4.4: Rotating disk electrode studies of 2-2PEAQ. a. Linear-sweep voltammograms at different scan rates. b. The limiting current plotted against the square root of the rotation rate. c. At different overpotentials, the reciprocal of the current is plotted against the reciprocal square of the rotation rate. d. The base-10 log of the kinetic current, which is the inverse of the intercept at each overpotential in plot c, is plotted against the overpotential. Experiments were run and graphs were prepared by Dr. Kiana Amini.

4.3 2-2PEAQ Cell Cycling Performance

To test the performance of 2-2PEAQ in a flow cell 4.7 mL of 0.1 M 2-2PEAQ in 1 M potassium hydroxide was prepared with 50 mL of 0.1 M potassium ferrocyanide in 1 M potassium hydroxide as a posolyte. A Nafion 212 membrane and SGL AA electrodes were used in the battery (Figure 4.5). The open circuit voltage of the cell increases to 1.0 V at 90% SOC

while the polarization area specific resistance is, on average, 5.7 Ω cm^{-2}, most of which is attributed to the resistance of the Nafion 212 membrane as observed in the high-frequency resistance of 4.47 Ω cm^{-2} (Figure 4.5a). A peak power density of 42 mW/cm^2 at 90% SOC at a current density of 82 mA/cm^2 was measured (Figure 4.6b). The coulombic efficiency decreased from 100% to 95.7% as the current density was increased from 10 to 60 mA/cm^2. The voltage and energy efficiency decreased from 73% and 73% to 34.0% and 32.5% respectively (Figure 4.5d).

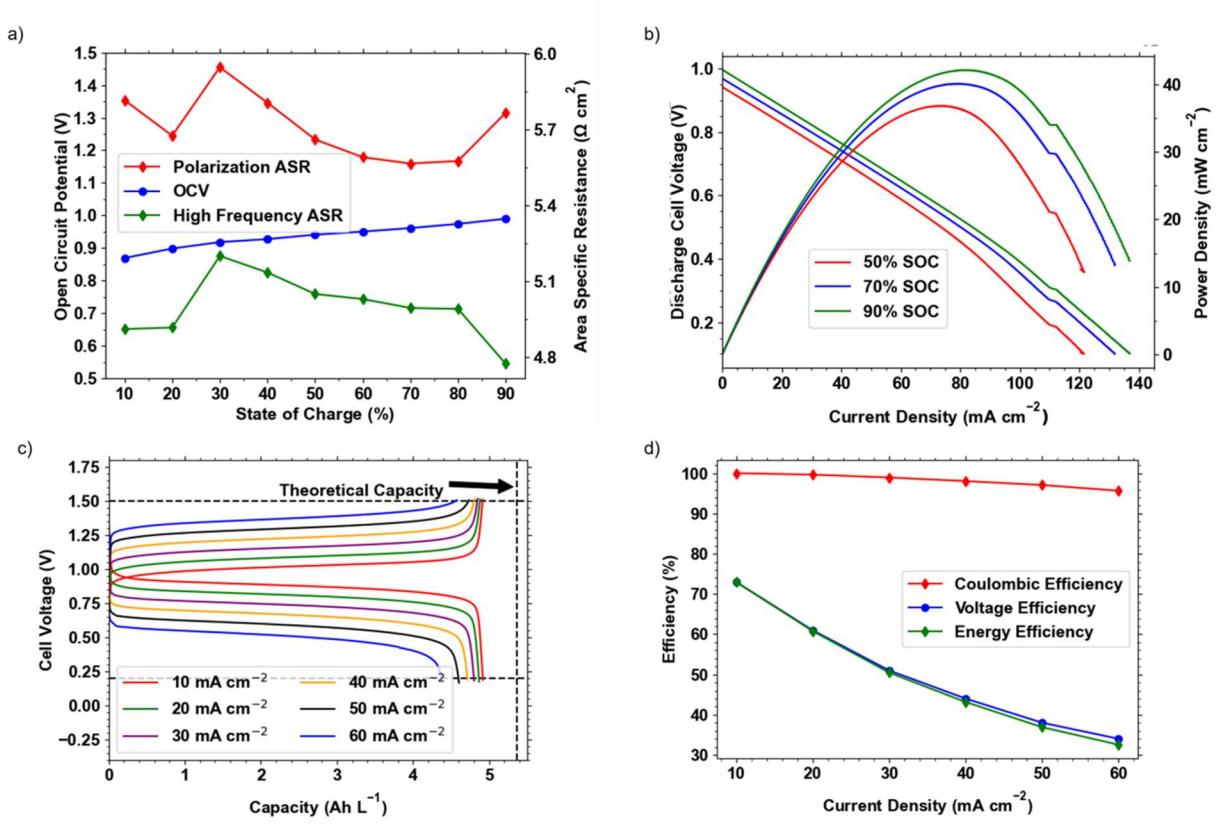

Figure 4.5: Cell performance of 0.1 M 2-2PEAQ cell in 1 M KOH. a. ASR measurement of 2-2PEAQ 0.1 M cell. b. Polarization studies of 0.1 M 2-2PEAQ cell. C. Representative charge and discharge curves at various current densities. d. Coulombic, voltage, and energy efficiencies of 0.1 M 2-2PEAQ cell. The cell run was set up and run and graphs were constructed by Dr. Kiana Amini.

The stability of 2-2PEAQ in a cell was measured at both pH 7 and pH 14 (Figure 4.6). The cells were cycled at 40 mA/cm^2 followed by potentiostatic holds at 1.3 V on charge and 0.5 V on discharge until the current dropped to 1 mA/cm^2. The negolytes contained 0.1 M of 2-2PEAQ and the posolyte 0.1 M of potassium ferrocyanide and 0.02 M of potassium ferricyanide in an excess volume to ensure the negolyte was capacity limiting. For the pH 7 cell, an additional 1 M KCl was added to both reservoirs to ensure adequate electrical conductivity.

For the pH 7 cell, 4.45 Ah/L, or 83%, of the total theoretical capacity was initially accessed. The remaining 17% is attributed to small errors in the electrolyte volume transferred to the reservoir and inorganic salts or water present in the 2-2PEAQ powder. The cell exhibited a capacity fade rate of 0.09%/day over a period of 10 days (Figure 4.6a). No new plateau in the voltage curves was observed, indicating the lack of observable new redox activity from any decomposition products (Figure 4.6b). Charge-Discharge voltage profiles showed a decrease in capacity access and an increase in resistance (the cell reaches the voltage cutoff faster) during cell cycling.

The pH 14 cell was prepared in a manner analogous to the pH 7 cell, except that the KCl was replaced with a 1 M KOH solution. Both cells used Nafion 212 membranes. The alkaline cell demonstrated a slower fade rate of 0.05%/day (Figure 4.6c). No new features were seen on the charge-discharge voltage profiles (Figure 4.6d).

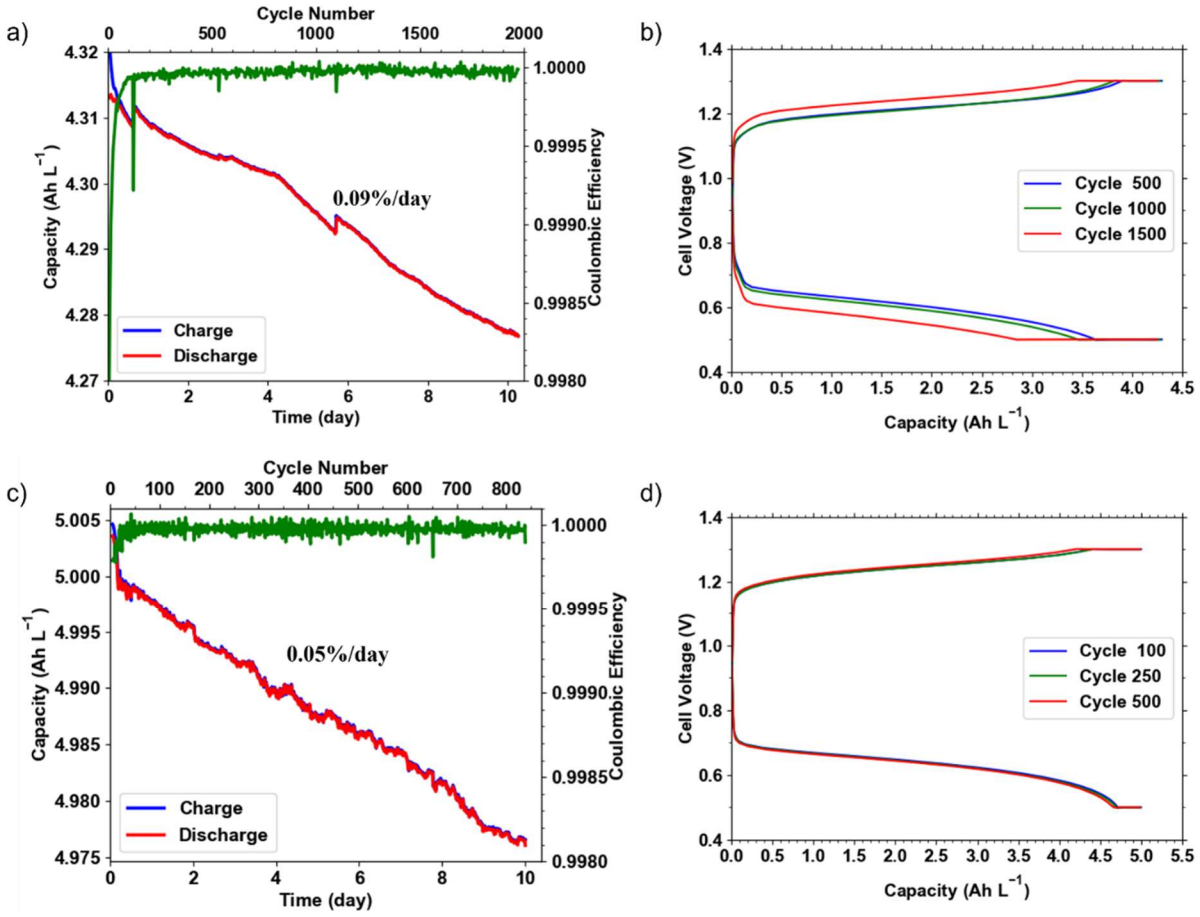

Figure 4.6: Long-term cell cycling of 2-2PEAQ at neutral and alkaline conditions. a. Capacity fade of a 0.1 M 2-2PEAQ cell at pH 7. b. Charge-discharge voltage profiles for pH 7 cell. c. Capacity fade of 0.1 M 2-2PEAQ cell at pH 14. d. Charge-discharge voltage profiles for pH 14 cell. Cell run and graphs prepared by Dr. Kiana Amini.

To evaluate the causes of capacity fade, post cycling analysis was performed on the pH 14 cell. Cyclic voltammogram of both the negolyte and the posolyte reservoirs were performed without dilution (Figure 4.7). In the posolyte reservoir only the expected potassium ferro/ferricyanide redox reaction was observed. No electrochemistry was seen at negative potentials where 2-2PEAQ would be expected and no unexpected redox chemistry was seen. Similarly, the negolyte reservoir showed only the expected peaks associated with the oxidation

and reduction of 2-2PEAQ. No peaks are seen at positive potentials, where potassium ferrocyanide and ferricyanide would be expected. Based on this data, it was concluded that crossover was too low during cell cycling to be detected using cyclic voltammetry.

a. b.

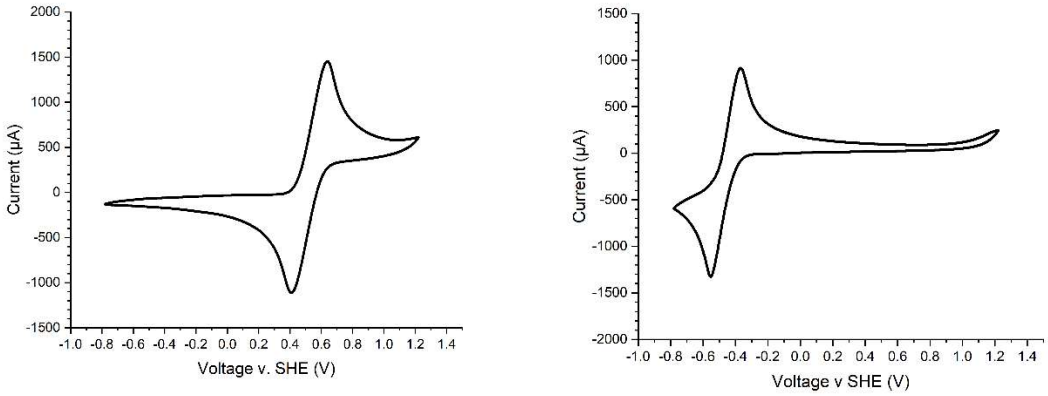

Figure 4.7: Post cycling cyclic voltammetry analysis of 2-2PEAQ 0.1 M pH 14 cell. CV measurements of both the posolyte and negolytes reservoir were taken at 0.1 V/s over the range of -0.78 to 1.22 V vs. SHE. The second cycle of each is plotted. a. Cyclic voltammogram of the posolyte reservoir. b. Cyclic voltammogram of the negolyte reservoir.

NMR was used for an initial study of molecular decomposition. proton and carbon-13 NMRs were obtained on a Bruker AVANCE NEO400 MHz instrument. No unexpected peaks were seen on either carbon NMR (Figure 4.8) or the proton NMR of the ferrocyanide reservoir (Figure 4.9). This is consistent with the lack of observable crossover seen in cyclic voltammetry studies.

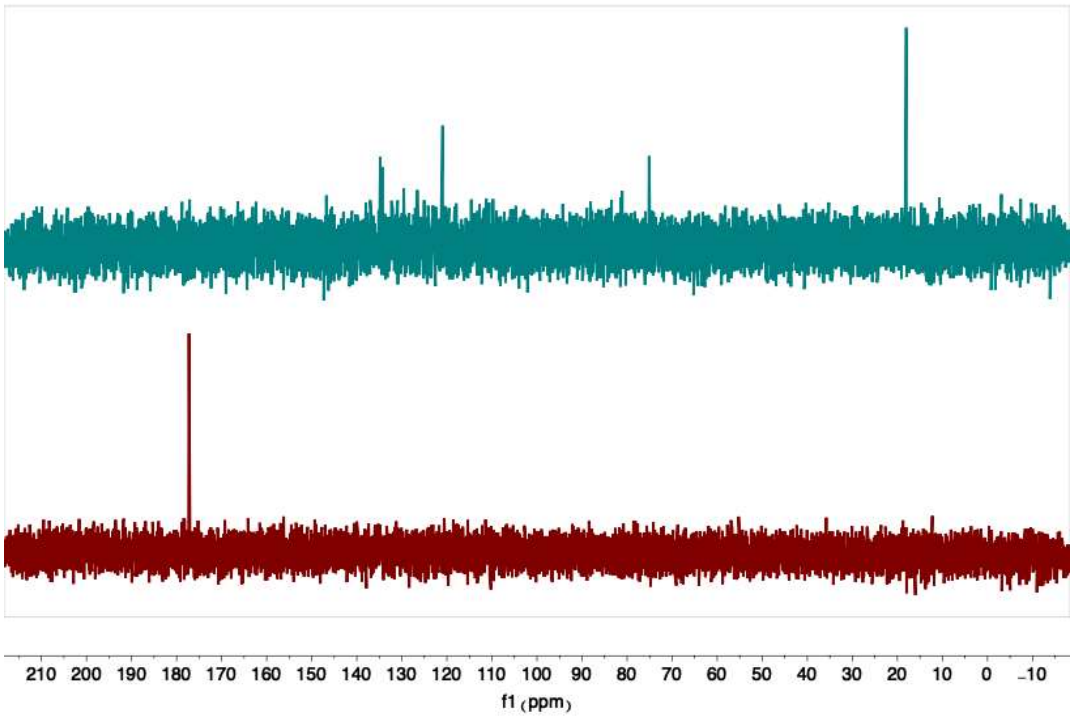

Figure 4.8: Post-Cycling ^{13}C-NMR spectra of pH 14 2-2PEAQ cell. The negolytes reservoir (blue, top plot) has peaks at 134.7, 134.3, 75.1, and 18.04. The carbon NMR of the posolyte reservoir (red, bottom plot) shows a single peak at 177.2.

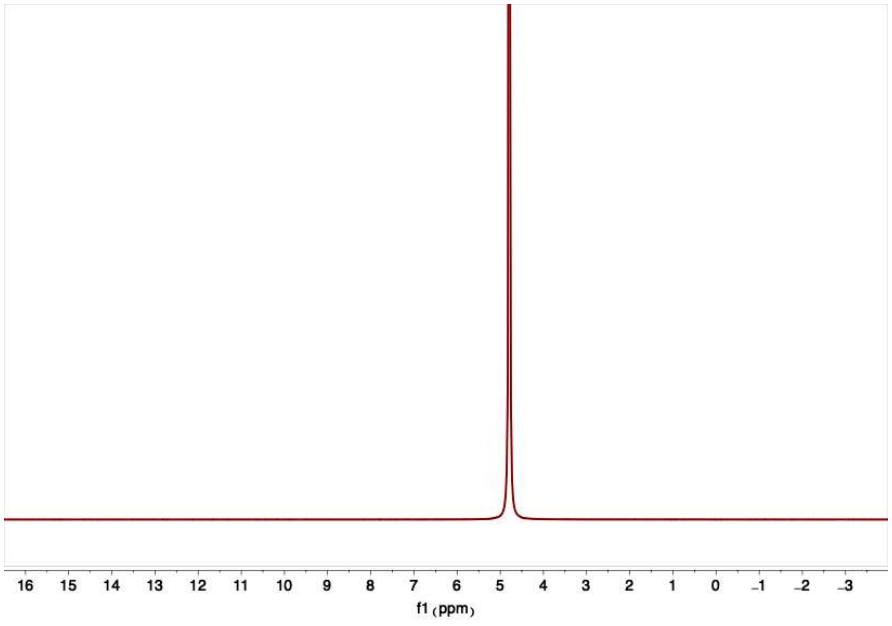

Figure 4.9: ^{1}H NMR of posolyte reservoir of pH 14 0.1 M 2-2PEAQ cell.

^{1}H NMR of the negolyte did reveal new peaks in the aromatic region immediately upfield (right) of the original 2-2PEAQ peaks (Figure 4.10). The 2-2PEAQ spectrum developed 3 new peaks at 7.30, 6.45, and 1.85 ppm. The peak at 1.85 ppm may correspond to a decomposition peak of potassium pyruvate. The new aromatic peaks were identified as belonging to 2-hydroxyanthraquinone, which would be consistent with a decomposition mechanism of side-chain loss. A new peak is observed in the aliphatic region as a singlet at 1.87 that may belong to the lost side chain or a decomposition product of the side chain, however, it does not correspond to the peaks expected of potassium lactate or potassium acrylate at the same pH. Potassium pyruvate, which could form if lactate was oxidized in the solution, forms several additional peaks in alkaline solution due to reactions with itself and water, one of which aligns with the new peak in the post-cycling NMR of 2-2PEAQ.

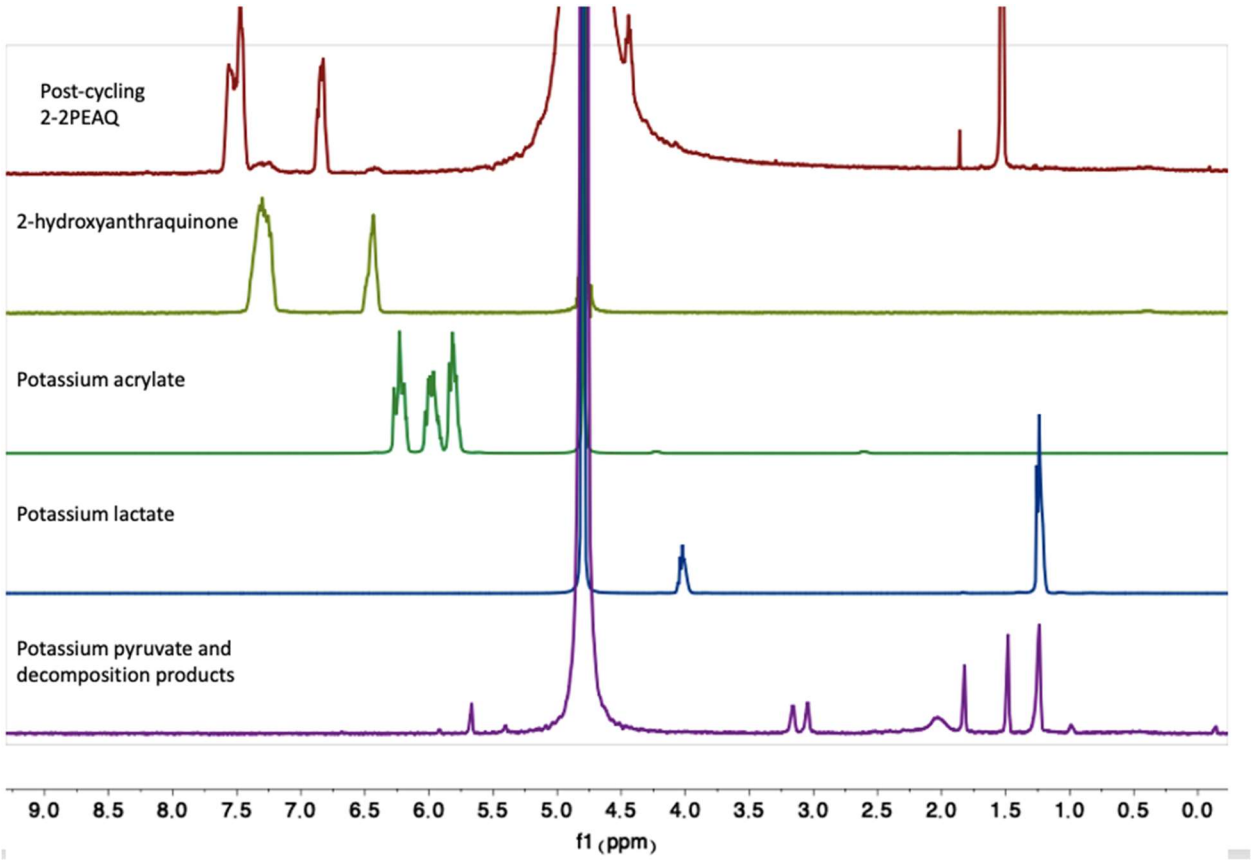

Figure 4.10: ^{1}H NMR of 2-2PEAQ after cycling in pH 14 cell (top) and comparison species. Comparison peaks not to scale.

NMR was followed up using LCMS studies. LCMS verified the presence of 2-hydroxyanthraquinone in the solution after cycling. Lactate and acrylate were not detected, however, the mass-to-charge ratio of pyruvate was detected, though the small molecule did not interact strongly enough with the column to form a discrete peak on the chromatograph. Anthrone formation or formation of anthrone dimer, a further product of the decomposition pathway shared by many anthraquinones, was not observed (Table 4.1)[70]. 2-hydroxyanthraquinone was observed in the posolyte, but no intact 2-2PEAQ was observed – indicating the side chain slows the crossover of this molecule through the membrane.

Table 4.1: LCMS results for 2-2PEAQ pH 14 cell

Compound	Negolyte Reservoir	Posolyte Reservoir	Pre-cycling 2-2PEAQ sample
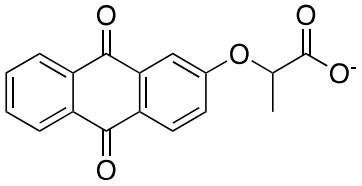	Detected	Not Detected	Detected
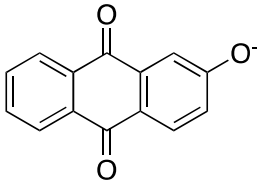	Detected	Detected at low concentrations	Detected
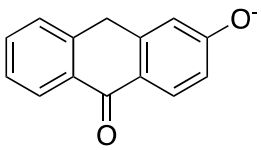	Not detected	Not detected	Not tested
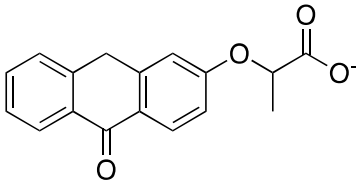	Not detected	Not Detected	Not tested
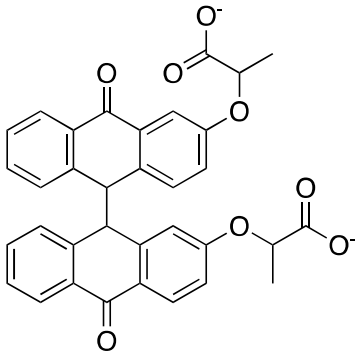	Not detected	Not detected	Not tested
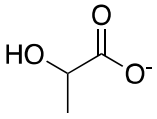	Not detected	Not tested	Detected
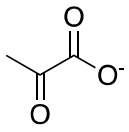	Detected	Not tested	Not tested
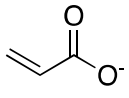	Not detected	Not tested	Detected

Table 4.1: LCMS results of the posolyte reservoir and the negolytes reservoir were prepared at 10μM in water and run by the Small Molecule Mass Spectrometry Facility at Harvard University. The pre-cycled solution was prepared at 20 μM in water. The ESI mass spectrum was recorded in negative ionization mode.

4.4 Capacity recovery of 2-2PEAQ and high concentration cell cycling

Anthraquinones have previously been reported to decompose through overreduction resulting in the formation of anthrone. Prior work has demonstrated that the original anthraquinone can be regenerated and capacity recovered by exposing this anthrone to ambient oxygen or by holding the cell at low voltages in a "deep discharge" process.[70] Because 2-2PEAQ is singly substituted, the anthraquinone core can potentially be generated from inexpensive feedstock chemicals as starting material (see Chapter 3). If this potentially low cost can be combined with an extended lifetime through capacity recovery processes, the suitability of 2-2PEAQ for large-scale batteries increases.

To test the efficacy of capacity recovery methods on 2-2PEAQ a cell was prepared and cycled as described previously, except every three days a deep discharge step was performed. The cell faded at a rate of 0.03% - 0.05% per day when actively cycling between 0.5 and 1.3 V. On days 3, 6, and 10 the cell was held at -0.05 V in a deep discharge step, resulting in some capacity being recovered, likely indicating that some anthrone formation had occurred and was reversed. Over the period of 13 days, an overall capacity fade of 0.01%/day was achieved (Figure 4.11).

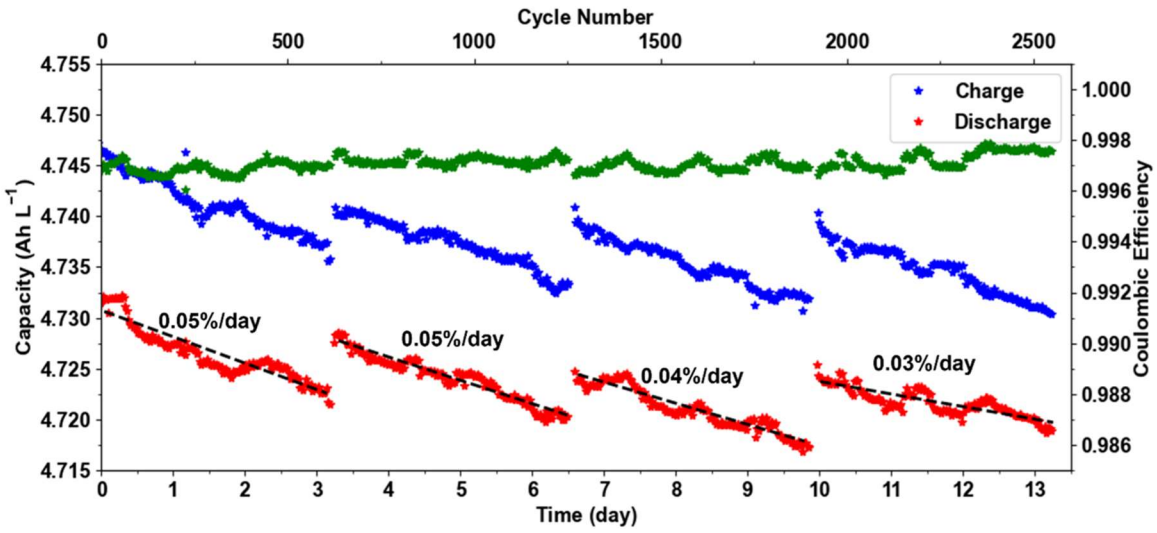

Figure 4.11: Capacity recovery cell of a 0.1 M cell 2-2PEAQ. Cell run and graph prepared by Dr. Kiana Amini.

To test the cell under more realistic conditions, a high concentration cell was prepared with 5 mL of 1.0 M of 2-2PEAQ in KOH solution at pH 14 as the negolyte and 100 mL of 0.3 M potassium ferrocyanide, 0.2 M sodium ferrocyanide, and 0.3 M of potassium ferricyanide as the posolyte. The capacity-limiting negolyte had a theoretical capacity of 964 C or 53.6 Ah/L. The membrane was Nafion 212 and the electrodes were SGL AA. The cell was cycled at 40 mA/cm^2 with potentiostatic holds at 0.5 and 1.3 V on discharge and charge respectively. Over a period of 9 days, an average fade rate of 0.03%/day was observed (Figure 4.12a). The capacity v. voltage curves for representative cycles are shown in Figure 4.12b.

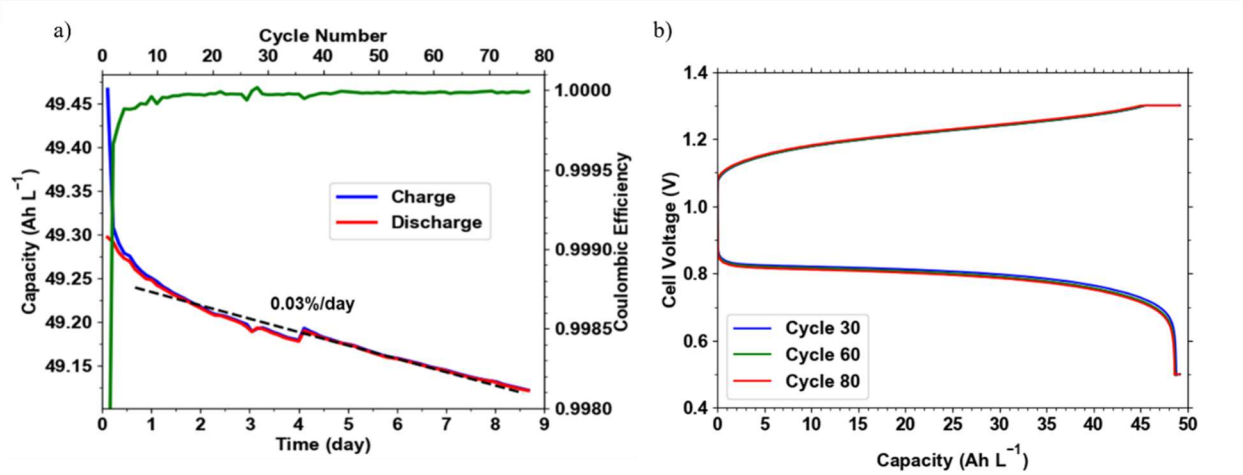

Figure 4.12: High concentration cell cycling of 2-2PEAQ. a. 2-2PEAQ capacity over the course of cell cycling. b. Charge-discharge voltage profiles of the high concentration 2-2PEAQ cell at cycles 20, 40, and 60. The cell was run and figures prepared by Dr. Kiana Amini.

4.5 Comparison of 1-2PEAQ and 2-2PEAQ

Previous studies of ether-linked anthraquinones in flow batteries have generally found that anthraquinones with ether linkages only on the carbon adjacent to the central quinone ring (the alpha carbon) experienced higher fade rates than anthraquinones with the linkage attached on carbons non-adjacent to the central ring (the beta position). Figures 4.13a and 4.13b show previously published symmetric cell runs of 1,2-DBEAQ and 1,8-DBEAQ had capacity fade rates of >0.1%/day and >10%/day compared to <0.01%/day for the solely beta-substituted 2,6-DBEAQ isomer in a symmetric cell (Synthetic information for 1,2-DBEAQ and 1,8-DBEAQ in appendix A). Similarly, the. 1,8-D2PEAQ and 1,4-D2PEAQ isomers showed fade rates of >1.1%/day and 2.4%/day respectively, depending on the cell cycling conditions, particularly the voltage cutoffs for 1,8-D2PEAQ (Figure 4.13c-d, synthetic information for 1,8-D2PEAQ and 1,4-D2PEAQ can be found in appendix A).

a.

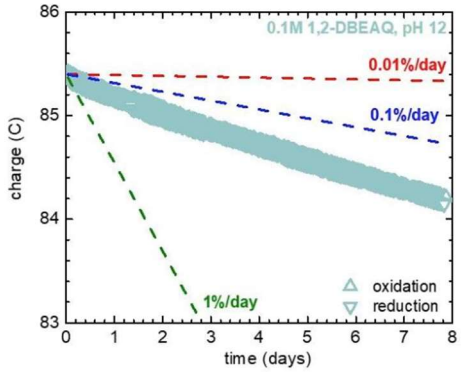

b.

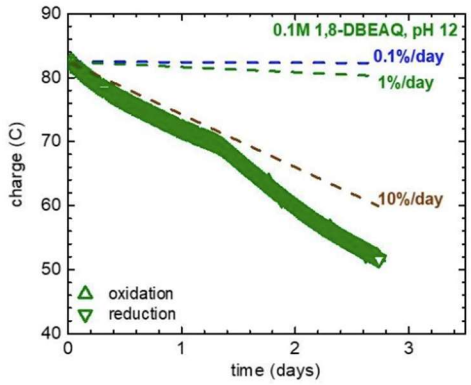

c.

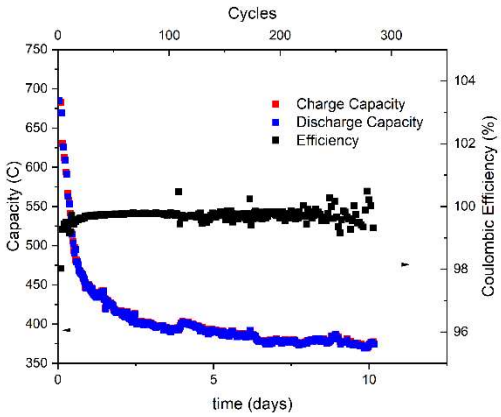

d.

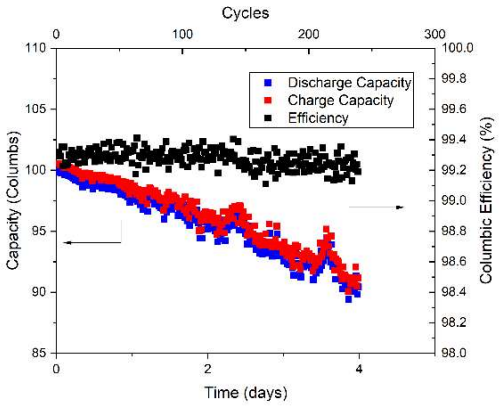

Figure 4.13: Capacity fade of ether-linked anthraquinone isomers. a. symmetric cell of 1,2-DBEAQ. Cell run by Dr. David Kwabi and image previously published in reference 29 .b. A symmetric cell of 1,8-DBEAQ. Cell run by Dr. David Kwabi and image previously published in reference 29 c. A full cell of 1,4-D2PEAQ. Cell run by Dr. Zhijiang Tang. d. A full cell of 1,8-D2PEAQ. Cell run by Dr. Zhijiang Tang.

It has not previously been possible to systematically study the differences between alpha-substituted and beta-substituted ether-linked anthraquinones in flow batteries without adding the

complexity of two separate side chains due to the limited solubility of previously reported monosubstituted anthraquinones. The highly solubilizing nature of the branched side chain, however, allows both 2-2PEAQ and its isomer 1-2PEAQ (Figure 4.14) to dissolve at >0.1M in pH 14 solution.

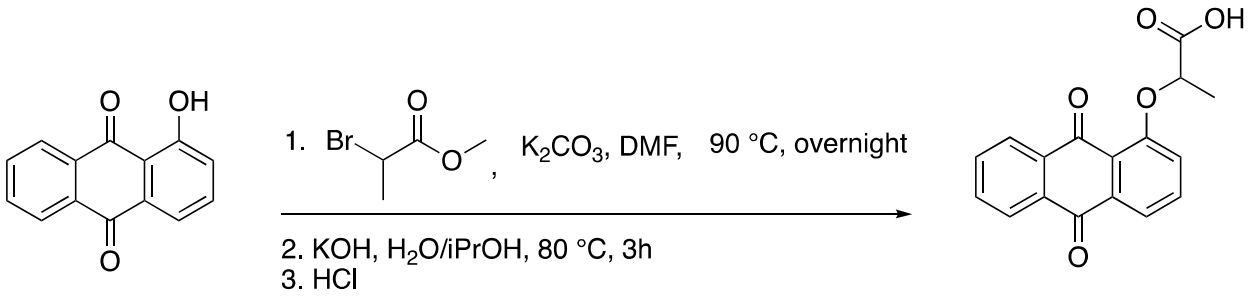

Figure 4.14: Synthesis of 1-2PEAQ. Synthesis developed in collaboration with Abdulrahman Alfaraidi.

A cyclic voltammogram of 1,2-PEAQ was obtained at a 0.1 V/s scan rate. This showed a reduction potential of -0.465 V vs. SHE and a potential total OCV of 0.96 V against a potassium ferrocyanide posolyte. The peak separation was 51 mV (Figure 4.15).

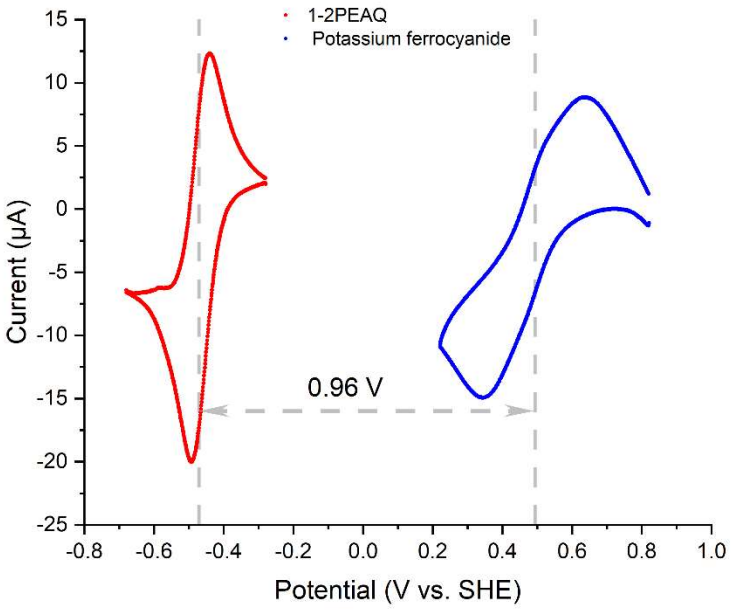

Figure 4.15: Cyclic voltammogram of 1-2PEAQ. The cyclic voltammogram of 1-2PEAQ was obtained from a solution at pH 14 containing both 1 mM 1-2PEAQ (blue) and 1 mM potassium ferrocyanide (red). The second complete cycle is shown. A background current of a pH 14 KOH solution scanned under the same conditions has been subtracted.

To study the thermal stability, 1,2-PEAQ was heated at 65 °C in an oven for 1 week in both the oxidized and the reduced form. The reduced form was then re-oxidized by agitating the solution in air and both solutions were diluted by a factor of 6 with D_2O and ^1H NMRs obtained (Figure 4.16). No new aromatic peaks appear; however, shifts are observed in the aromatic peaks. A singlet at 1.90 ppm is observed for the sample heated in the oxidized form. This singlet is likely the result of side chain loss, as discussed in the post-cycling analysis of 2-2PEAQ but is much larger than the 1.90 ppm peak observed for that molecule.

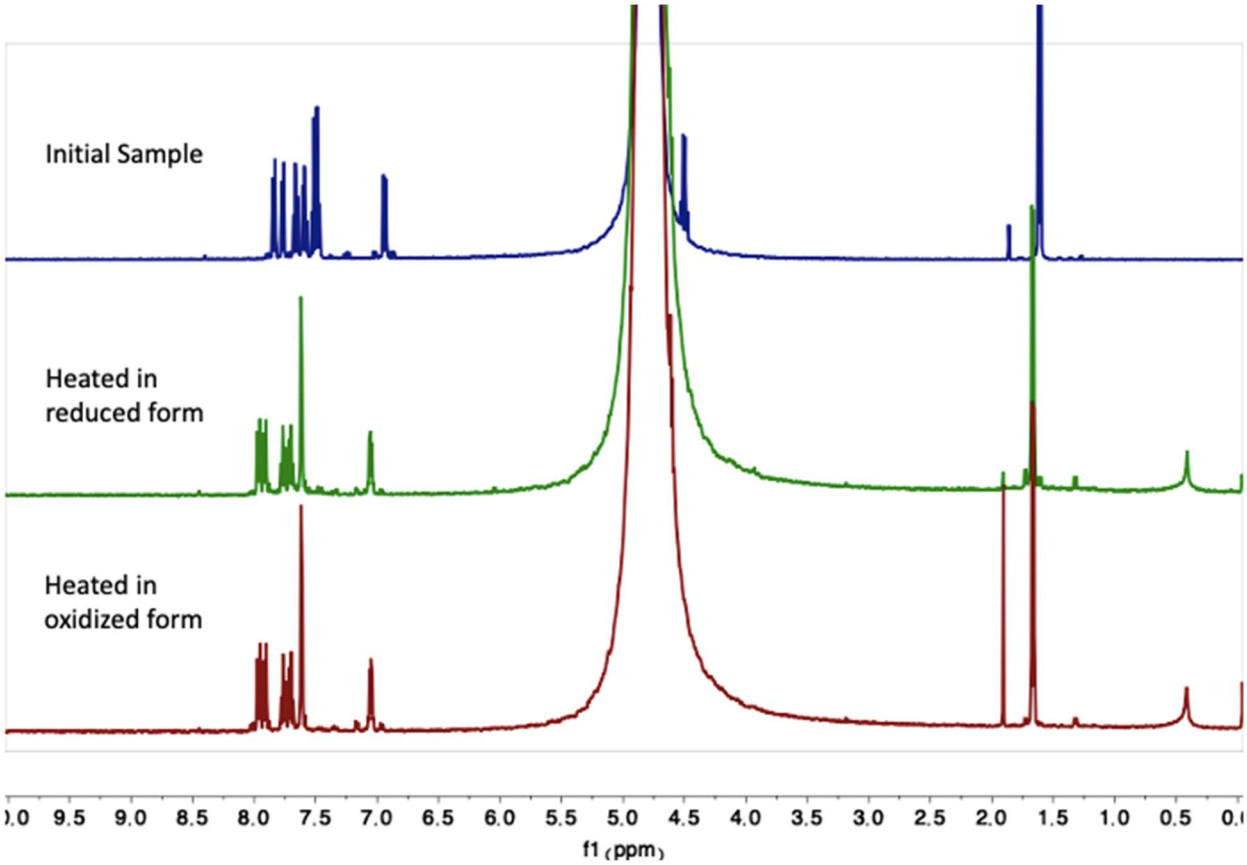

Figure 4.16: Thermal decomposition of 1-2PEAQ. Samples were obtained by mixing 100 µL of the heated sample with 500 µL of D_2O and taking ^{1}H-NMR spectra before and after heating. The sample heated in the reduced form was re-oxidized before analysis.

Cell cycling of 1,2-PEAQ was performed using 5.9 mL of 0.1 M 1,2-PEAQ in 1 M KOH as the negolyte and an excess of 50 mL of 0.1 M potassium ferrocyanide and 0.02 M of potassium ferricyanide as the posolyte. The cell was constructed using SGL AA electrodes and a Nafion 212 membrane and cycled at 40 mA/cm^2 between 0.5 and 1.3 V followed by a potentiostatic hold until the current fell to 1 mA/cm^2. This cell experienced a capacity fading rate of 0.16%/day (Figure 4.16a). Charge-discharge voltage profiles taken at cycles 50, 200, and 400

are shown in Figure 4.16b. This confirmed the hypothesis that singly alpha-substituted anthraquinone using this side chain fades faster than the beta-substituted analog.

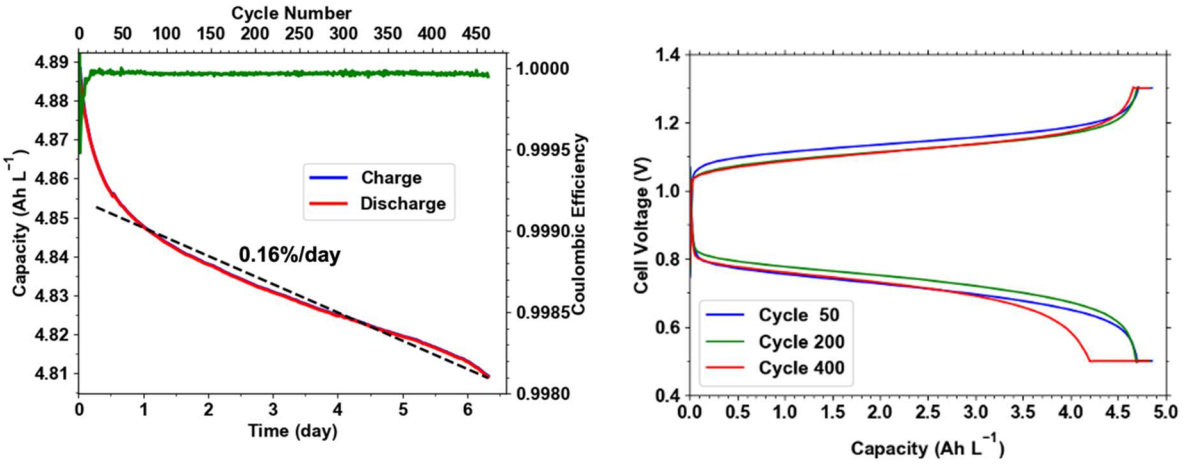

Figure 4.17: Cell cycling and capacity fade of 0.1 1-2PEAQ cell. Cell prepared and operated by Dr. Kiana Amini. Graphs prepared by Dr. Kiana Amini

NMR of the posolyte and negolyte reservoirs was used to assess crossover and decomposition after cycling was completed. ^{13}C NMR showed no unexpected peaks for either the potassium ferrocyanide reservoir or the 1-2PEAQ negolyte reservoir, although a red color was observed in the potassium ferrocyanide solution, indicating the possibility of some anthraquinone crossover (Figure 4.18a). Likewise, no peaks indicating 1-2PEAQ crossover were detected on the ^{1}H NMR of the positive electrolyte (Figure 4.18b).

a. b.

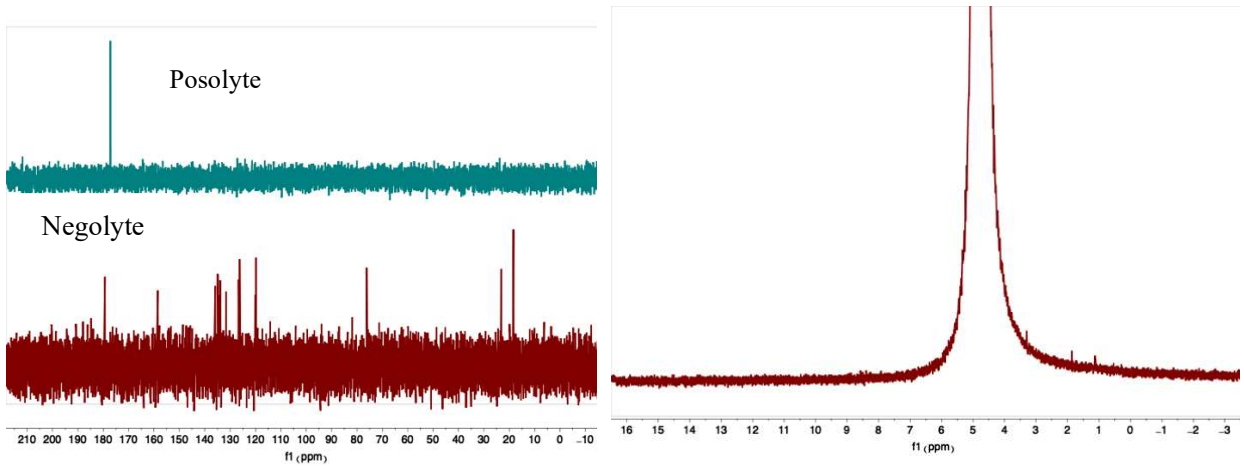

Figure 4.4: NMR crossover analysis of 1-2PEAQ cell. a. ^{13}C NMR of posolyte (blue) and negolyte (red) reservoirs. b. ^{1}H NMR of the posolyte reservoir.

Cyclic voltammograms were obtained of both reservoirs without dilution (Figure 4.19). 10 cycles from -0.78 to 1.22 V vs. SHE were completed at a scan rate of 0.1 V/s. The principal component of the negolyte reservoir is 1,2-PEAQ and the principal component of the negolyte reservoir was potassium ferro/ferricyanide. A small peak at the potential expected for 1,2-PEAQ was observed when the posolyte reservoir was scanned at only negative potentials (Figure 4.19c). No signs of crossover were otherwise observed.

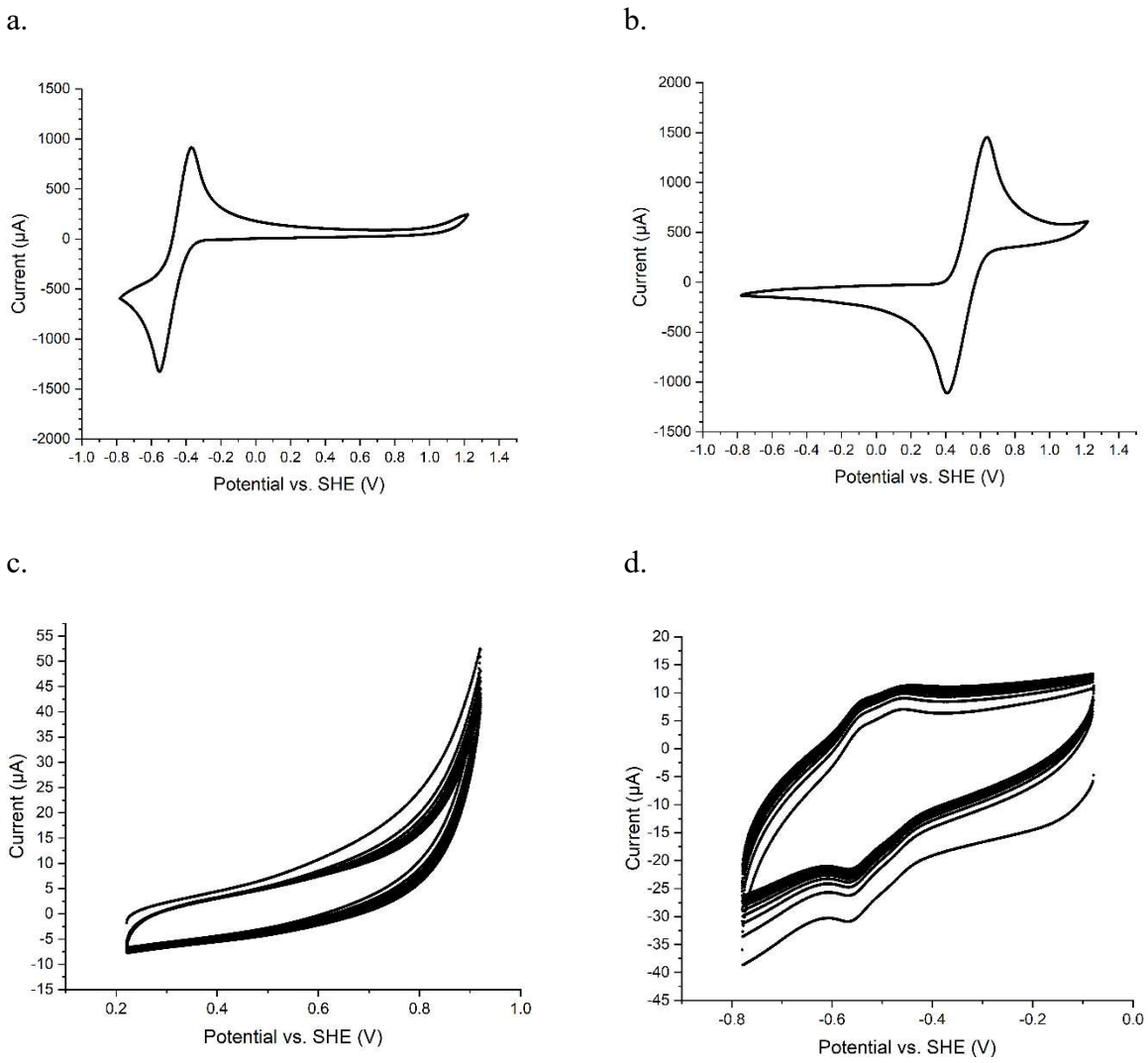

Figure 4.19: Cyclic voltammetry of 1-2PEAQ post-cycling reservoirs. a. Cyclic voltammogram of the negolyte reservoir scanned from -0.78 to 1.2 V vs. SHE. b. Cyclic voltammogram of the posolyte reservoir scanned from -0.78 to 1.2 V vs. SHE. c. Cyclic voltammogram of the negolyte reservoir scanned from 0.22 to 0.92 V vs. SHE only. d. Cyclic voltammogram of the posolyte reservoir scanned from -.78 to -0.08 V vs. SHE only.

Proton NMR of the negolyte was used to evaluate potential molecular decomposition. New singlets were observed at 1.86 ppm and 8.43 ppm and a new doublet was observed at 1.29.

Small peaks from 1-hydroxyanthraquinone also grow relative to the 1-2PEAQ aromatic peaks during the course of cell cycling. (Figure 4.20).

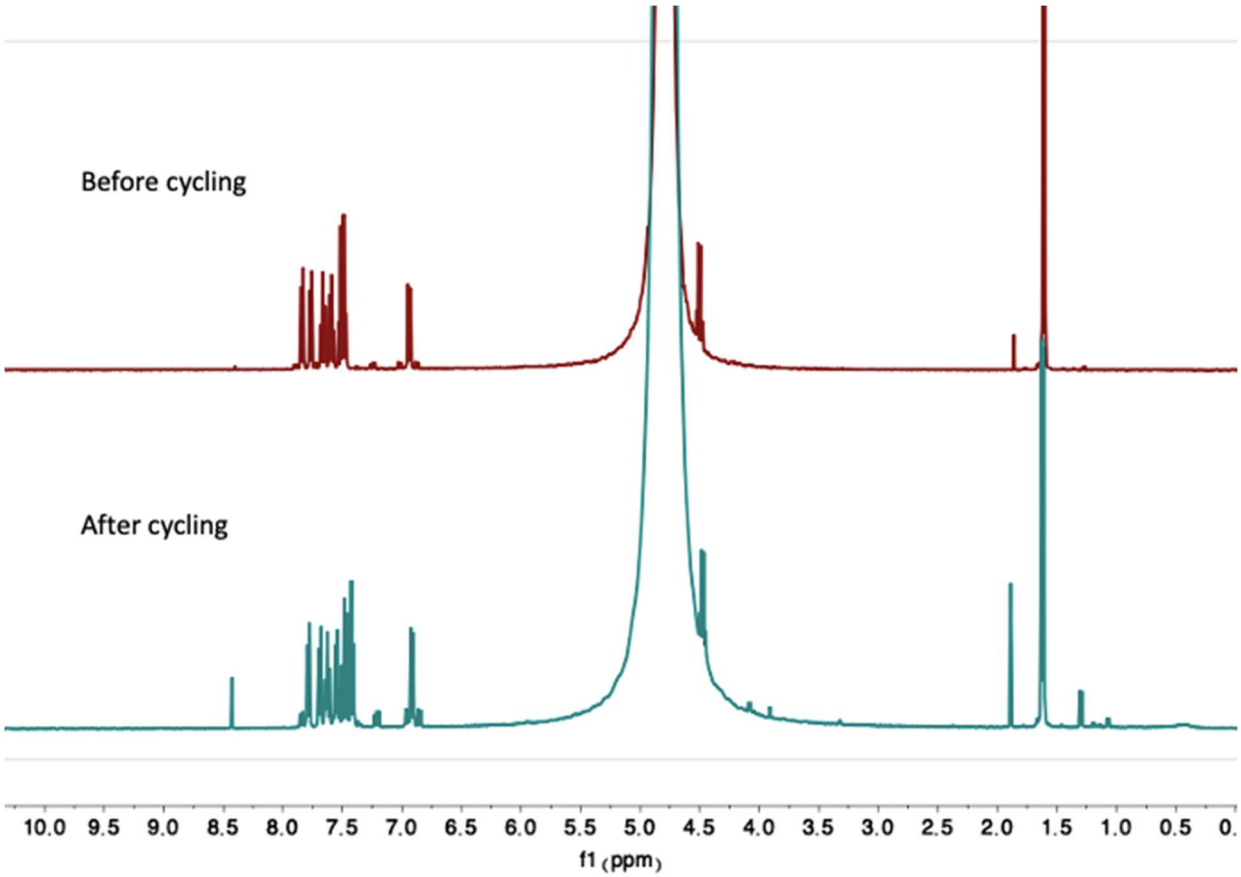

Figure 4.20: ^{1}H NMR of cycled 1-2PEAQ negolyte. New peaks are observed at 8.43 (s), 1.89 (s), and 1.29 (d).

To attempt to identify the new singlet at 1.86 the post-cycling solution was spiked with first one and then two drops of new commercial pyruvic acid. This resulted in the growth of the peak at 1.86 ppm and 1.27 ppm relative to the 1-2PEAQ peak at 1.64 ppm. The other peaks associated with pyruvic acid at pH 14 were not present in the post-cycling solution (Figure 4.21).

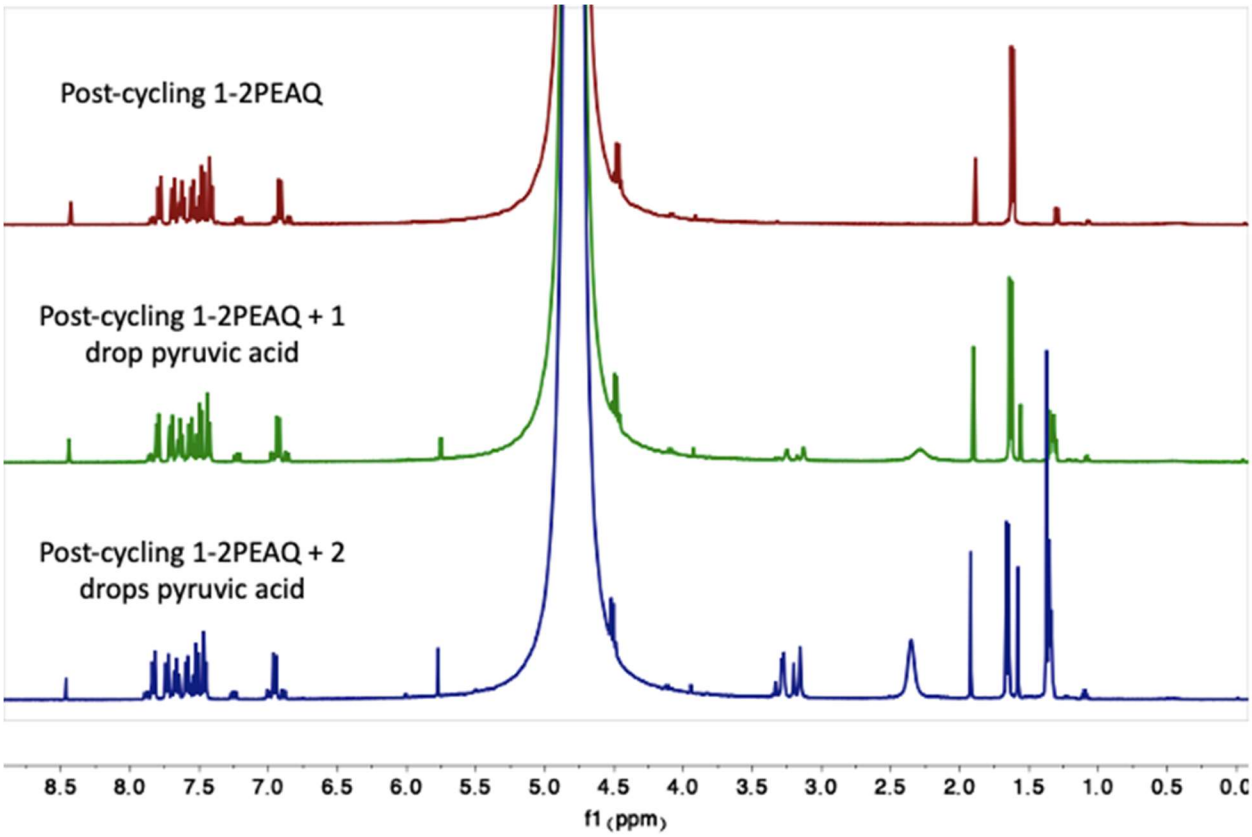

Figure 4.21: Pyruvic acid spike in post-cycling 1-2PEAQ.

LCMS analysis of 1-2PEAQ after cycling was performed by the Small Molecule Mass Spectrometry Facility at Harvard University. LCMS detected the mass-to-charge ratios of lactate, acrylate, and pyruvate as well as 1-hydroxyanthraquinone. No anthrone or anthrone dimer were detected, although this may be due to the reoxidation of anthrone derivatives to their anthraquinone precursors in oxygen. The side-chain molecules were also detected in a pre-cycled sample of 1-2PEAQ, indicating that some side-chain loss may occur in the presence of the base used in the synthesis of the molecule. No 1-2PEAQ was detected in the posolyte reservoir, indicating that the side chain prevents crossover through the Nafion 212 membrane during cycling (Table 4.2).

Table 4.2: LCMS analysis of 1-2PEAQ reservoirs after cycling

Compound	Negolyte Reservoir	Posolyte Reservoir	Pre-cycling 2-2PEAQ sample
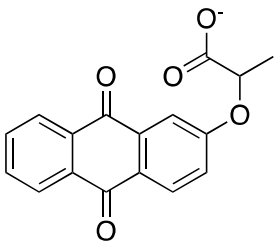	Detected	Not Detected	Detected
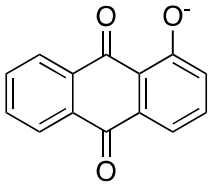	Detected	Detected at low concentrations	Detected
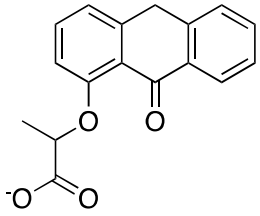	Not detected	Not detected	Not tested
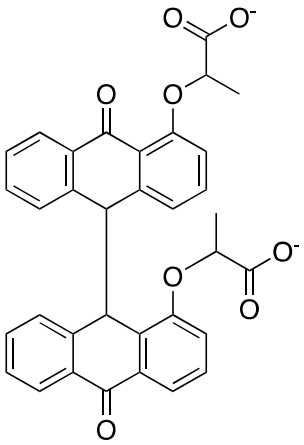	Not detected	Not detected	Not tested
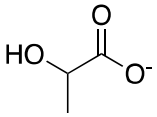	Detected	Detected	Detected
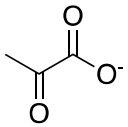	Detected	Detected	Not tested
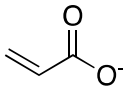	Detected	Detected	Detected

4.6 Conclusion

2-2PEAQ builds on the high stability of 2,6-D2PEAQ while retaining a high solubility of >2.0 M electrons. Decomposition seems to occur through both loss of the side chain, demonstrated by the appearance of new NMR peaks in post-cycling studies, as well as through the formation of anthrone in the cell, demonstrated by the recovery of capacity in a 2-2PEAQ cell when deep discharges are performed.

As with prior ether-linked anthraquinones, the decomposition seems more rapid on alpha-substituted isomers than beta-substituted isomers, although it remains unclear whether that is because of the relative susceptibility to anthrone formation or side chain loss. The high stability of the molecule can be further improved by using deep discharge steps to regenerate 2-2PEAQ from anthrone decomposition products, leading to an extremely low decomposition rate of 0.01%/day.

Chapter 5: Characterization of commercially available anthraquinones

Abstract:

Commercially available anthraquinones are interesting for exploration as flow battery candidates because of their easy accessibility and frequent low cost. However, commercially produced anthraquinones used as dyes are not designed for optimal redox potential, water solubility, or stability under cycling conditions. Because of this, the investigation of ultimately unpromising commercial anthraquinones can easily be unknowingly duplicated by multiple researchers. This chapter describes an initial characterization of four commercially available anthraquinones and an assessment of their feasibility for further flow battery applications.

5.2 Motivations for exploring commercially available anthraquinones

Anthraquinones have historically been used heavily by the dye industry because of their vibrant coloration and potential for lightfastness.[128] While the dye industry does not select for molecules with low reduction potentials, high solubilities, or long lifetimes under cycling conditions, some of the large number of anthraquinone derivatives tested as dyes appear as potentially promising flow battery candidates. Because of their ease of access and often low cost, the performance of commercially available anthraquinones that have not been synthetically modified is regularly published in the aqueous redox flow battery literature.

However, because molecules designed for use as dyes often don't ultimately demonstrate promising behavior in batteries upon further investigation, the easily accessible nature of these molecules can result in multiple researchers running preliminary tests on the same molecules due to a lack of knowledge that a molecule has previously been investigated and found wanting. In order to avoid this duplication of effort in the future, this chapter details the preliminary

investigation of several anthraquinone dyes for use in flow batteries, their shortcomings, and potential avenues of exploration in the future.

5.3 Carminic Acid

Carminic acid is a red dye commonly produced as the aluminum lake pigment derived from the cochineal insect that has historically been used to give fabrics, foods, and paints a red color.[129] Its structure is shown in Figure 5.1. This structure initially seemed promising because of the presence of both a carboxylic acid group and a monosaccharide that could aid in solubilizing the molecule in an aqueous solution. While it's common to find anthraquinones bonded to sugars in nature, this has not previously been reported in an anthraquinone used for cell cycling despite the potential for achieving high solubilities at a range of pH values.

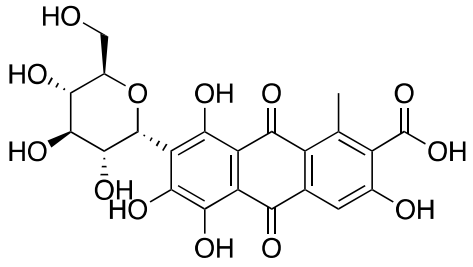

Figure 5.1: Chemical structure of carminic acid

An initial thermal decomposition study was performed of carminic acid in a pH 14 solution of KOH at 65 °C for 8 days. The H^1 NMR of carminic acid before and after heating was obtained after diluting the sample with 500 µL of deuterium oxide. The resulting NMRs are shown in Figure 5.2. No changes in the peak in the aromatic region are seen. The aliphatic region

is largely stable, although new peaks are observed at 4.06 (quadruplet) and 1.26 ppm (doublet). The source of these peaks has not been identified, but their integration is 0.65 and 1.15 relative to the aromatic peak respectively

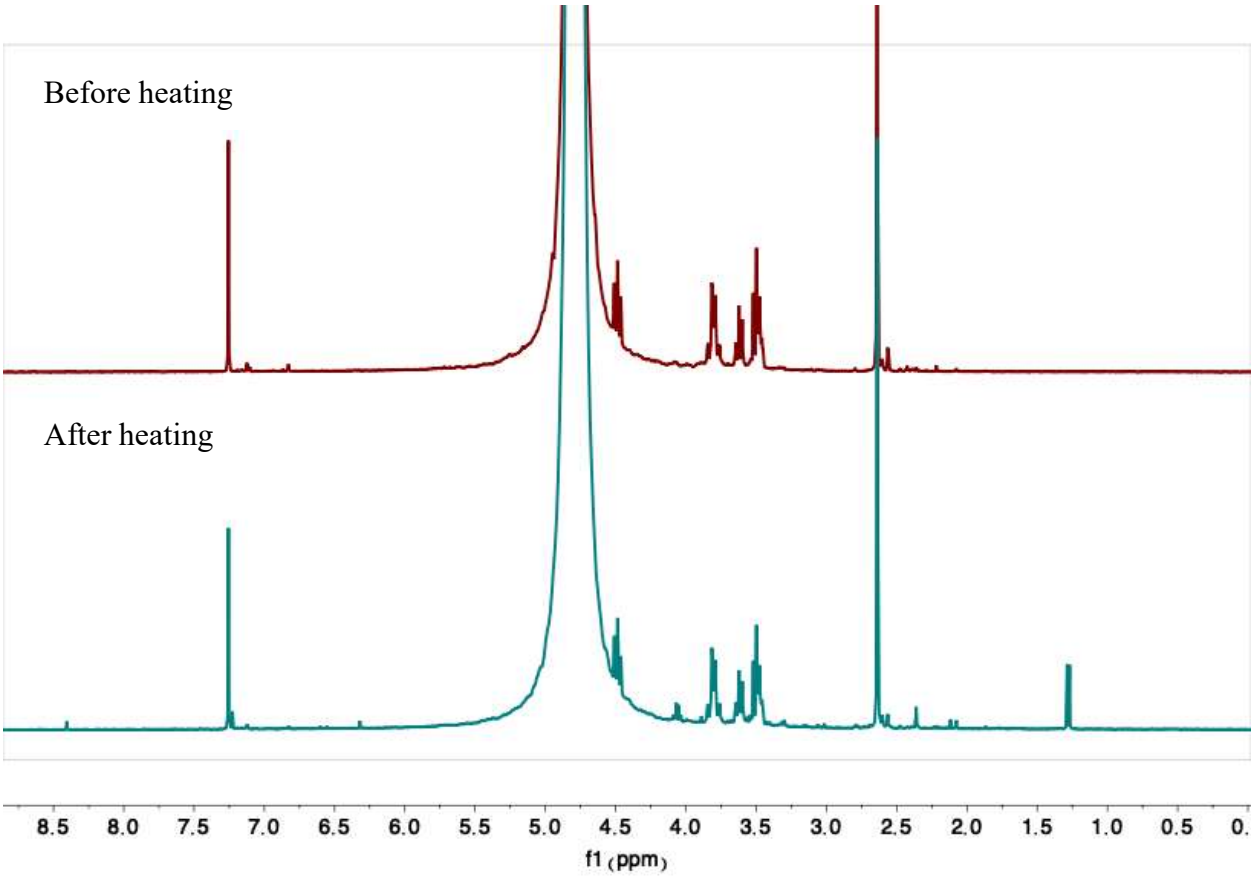

Figure 5.2: Thermal decomposition of carminic acid. ^{1}H NMR of 0.1 M carminic acid before (red) and after (blue) being held at 65 ºC for eight days in the oxidized form.

To test the electrochemical behavior of carminic acid, cyclic voltammetry was performed at both pH 0 in 1 M HCl and pH 14 in 1 M KOH using 1 mM of carminic acid and a scan rate of 0.1 V/s. No clear peaks were identified at pH 14, which is consistent with previous work showing that carminic acid shows increasingly less reversible redox activity at high pH (Figure 5.3)[130]. It is possible this is caused by the high number of negative charges accumulated on the molecule from the 4 phenolic groups attached to the ring and the carboxylate at high pH limiting

the reduction of the molecule, which would add further negative charge. The acidic CV showed a small peak at -95 mV v. SHE with a peak separation of 80 mV.

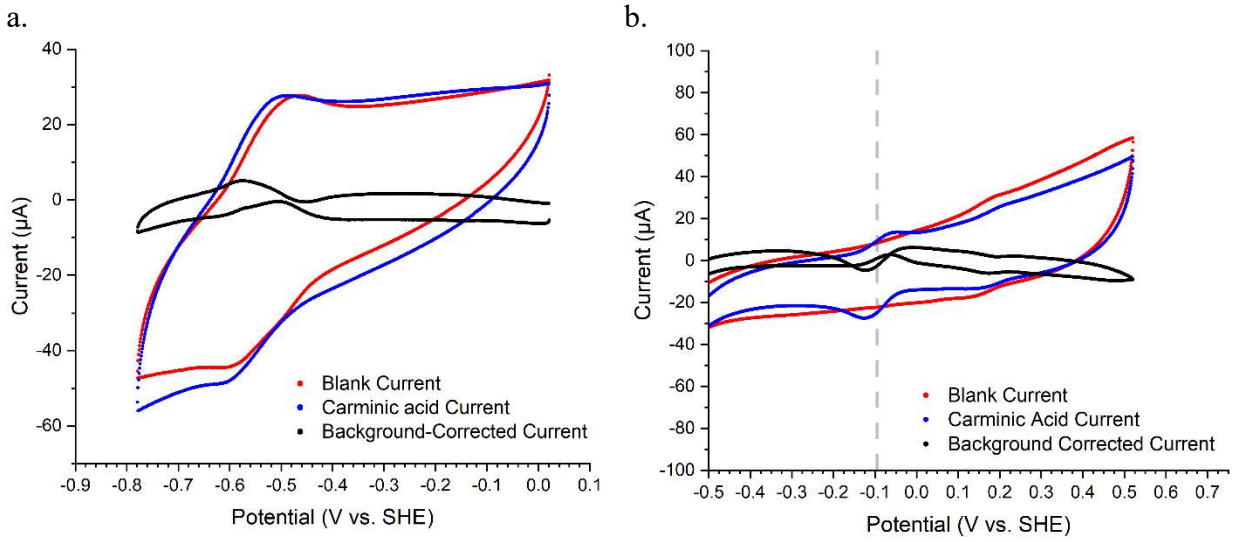

Figure 5.3: Cyclic voltammetry of carminic acid. a. CV of 1 mM carminic acid in pH 14 solution. Both the pH 14 blank solution containing only a 1 M KOH solution and the pH 14 solution containing 1 mM carminic acid was degassed with nitrogen prior to CV. b. CV of carminic acid at pH 0. Both the 1 M HCl solution blank and the pH 0 solution of carminic acid were degassed with nitrogen. The grey dotted line indicates the center of the peak. Both CVs used an Ag/AgCl reference electrode, glassy carbon working electrode, and graphite counter electrode.

While the cyclic voltammetry of carminic acid showed minimal reversible redox chemistry, molecules with poor redox kinetics on glassy carbon can demonstrate improved redox kinetics on the porous carbon electrodes used in flow batteries.[131] Because of the good thermal stability observed, carminic acid was tested at 0.1 M (5.5 mL) against potassium ferrocyanide (40 mL) at pH 14. A Nafion 212 membrane was used with SGL 39AA carbon felt electrodes.

88% of the total theoretical capacity was accessed. However, the capacity retention was poor, with the 1.2%/day being lost (Figure 5.4). Further studies of the decomposition pathway for this cell should be undertaken before further cell testing or investigation as a flow battery candidate is merited.

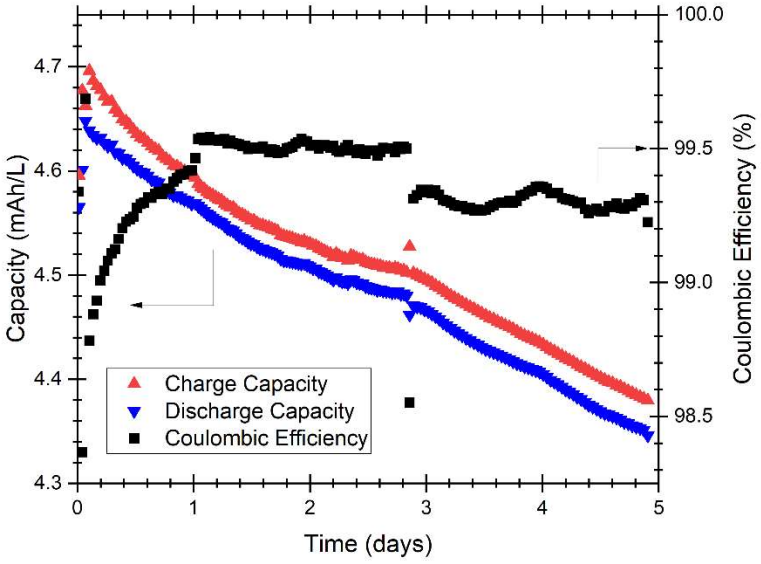

Figure 5.4: Cell testing of carminic acid. A 0.1 M Carminic acid cell at pH 14 was prepared using 5.5 mL of 0.1 M carminic acid in KOH at pH 14 against 40 mL of potassium ferrocyanide posolyte. A Nafion 212 membrane was used with SGL carbon fiber electrodes. A current cutoff of 20 mA/cm^2 was used from the start of cycling until 1 day (Cycle 0 to 31) then increased to 40 mA/cm^2 from day 1 to day 2.9 (Cycle 31 to 104). The final current density was 30 mA/cm^2 from day 2.9 until the end of cycling (Cycle 104 to 168). Cell prepared and run by Abdulrahman Alfaraidi.

5.4 Laccaic Acid

Laccaic Acid is a group of compounds originally derived from the resin produced by lac insects (Figure 5.5) and is sold as Natural Red 25.[132, 133] The laccaic acids have been used as fabric dyes.[134, 135] Lacaaic Acid consists of a variety of anthraquinones. The four most abundant are shown in Figure 5.5. These dyes were studied for stability and electrochemical properties without purification of the commercial mixture obtained from TCI.

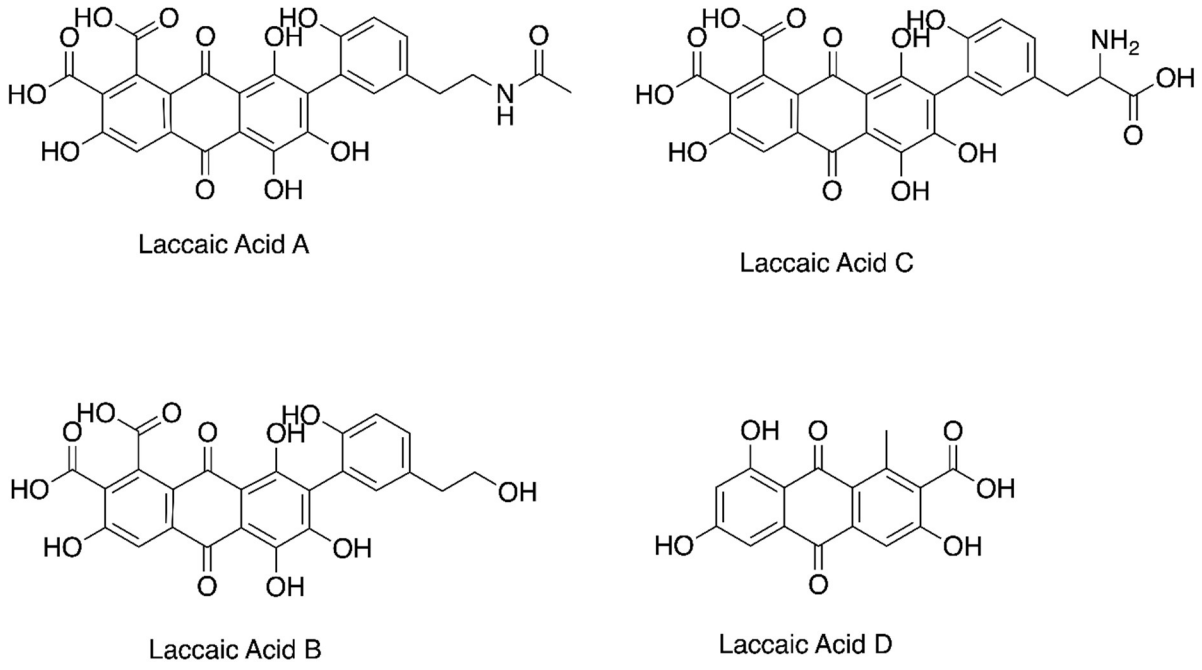

Figure 5.5: Chemical structure of Laccaic Acid A-D.

Thermal decomposition studies of laccaic acid were performed at 0.1 M in pH 14 solution at 65 ^{o}C for one week in the oxidized form (Figure 5.6). ^{1}H NMR was used before and after heating to detect the formation of new compounds. While a substantial amount of the original compound remained, several new peaks appeared, including in the aromatic region. New

peaks were observed at 7.20 (s), 7.16 (s), 7.12 (s), and 7.08 (m) ppm, as well as multiple overlapping peaks in the range of 6.72-6.82 ppm and 6.45-6.60 ppm. Additionally, new aliphatic peaks were observed between 3.01 and 3.11, 2.33 (m), and 2.11 ppm. This may indicate these molecules are prone to significant levels of thermal decomposition which make them poor flow battery candidates.

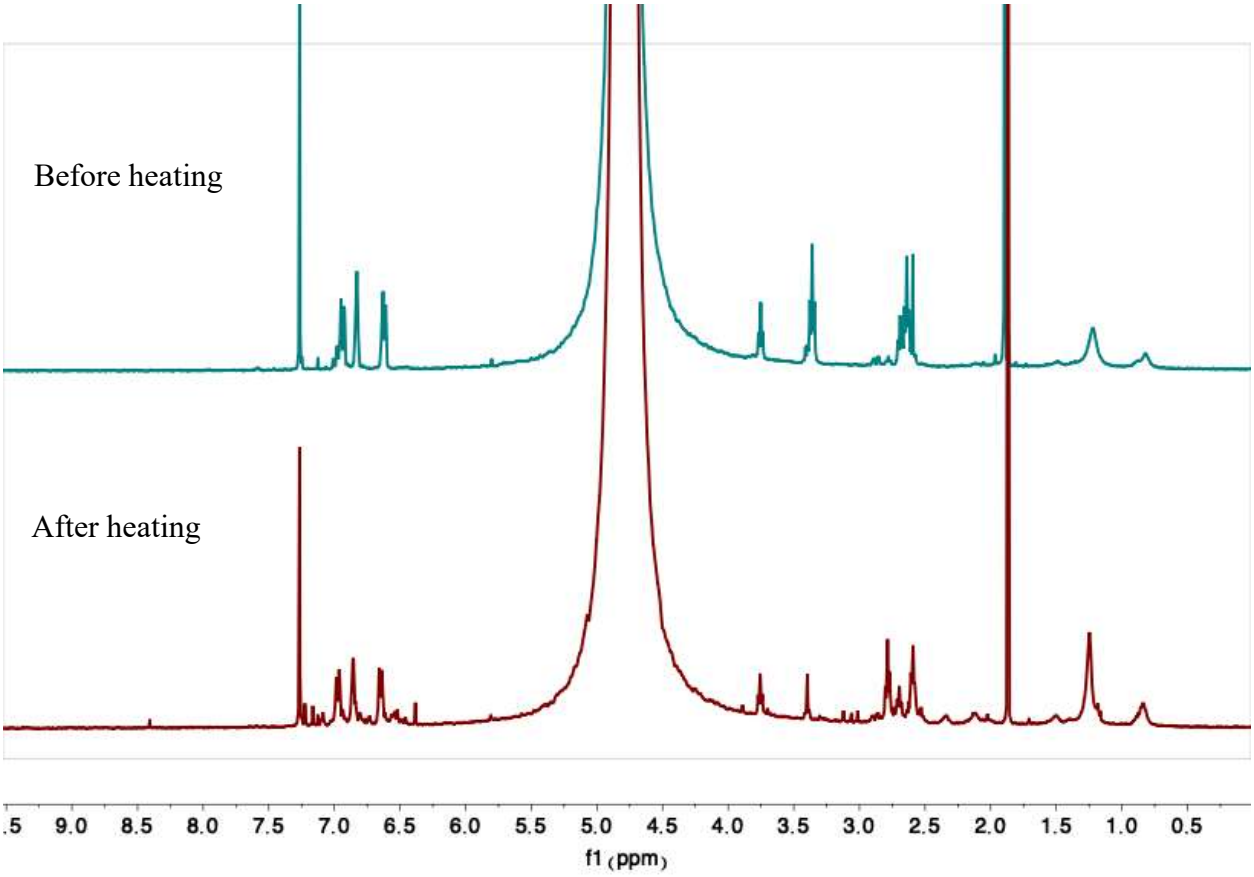

Figure 5.6: Thermal decomposition study of Laccaic Acid. ^{1}H-NMR was obtained before and after heating 0.1 M Laccaic Acid in pH 14 KOH solution.

The cyclic voltammogram of Laccaic Acid. was obtained on a glassy carbon electrode against a silver/silver chloride electrode in pH 14 KOH solution after degassing with nitrogen. No significant differences were seen between the sample containing 1 mM Laccaic acid D and

the blank containing only 1 M KOH. Because of the combination of likely thermal decomposition and poor electrochemical kinetics, Laccaic Acid was not carried forward to cell testing.

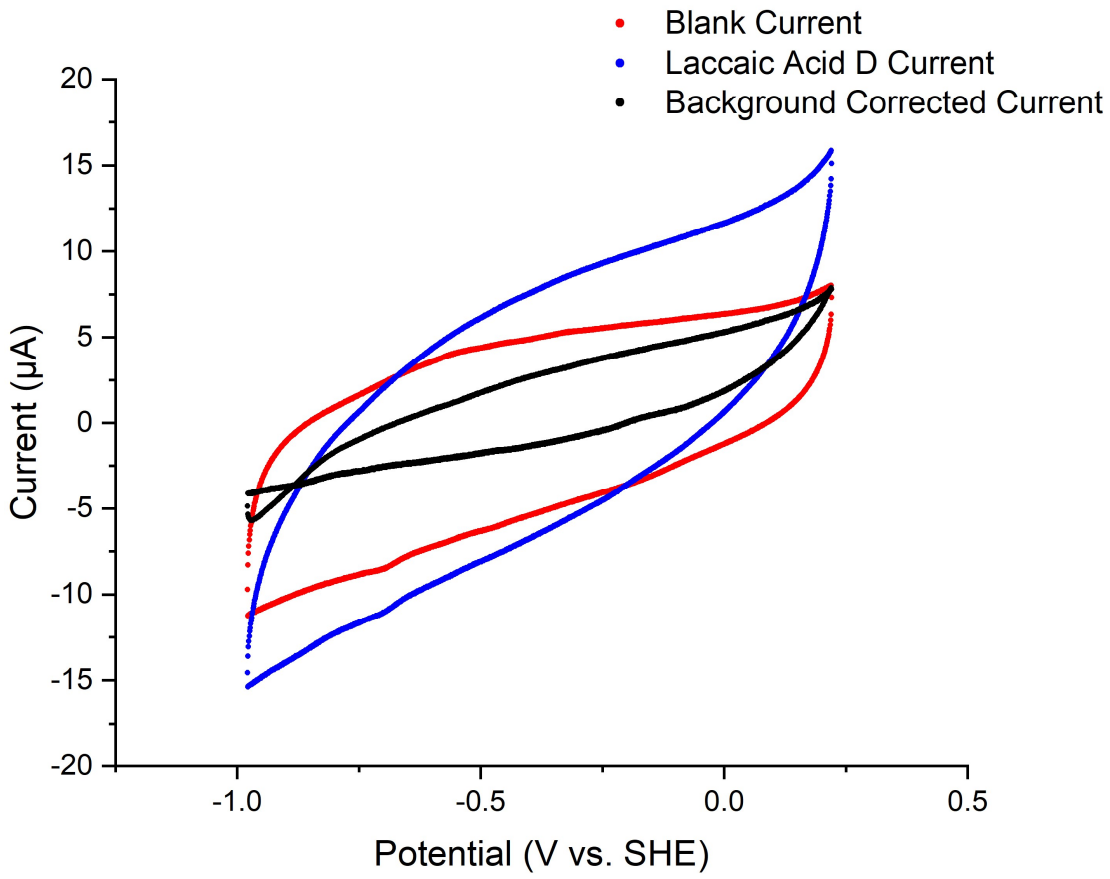

Figure 5.7: Cyclic voltammogram of 1 mM Laccaic acid at pH 14 in KOH solution compared to a 1 M KOH blank.

5.5 Alizarin Blue Black B

Alizarin Blue Black B is an anthraquinone linked to two sulfonated aromatic rings through nitrogen atoms (Figure 5.8). While the addition of two aromatic rings would tend to make a structure too insoluble for preliminary stability investigations or cell cycling, the

presence of two sulfonate groups and a phenolic oxygen suggested potentially acceptable solubility. On preparing a 0.1 M pH 14 solution for thermal decomposition studies, however, some precipitate was observed, indicating a solubility of <0.1 M at pH 14.

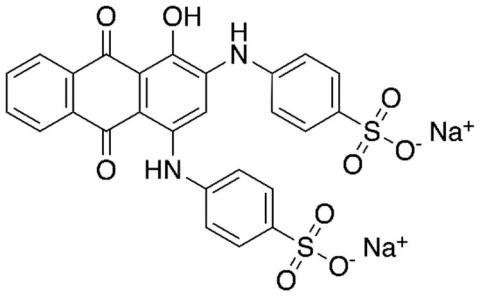

Figure 5.8: Chemical structure of Alizarin Blue Black B.

Thermal decomposition studies were still carried out at a saturated concentration. A sample was stored at 65 ºC for 8 days in the oxidized form. The commercial sample has significant peak overlap and broadening in the aromatic region, but two large doublets are seen to form at 7.54 and 6.82 after heating (Figure 5.9).

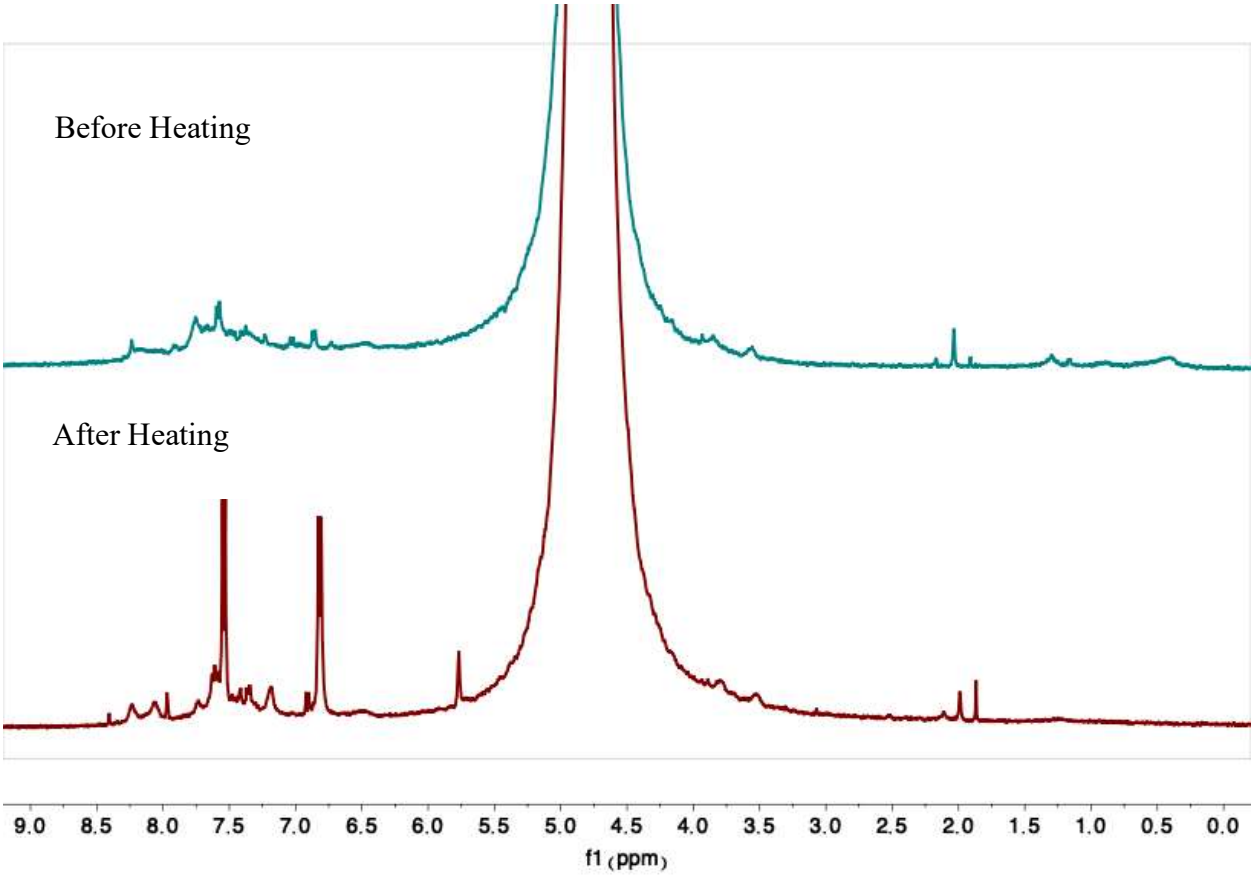

Figure 5.9: ^{1}H NMR of Alizarin Blue Black B before and after heating,

Because sulfonate groups can be solubilizing in both acidic and basic conditions, cyclic voltammetry of Alizarin Blue Black B was performed at both pH 0 and pH 14. 1 mM Alizarin Blue Black B showed an oxidation peak at -544 mV vs. SHE and two reduction peaks at -541 mV vs. SHE and -694 mV vs. SHE at pH 14 (Figure 15.10a). No electrochemical behavior was observed at pH 0 (Figure 5.10b).

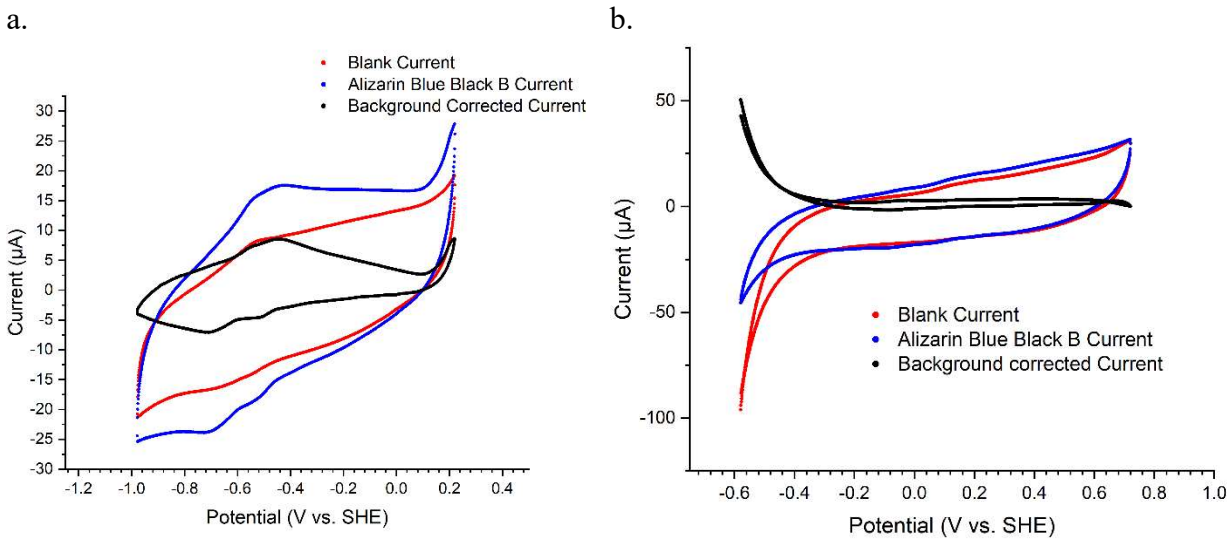

Figure 5.10: Cyclic voltammetry of Alizarin Blue Black B. a. In pH 14 KOH solution. b. Scan of Alizarin Blue Black B at pH 0.

Due to the poor aqueous solubility of the molecule as well as poor initial stability, cell testing was not done on Alizarin Blue Black B and this molecule does not appear to be a strong candidate for future flow battery research.

5.6 Acid Blue 25

Acid Blue 25 (Figure 5.11) is an anthraquinone dye that was interesting for potential flow battery applications because of its solubilizing sulfonate functionalizing group and two amine groups which would be expected to lower reduction potential by donating electron density into the anthraquinone core. However, this molecule demonstrated extremely low solubility in both acidic and basic aqueous solutions and was excluded from further analysis.

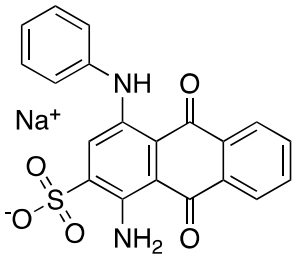

Figure 5.11: Chemical Structure of Acid Blue 25.

5.7 Conclusion

Flow battery research to date has identified a number of promising core structures that show reliable redox activity and potential stability. Commercially available compounds are particularly interesting, particularly if they are already produced at large scales, because of their easy accessibility, lack of synthetic requirements, and potential low costs.

To minimize time and resources spent on studying ultimately poorly-performing molecules, it is advisable to first do tests that require less time and material. Thermal decomposition studies, determining whether an acceptable solubility is obtainable, and cyclic voltammetry for an initial sense of electrochemical behavior are reasonable initial tests.

The molecules presented in this chapter do not seem initially promising for further study in flow batteries. If further study of these molecules is attempted, it should attempt to understand the causes of molecular decomposition and determine whether they affect battery performance and whether that effect can be ameliorated. In their current state, further use of these four molecules in battery testing is unlikely to result in strong battery performance.

Appendix 1: Synthetic Procedures and NMRs

2,6-D2PEAQ (2,2'-((9,10-dioxo-9,10-dihydroanthracene-2,6- diyl)bis(oxy))dipropionic acid)

10 g of 2,6-dihydroxyanthraquinone (41.6 mmol) was mixed with 15 g of potassium carbonate (108 mmol, 2.6 eq), 15 mL of methyl 2-bromopropionate (22.45 g, 134.4 mmol, 3.23 eq), and 30 mL of dimethylformamide and stirred at 80 ºC for 1 hour. This resulted in the formation of a sandy yellow precipitate. 20 mL of water was added and used to wash the flask followed by vacuum filtration.

Without further purification, the solid was suspended in a solution containing 150 mL of 2-propanol and 150 mL of water along with 15 g of potassium hydroxide (267 mmol. 6.43 eq). This solution was stirred at 80 ºC for 3 hours followed by the addition of 1.5 M hydrochloric acid until a yellow precipitate was seen to form. This was then vacuum filtered to give a yellow solid. 9.15 g yield (57%). ^{1}H NMR peaks: 8.15 (d, 2H), 7.50 (s, 2H), 7.38 (d, 2H), 5.17 (t, 1H), 1.58 (s, 3H). Unintegrated peaks are water and DMSO-d_5.

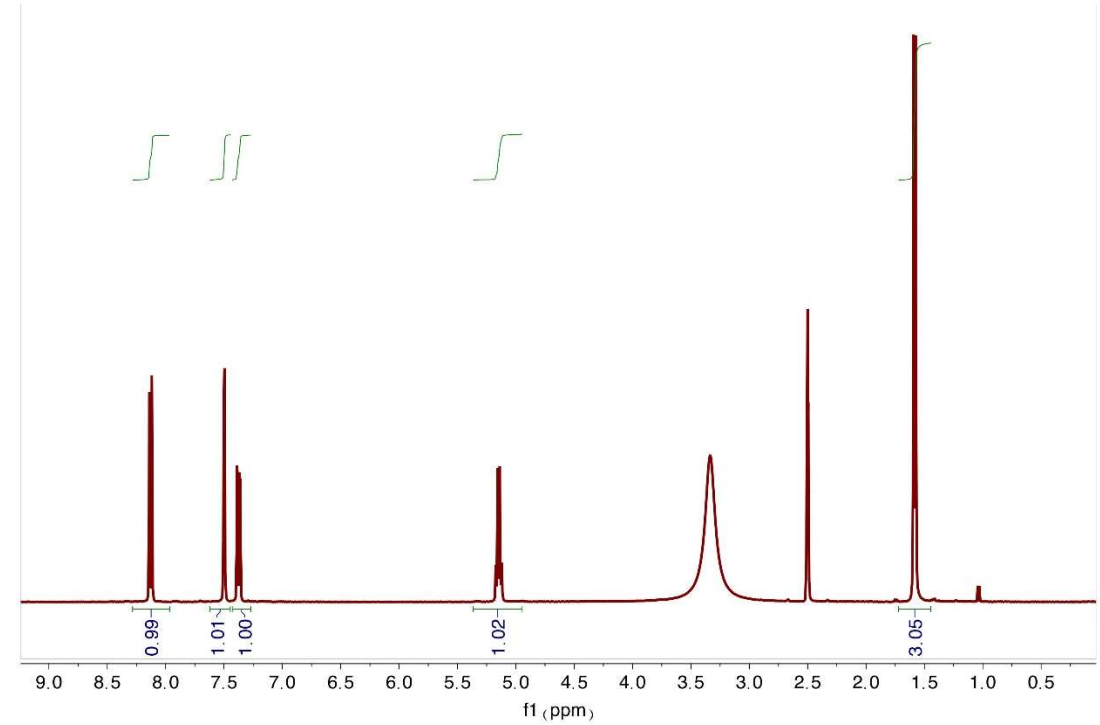

Figure A.1: ^{1}H NMR of 2,6-D2PEAQ in d6-DMSO

2,6-DEEAQ (2,2'-((9,10-dioxo-9,10-dihydroanthracene-2,6-diyl)bis(oxy))diacetic acid)

1 g (4.17 mmol) of 2,6-dihydroxyanthraquinone was mixed with 4 mL of dimethylformamide, 0.98 mL of methyl bromoacetate (1.58 g, 10.4 mmol, 2.49 eq), and 1.43 g potassium carbonate (10.3 mmol, 2.48 eq) was stirred at 85 °C overnight, resulting in the precipitation of a brown solid. 5 mL of water we added, rinsing out the sides of the vial followed by vacuum filtration.

Without further purification, the reaction product (about 2.63 g of wet solid) was suspended in a mixture of 15 mL 2-propanol, 15 mL water, and 3.0 g potassium hydroxide (53.6 mmol, 12.8 eq) and stirred at 85 °C overnight. The reaction was then cooled to room temperature followed by the addition of 50 mL of acetic acid, resulting in the formation of a sandy yellow precipitate that was

then vacuum filtered to give 1.49 g of yellow powder (^{1}H NMR peaks: 7.97 (d, 2H), 7.37 (s, 2H), 7.22 (d, 2H) 4.44. Integrated peaks belong to d5-DMSO-d_5, water, and acetic acid residues.

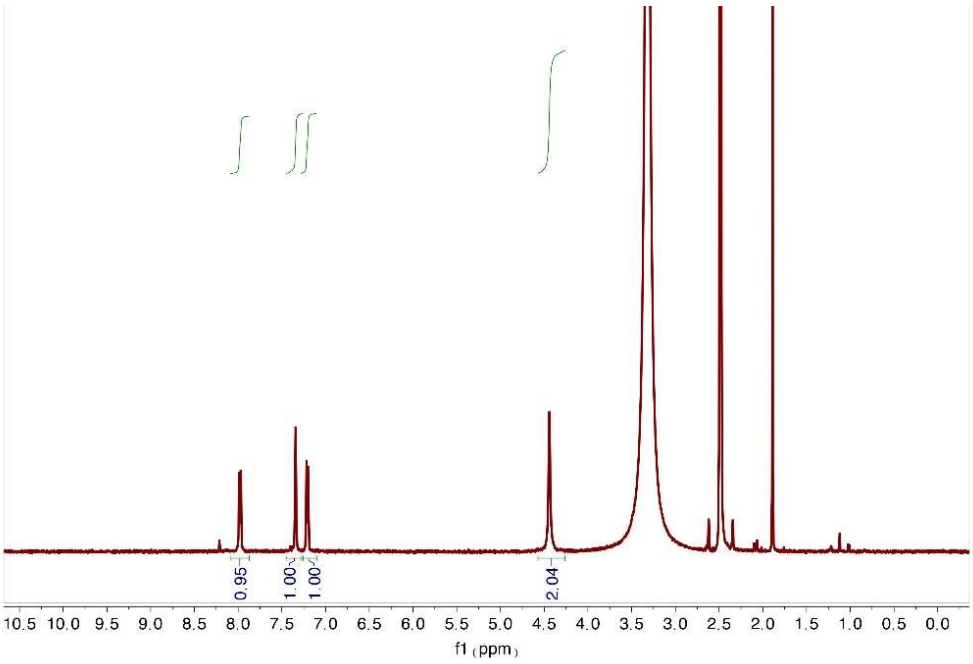

Figure A.2: 2,6-DEEAQ ^{1}H NMR in d6-DMSO

2-BEAQ (4-((9,10-dioxo-9,10-dihydroanthracen-2-yl)oxy)butanoic acid)

1gram of 2,6-dihydroxyanthraquinone (4.45mmoles) was mixed with1.5 g potassium carbonate (10.9mmol, 2.45eq) in 4mL of anhydrous dimethylformamide.1.5 mL of ethyl 2-bromopropionate (2.08g, 11.5mmol, 2.44eq). The mixture was stirred at 85 ºC for 80 minutes during which time a sandy solid precipitated out. 5 mL of water was added to the solution followed by vacuum filtration. The solid was added without purification to a flask containing 4.5 g potassium hydroxide (80.3 mmol18eq), 4 5 mL of water, and 45 mL of 2-propanol and stirred

at 85 ºC for three hours, resulting in a dark solution. Glacial acetic acid was then added until the solution formed a green precipitate which was vacuum filtered. 0.83 g of a yellow-green solid was obtained (63% yield). H^1 NMR: 8.19 (3H, m), 7.92 (2H, quint), (7.60, 1H, d), 7.45 (1H, dd), 4.24 (2H, t), 2.24 (2H, t), 2.01 (2H, quint). Unintegrated peaks belong to DMSO-d5 and water.

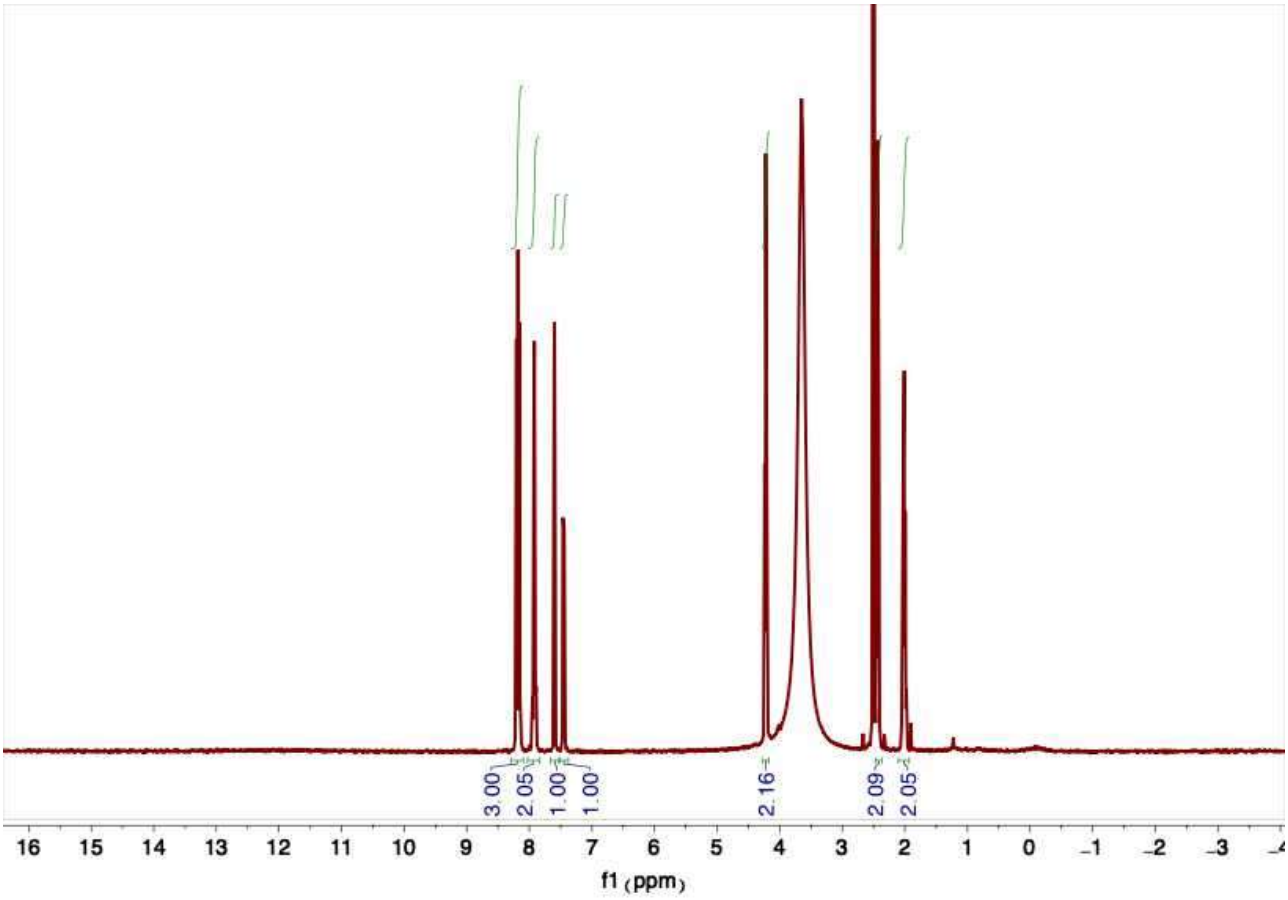

Figure A.3: ^{1}H NMR of 2-BEAQ in d6-DMSO

2-2PEAQ (2-((9,10-dioxo-9,10-dihydroanthracen-2-yl)oxy)propanoic acid)

5 grams of 2-hydroxyanthraquinone (22.3 mmol) was added to a 100 mL pear-bottomed flask. 15 mL of ethyl 2-bromopropionate (116 mmol, 5.2 eq) and 7.5 g 0f potassium carbonate (54 mmol, 2.4 eq). This solution was stored at 80 ºC for 3 hours and then vacuum filtered to give the ester.

Without further purification, the ester was suspended in 75 mL of water and 75 mL of isopropanol with 7.5 g of potassium hydroxide (13.3 mmol 1.6 eq). This solution was stirred at 80 ºC for three hours before being precipitated out using 1 M HCl as a green solid. Yield: 2.4g (36.7%). H^1 NMR: 8.19 (3H, m), 7.92 (2H, m), 7.53 (1H d), 7.42 (1H, dd), 5.18 (1H, q), 1.59 (3H, d). Unlabeled peaks are attributed to water and d^5-DMSO.

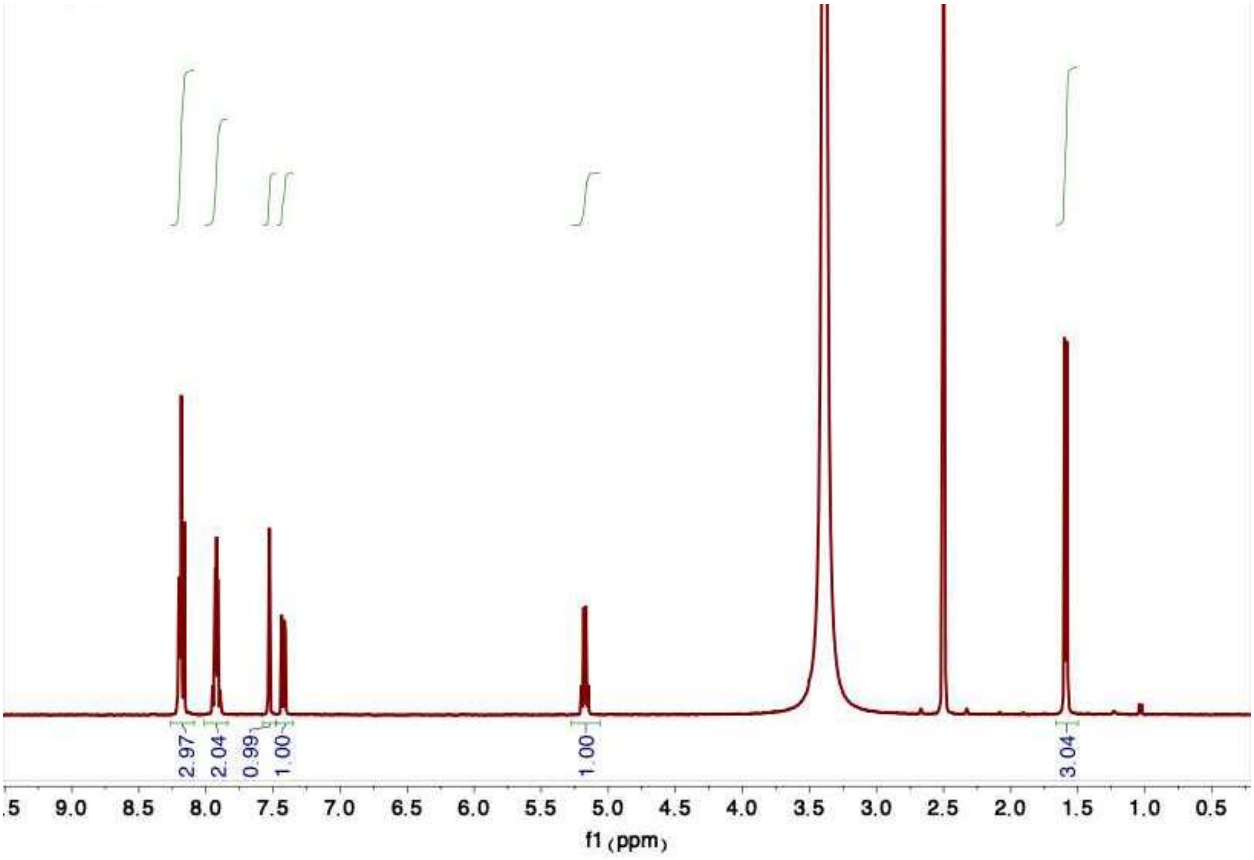

Figure A.4: ^{1}H NMR of 2-2PEAQ in d6-DMSO

1-2PEAQ (2-((9,10-dioxo-9,10-dihydroanthracen-1- yl)oxy)propanoic acid)

2 grams of 1-hydroxyanthraquinone (8.09 mmol) were mixed with 6 mL of ethyl 2-bromopropionate (46.2 mmol, 5.7 eq) and 3 g potassium carbonate (was heated at 90 ºC overnight followed by the addition of water to precipitate out the ester. This was followed without further purification by hydrolysis with 5 g KOH (89.3 mmol, 11.03 eq) in 30 mL of each water and isopropanol. This stirred for 3 hours at 80 ºC followed by precipitation with 1 M HCl to give a sandy orange solid. The yield was 2g (75.8%). H^1 NMR: 8.14 (2H, td), 7.86 (4H m), 7.39 (1H dd), 5.09 (1H, q), 1.63 (3H, d). Unintegrated peaks are attributed to water and d^5-DMSO

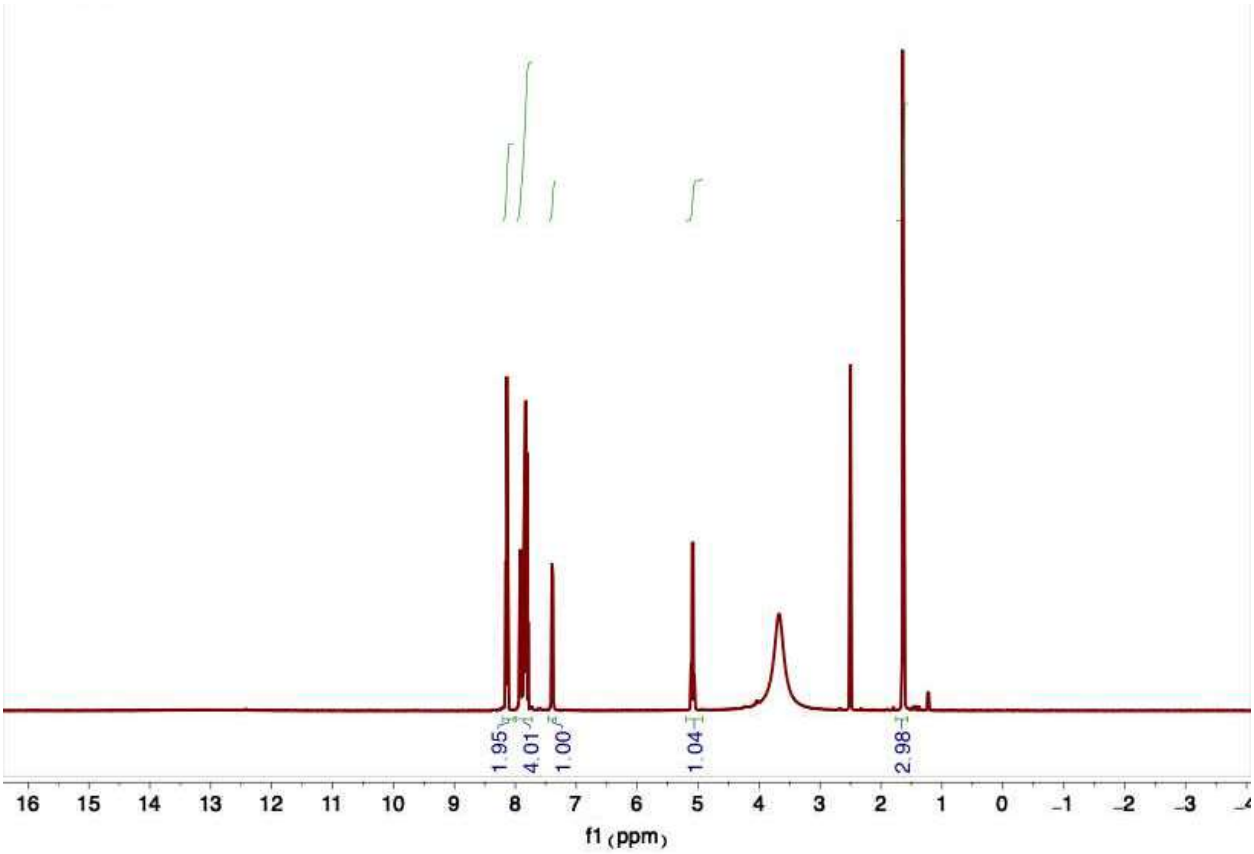

Figure A.5: ^{1}H NMR of 1-2PEAQ in d6-DMSO.

1,4-D2PEAQ (2,2'-((9,10-dioxo-9,10-dihydroanthracene-1,4-diyl)bis(oxy))dipropionic acid)

2g (8.33 mol) of 1,4-dihydroxyanthraquinone was placed in a 50 mL round-bottomed flask with 3 mL of ethyl 2-bromopropionate (23.1 mmol, 2.8 eq) and 3 g of potassium carbonate (21.7 mmol, 2.6 eq) and 12 mL of DMF and stirred for 3 hours at 80 ºC. Water was added until a light brown suspension formed in the solution which was then vacuum filtered. Without further purification or extensive drying, this solid and 3 g of potassium hydroxide was then placed into a 250 mL flask with 30 mL of water and 30 mL of isopropanol and stirred at 80 ºC for 3 hours, at which point a dark solution was observed. 1.3 M HCl was added until an orange precipitate

formed that was then isolated by vacuum filtration. 1.4 g of solid was obtained (43.7% yield). H^1 NMR: 12.99 (b) 8.03 (2H, m), 7.82 (2H, m), 7.36 (2H, b) 4.90 (q, 2H), 1.57 (m, 6H)

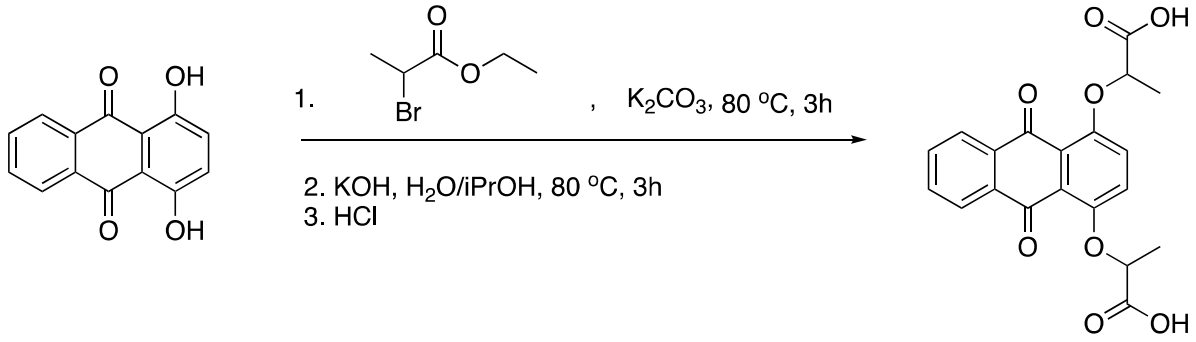

Figure A.6: Synthesis of 1,4-D2PEAQ

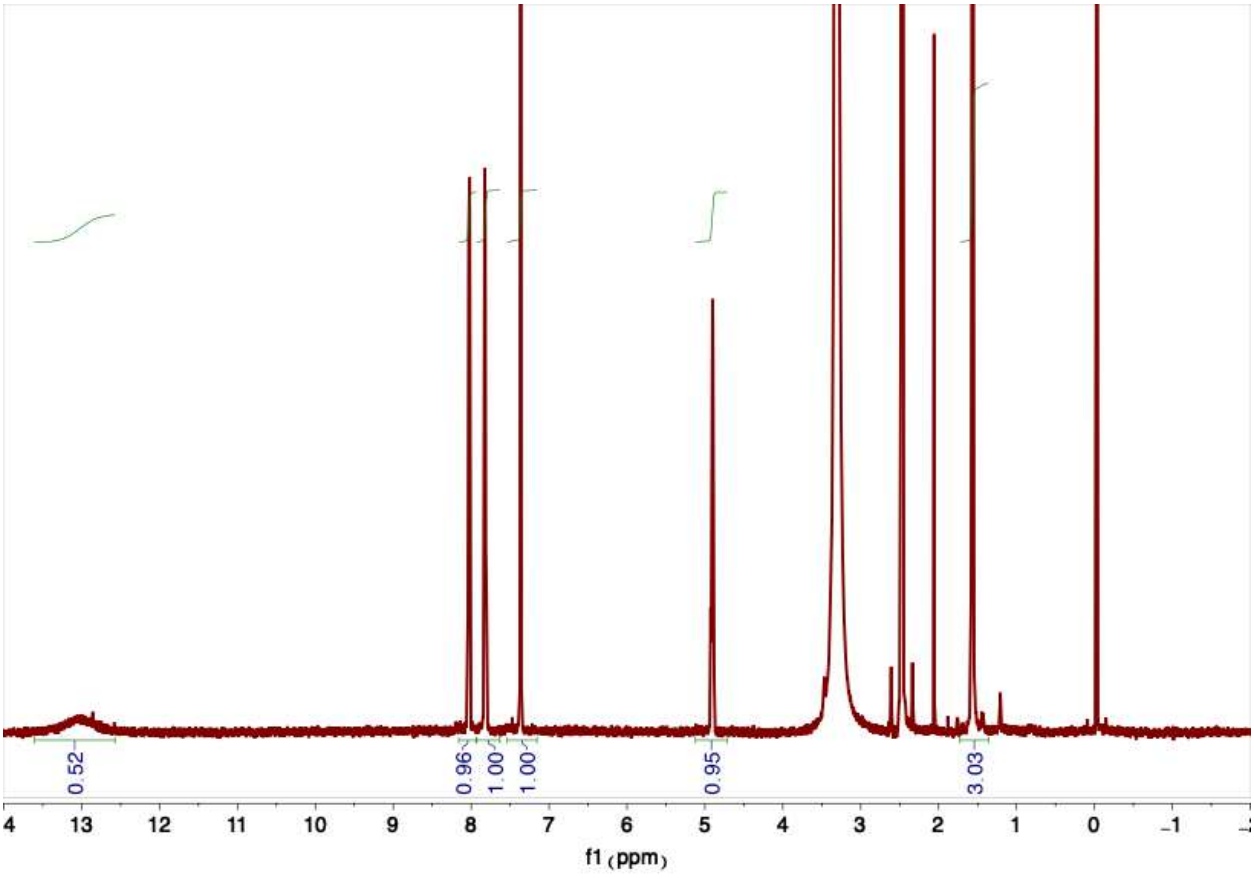

Figure A.7: ^{1}H NMR of 1,4-D2PEAQ in d6-DMSO

1,8-DBEAQ (4,4'-((9,10-dioxo-9,10-dihydroanthracene-1,8-diyl)bis(oxy))dibutyric acid)

2g of 1,8-dihydroxyanthraquinone (8.33 mmol) was mixed with 3 mL of ethyl 4-bromobutyrate (21.0 mmol, 2.5 eq) and 3 g of potassium carbonate (21.7 mmol, 2.6 eq) and stirred at 80 °C for 5 hours followed by allowing the solution to cool while stirring for 2 hours. Water was added until a sandy suspension formed, which was then separated by vacuum filtration. Without further purification, this was then suspended in a solution with 3 g KOH (53.5 mmol, 6.43 eq) with 30 mL of each water and isopropanol for three hours followed by the addition of acetic acid until a yellow precipitate formed and was isolated by vacuum filtration. 1.27 g of a bright yellow solid was obtained (37% yield). H1 NMR: 12.01 (2H, b) 7.72 (2H, m), 7.67 (2H, dd), 7.52 (2H, dd), 4.15 (4H, t), 2.51 (2, 4H), 1.98 (t, 4H)

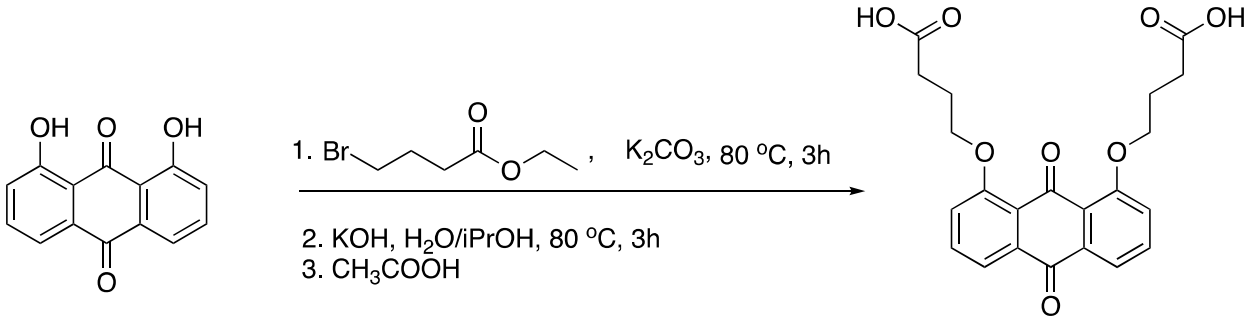

Figure A.8: Synthesis of 1,8-DBEAQ

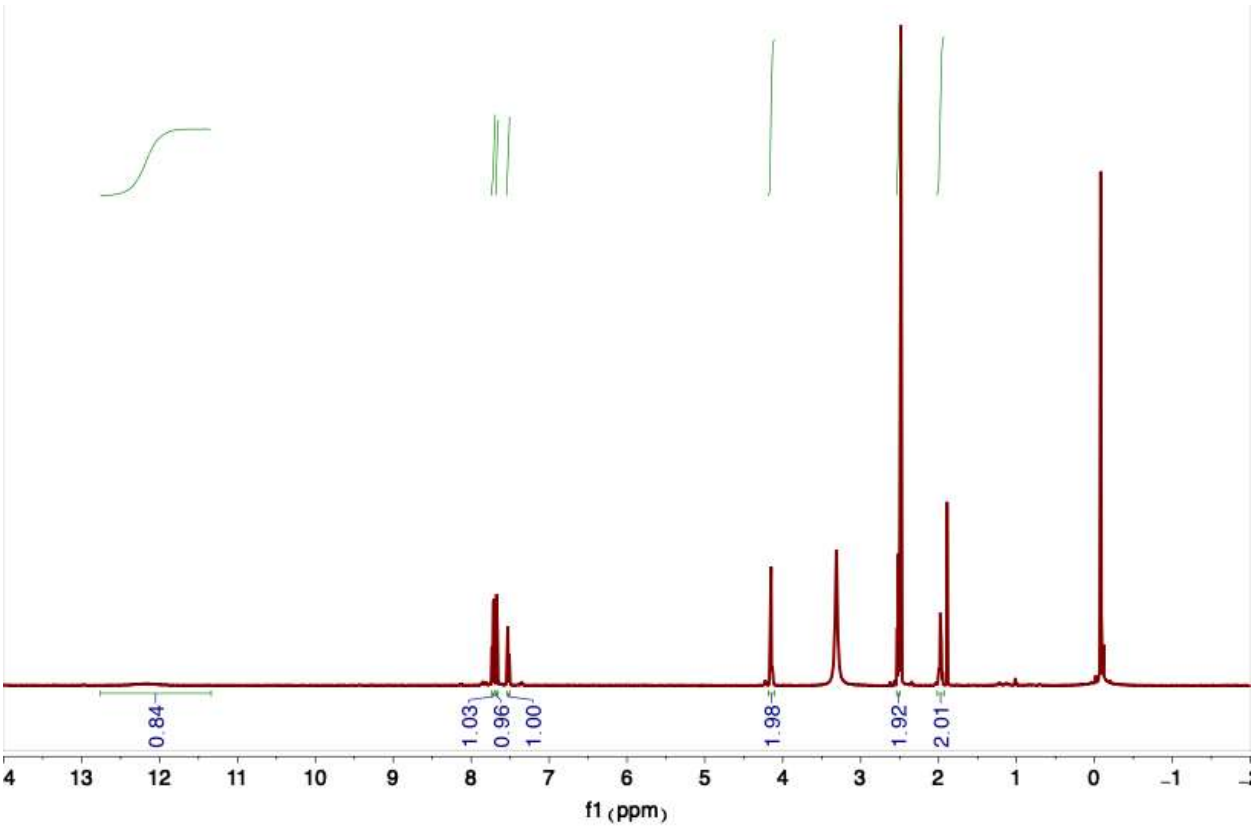

Figure A.9: ^{1}H NMR of 1,8-DBEAQ in d6-DMSO

1,8-D2PEAQ (2,2'-((9,10-dioxo-9,10-dihydroanthracene-1,8- diyl)bis(oxy))dipropionic acid)

1 gram of 1,8-dihydroxyanthraquinone (4.17 mmol) was mixed with 2.3 mL of methyl 2-bromopropionate (20.6 mmol, 4.94 eq) and 1.5 of K_2CO_3 (10.8 mmol, 2.60 eq) in 4 mL of DMF and stirred at 85ºC in a 100 mL round-bottomed flask overnight. A dark precipitate was seen to form and was recovered by vacuum filtration. Without further purification, this compound was mixed with 1.5 g of KOH (26.7 mmol, 6.42 eq) in a 30 mL 50/50 water isopropanol solution and stirred for 5 hours at 85 ºC. After an hour the brown starting material disappeared and was replaced by a dark solution. 1.3 M hydrochloric acid was added to precipitate out a yellow/brown

solid that was isolated by vacuum filtration. 1.5g yield (47% yield). H^1 NMR: 13.13 (2H, b), 7.71 (4H, m), 7.34 (2H, m), 5,00 (2H, m), 1.60 (2H, dd).

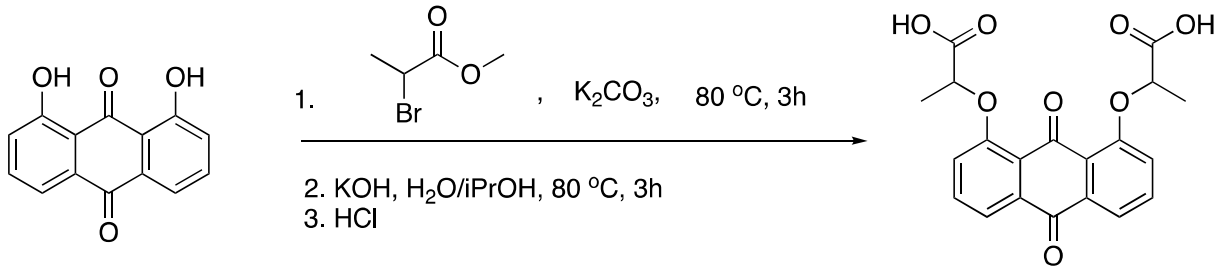

Figure A.10: Synthesis of 1,8-D2PEAQ

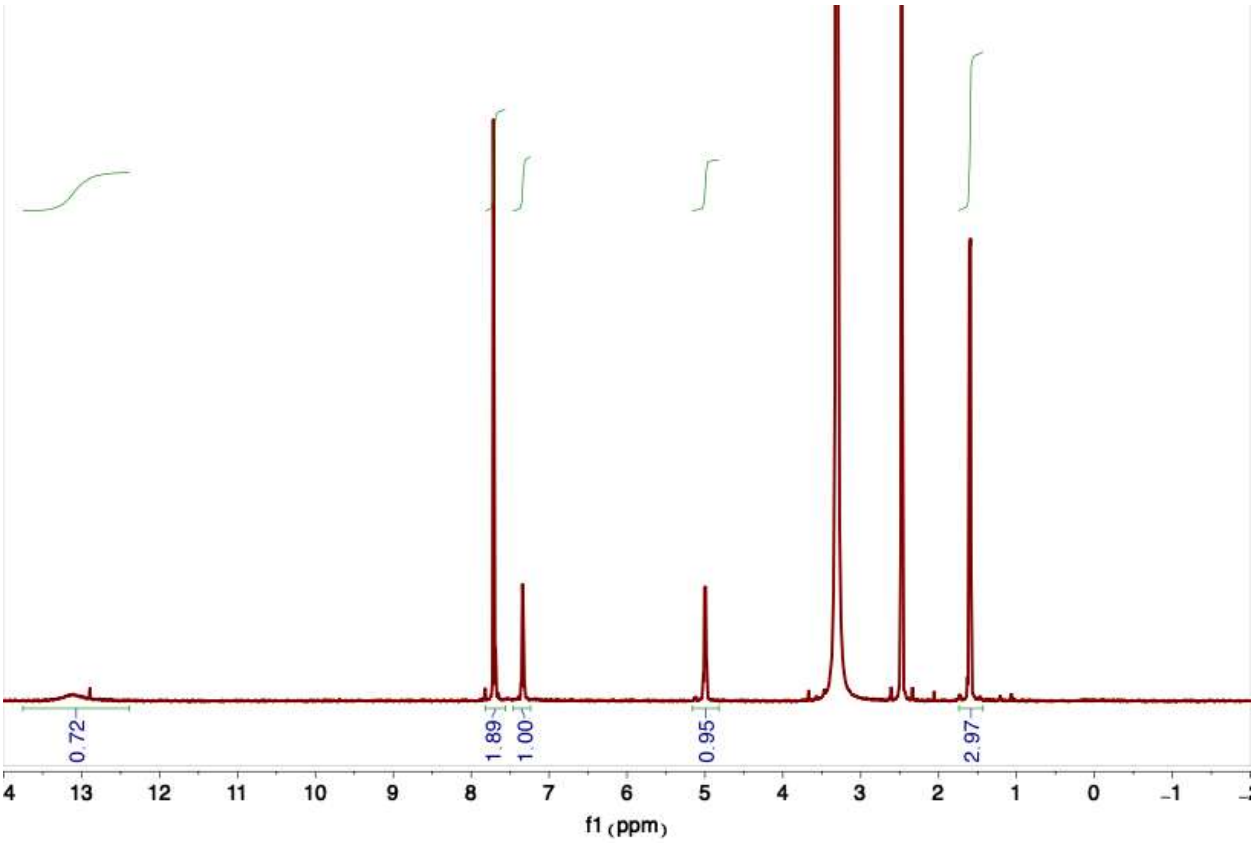

Figure A.11: ^{1}H NMR of 1,8-D2PEAQ in d6-DMSO

1,2-DBEAQ (4,4'-((9,10-dioxo-9,10-dihydroanthracene-1,2-diyl)bis(oxy))dibutyric acid)

1 g of 2,6-dihydroxyanthraquinone (4.2 mmol) was mixed with 2 g of potassium *tert*-butoxide (17.8 mmol, 4.2 eq) and 3 mL of ethyl 4-bromobutyrate (20.9 mmol, 5 eq) in 4 mL of DMF in a 50 mL round-bottomed flask. This solution was stirred at 100 ^{0}C overnight. The solvent was removed and the solids were washed with ~1 M potassium hydroxide solution to remove unreacted starting material. The solid ester was then placed in a round bottom flask with 15 mL of water and 15 mL of isopropanol. 1.5 g KOH (26.8 mmol, 6.5 eq) was added. The solution was stirred at 80 ^{o}C for one hour. 1.3 M HCl solution was added until a bright yellow precipitate formed. The solid was separated by vacuum filtration and 0.3 g were recovered (17.5% yield). H^1 NMR: 8.22 (2H, m), 7.95 (2H, p), 7.74 (1H, d), 7.46 (1H, d), 4.19 (4H, t), 2.44 (4H, t), 2.01 (4H, p)

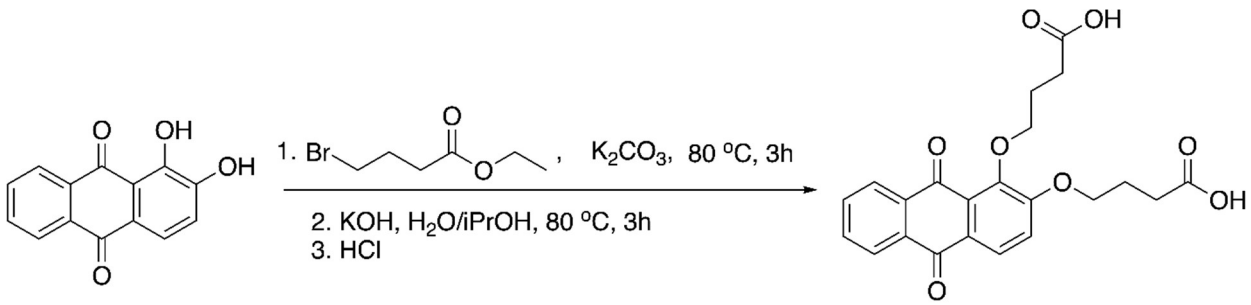

Figure A.12: Synthesis of 1,2-DBEAQ

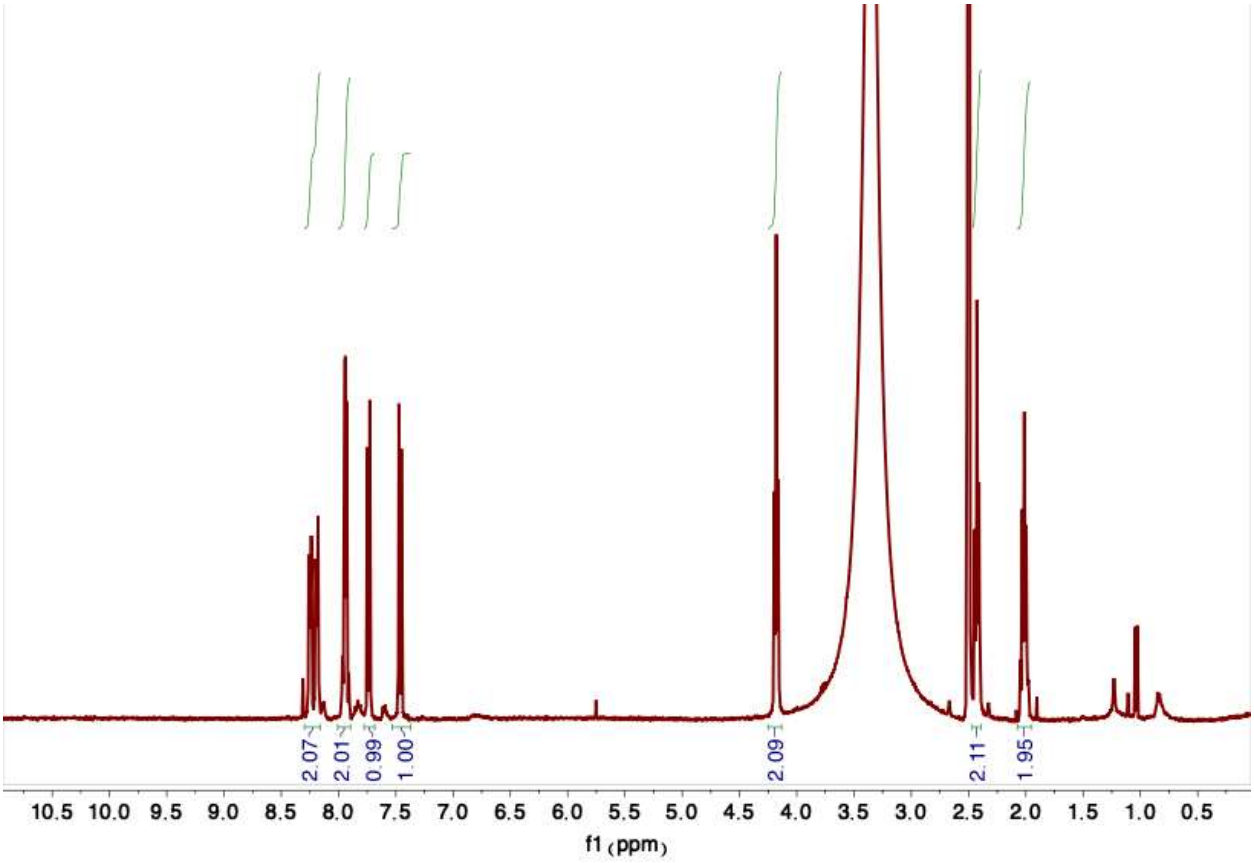

Figure A.13: ^{1}H NMR of 1,2-DBEAQ in d6-DMSO

References

1. *Inventory of U.S. Greenhouse Gas Emissions and Sinks*; Environmental Protection Agency: 2021.

2. Majority of New Renewables Undercut Cheapest Fossil Fuel on Cost. https://www.irena.org/newsroom/pressreleases/2021/Jun/Majority-of-New-Renewables-Undercut-Cheapest-Fossil-Fuel-on-Cost (accessed May 27, 2022).

3. Jones, D. *Global Electricity Review 2022*; Ember: 2022.

4. *Statistical Review of World Energy*; BP: 2021.

5. Ramasamy, V.; Feldman, D.; Desai, J.; Margolis, R. *U.S. Solar Photovoltaic System and Energy Storage Cost Benchmarks: Q1 2021*; NREL: 2021.

6. *Renewable Power Generation in 2017*; Abu Dhabi, 2018.

7. Our World in Data. https://ourworldindata.org/. (accessed May 27, 2022).

8. Rugolo, J.; Aziz, M. J., Electricity storage for intermittent renewable sources. *Energ Environ Sci* **2012,** *5* (5), 7151-7160.

9. U.S. Department of Energy, *U.S. Hydropower Market Report*. **2021**.

10. Cole, W. A.; Frazier, W.; Augustine, C. *Cost Projections for Utility-Scale Battery Storage: 2021 Update*; National Renewable Energy Laboratory: 2021.

11. Lithium-ion batteries need to be greener and more ethical. *The International Journal of Science* **2021**, *595,* **7.**

12. Wu, X.; Song, K.; Zhang, X.; Hu, N.; Li, L.; Li, W.; Zhang, L.; Zhang, H., Safety Issues in Lithium Ion Batteries: Materials and Cell Design. *Frontiers in Energy Research* **2019**, *7*, 65.

13. *Survey Form EIA-860*; U.S. Energy Information Administration: 2019.

14. *Battery Storage in the United States: An Update on Market Trends*; Department of Energy: Washington D.C., 2021.

15. Earth-Rare Diagram of the Zinc-Cerium redox flow battery. https://commons.wikimedia.org/wiki/File:Diagram_of_the_Zinc-Cerium_redox_flow_battery.jpg (accessed May 28, 2022).

16. Aziz, M., Private Communication. 2021.

17. Peacock, B., Another Vanadium Redox Flow Battery To Be Installed In Australia. *PV News* 2020. https://www.pv-magazine.com/2020/12/23/another-vanadium-redox-flow-battery-to-be-installed-in-australia/. (accessed September 4, 2022).

18. Colthorpe, A., 226MWh of vanadium flow batteries on the way for California community energy group CCCE. 2021.

19. Kirk, E. H.; Fenini, F.; Oreiro, S. N.; Bentien, A., Temperature-Induced Precipitation of V2O5 in Vanadium Flow Batteries—Revisited. *Batteries* **2021,** *7* (87).

20. Zeng, Y. K.; Zhao, T. S.; An, L.; Zhou, X. L.; Wei, L., A comparative study of all-vanadium and iron-chromium redox flow batteries for large-scale energy storage. *Journal of Power Sources* **2015,** *300*, 438-443.

21. Vanadium price. *https://www.vanadiumprice.com/ Accessed in April 2021*.

22. Rodby, K. E.; Carney, T. J.; Ashraf Gandomi, Y.; Barton, J. L.; Darling, R. M.; Brushett, F. R., Assessing the levelized cost of vanadium redox flow batteries with capacity fade and rebalancing. *Journal of Power Sources* **2020**.

23. Long Duration Storage Shot. https://www.energy.gov/eere/long-duration-storage-shot. (accessed September 4, 2022)

24. Huskinson, B. T.; Marshak, M. P.; Suh, C.; Er, S.; Gerhardt, M. R.; Galvin, C. J.; Chen, X.; Aspuru-Guzik, A.; Gordon, R. G.; Aziz, M. J., A metal-free organic-inorganic aqueous flow battery. *Nature* **2014,** *505* (7482), 195-8.

25. Lin, K.; Chen, Q.; Gerhardt, M. R.; Tong, L.; Kim, S. B.; Eisenach, L.; Valle, A. W.; Hardee, D.; Gordon, R. G.; Aziz, M. J.; Marshak, M. P., Alkaline quinone flow battery. *Science* **2015,** *349* (6255), 1529-32.

26. Gerhardt, M. R.; Tong, L.; Gomez-Bombarelli, R.; Chen, Q.; Marshak, M. P.; Galvin, C. J.; Aspuru-Guzik, A.; Gordon, R. G.; Aziz, M. J., Anthraquinone Derivatives in Aqueous Flow Batteries. *Adv Energy Mater* **2017,** *7* (8), 1601488.

27. Yang, Z.; Tong, L.; Tabor, D. P.; Beh, E. S.; Goulet, M. A.; De Porcellinis, D.; Aspuru-Guzik, A.; Gordon, R. G.; Aziz, M. J., Alkaline Benzoquinone Aqueous Flow Battery for Large-Scale Storage of Electrical Energy. *Adv Energy Mater* **2018,** *8* (8), 1702056.

28. Cao, J. Y.; Tao, M.; Chen, H. P.; Xu, J.; Chen, Z. D., A highly reversible anthraquinone-based anolyte for alkaline aqueous redox flow batteries. *Journal of Power Sources* **2018,** *386*, 40-46.

29. Kwabi, D. G.; Lin, K.; Ji, Y.; Kerr, E. F.; Goulet, M.-A.; De Porcellinis, D.; Tabor, D. P.; Pollack, D. A.; Aspuru-Guzik, A.; Gordon, R. G.; Aziz, M. J., Alkaline Quinone Flow Battery with Long Lifetime at pH 12. *Joule* **2018,** *2* (9), 1894-1906.

30. Jin, S.; Jing, Y.; Kwabi, D. G.; Ji, Y.; Tong, L.; De Porcellinis, D.; Goulet, M. A.; Pollack, D. A.; Gordon, R. G.; Aziz, M. J., A water-miscible quinone flow battery with high volumetric capacity and energy density. *Acs Energy Lett* **2019,** *4* (6), 1342-1348.

31. Park, M.; Beh, E. S.; Fell, E. M.; Jing, Y.; Kerr, E. F.; De Porcellinis, D.; Goulet, M. A.; Ryu, J.; Wong, A. A.; Gordon, R. G.; Cho, J.; Aziz, M. J., A High Voltage Aqueous Zinc-Organic Hybrid Flow Battery. *Adv Energy Mater* **2019,** *9* (25), 1900694.

32. Hu, B.; Luo, J.; Hu, M.; Yuan, B.; Liu, T. L., A pH-Neutral, Metal-Free Aqueous Organic Redox Flow Battery Employing an Ammonium Anthraquinone Anolyte. *Angew Chem Int Ed* **2019,** *58* (46), 16629-16636.

33. Ji, Y.; Goulet, M. A.; Pollack, D. A.; Kwabi, D. G.; Jin, S.; Porcellinis, D.; Kerr, E. F.; Gordon, R. G.; Aziz, M. J., A Phosphonate-Functionalized Quinone Redox Flow Battery at Near-Neutral pH with Record Capacity Retention Rate. *Adv Energy Mater* **2019,** *9* (12), 1900039.

34. Wu, M.; Jing, Y.; Wong, A. A.; Fell, E. M.; Jin, S.; Tang, Z.; Gordon, R. G.; Aziz, M. J., Extremely stable anthraquinone negolytes synthesized from common precursors. *Chem* **2020,** *6*, 11.

35. Jing, Y.; Wu, M.; Wong, A. A.; Fell, E. M.; Jin, S.; Pollack, D. A.; Kerr, E. F.; Gordon, R. G.; Aziz, M. J., In situ electrosynthesis of anthraquinone electrolytes in aqueous flow batteries. *Green Chemistry* **2020,** *22* (18), 6084-6092.

36. Wang, C. X.; Yang, Z.; Wang, Y. R.; Zhao, P. Y.; Yan, W.; Zhu, G. Y.; Ma, L. B.; Yu, B.; Wang, L.; Li, G. G.; Liu, J.; Jin, Z., High-Performance Alkaline Organic Redox Flow Batteries Based on 2-Hydroxy-3-carboxy-1,4-naphthoquinone. *Acs Energy Lett* **2018,** *3* (10), 2404-2409.

37. Hu, P. F.; Lan, H.; Wang, X.; Yang, Y.; Liu, X. Y.; Wang, H.; Guo, L., Renewable-lawsone-based sustainable and high-voltage aqueous flow battery. *Energy Storage Mater* **2019,** *19*, 62-68.

38. Wu, M.; Bahari, M.; Fell, E.; Gordon, R. G.; Aziz, M. J., High-Performance Anthraquinone with Potentially Low Cost for Aqueous Redox Flow Batteries. *Journal of Materials Chemistry A* **2021,** *9*, 26709-26716.

39. Zhu, Y.; Li, Y.; Qian, Y.; Zhang, L.; Ye, J.; Zhang, X.; Zhao, Y., Anthraquinone-based anode material for aqueous redox flow batteries operating in nondemanding atmosphere. *Journal of Power Sources* **2021,** *501*.

40. Jing, Y.; Fell, E. M.; Wu, M.; Jin, S.; Ji, Y.; Pollack, D. A.; Tang, Z.; Tsukamoto, T.; Gordon, R. G.; Aziz, M. J., Carbon-linked Water-Soluble Anthraquinones Enabled by Heck Cross-Coupling. *submitted* **2021**.

41. Shimizu, A.; Takenaka, K.; Handa, N.; Nokami, T.; Itoh, T.; Yoshida, J. I., Liquid Quinones for Solvent-Free Redox Flow Batteries. *Adv Mater* **2017,** *29* (41), 1606592.

42. Aziz, M. J.; Gordon, R. G.; Lin, K.; Kwabi, D. G.; Ji, X. Quinones Having High Capacity Retention For Use As Electrolytes In Aqueous Redox Flow Batteries. 2021/0009497 A1, 2021.

43. Jing, Y.; Fell, E. M.; Wu, M.; Jin, S.; Ji, Y.; Pollack, D. A.; Tang, Z.; Ding, D.; Bahari, M.; Goulet, M.-A.; Tsukamoto, T.; Gordon, R. G.; Aziz, M. J., Anthraquinone Flow Battery Reactants with Nonhydrolyzable Water-Solubilizing Chains Introduced via a Generic Cross-Coupling Method. *AVD Energy Lett* **2021,** *7* (1), 226-235.

44. Wu, M.; Bahari, M.; Jing, Y.; Amini, K.; Fell, E. M.; George, T. Y.; Gordon, R. G.; Aziz, M. J., Highly Stable Low Redox Potential Quinone for Aqueous Flow Batteries. *Batteries & Supercaps* **2022**, e202200009.

45. Guiheneuf, S.; Godet-Bar, T.; Fontmorin, J. M.; Jourdin, C.; Floner, D.; Geneste, F., A new hydroxyanthraquinone derivative with a low and reversible capacity fading process as negolyte in alkaline aqueous redox flow batteries. *Journal of Power Sources* **2022,** *539*.

46. Xia, L.; Zhang, Y.; Wang, F.; Chu, F.; Yang, Y.; Li, H.; Tan, Z., A Low-Potential and Stable Bis-Dimethylamino Substituted Anthraquinone for pH-Neutral Aqueous Redox Flow Batteries. *ChemElectroChem* **2022**.

47. Pang, S.; Wang, X.; Wang, P.; Ji, Y., Biomimetic Amino Acid Functionalized Phenazine Flow Batteries with Long Lifetime at Near-Neutral pH. *Angew Chem Int Ed* **2021,** *60*, 5289 –5298.

48. Xu, J.; Pang, S.; Wang, X.; Wang, P.; Ji, Y., Ultrastable aqueous phenazine flow batteries with high capacity operated at elevated temperatures. *Joule* **2021**.

49. Wang, C.; Li, X.; Yu, B.; Wang, Y.; Yang, Z.; Wang, H.; Lin, H.; Ma, J.; Li, G.; Jin, Z., Molecular Design of Fused-Ring Phenazine Derivatives for Long-Cycling Alkaline Redox Flow Batteries. *Acs Energy Lett* **2020,** *5* (2), 411-417.

50. Winsberg, J.; Stolze, C.; Muench, S.; Liedl, F.; Hager, M. D.; Schubert, U. S., TEMPO/Phenazine Combi-Molecule: A Redox-Active Material for Symmetric Aqueous Redox-Flow Batteries. *Acs Energy Lett* **2016,** *1* (5), 976-980.

51. Lin, K.; Gomez-Bombarelli, R.; Beh, E. S.; Tong, L.; Chen, Q.; Valle, A.; Aspuru-Guzik, A.; Aziz, M. J.; Gordon, R. G., A redox-flow battery with an alloxazine-based organic electrolyte. *Nat Energy* **2016,** *1* (9), 16102.

52. Wu, W.; Luo, J.; Wang, F.; Yuan, B.; Liu, T. L., A Self-Trapping, Bipolar Viologen Bromide Electrolyte for Redox Flow Batteries. *Acs Energy Lett* **2021**, 2891-2897.

53. Ohira, A.; Funaki, T.; Ishida, E.; Kim, J.-D.; Sato, Y., Redox-Flow Battery Operating in Neutral and Acidic Environments with Multielectron-Transfer-Type Viologen Molecular Assembly. *ACS Applied Energy Materials* **2020,** *3* (5), 4377-4383.

54. Liu, Y.; Li, Y.; Zuo, P.; Chen, Q.; Tang, G.; Sun, P.; Yang, Z.; Xu, T., Screening Viologen Derivatives for Neutral Aqueous Organic Redox Flow Batteries. *ChemSusChem* **2020**.

55. Jin, S.; Fell, E. M.; Vina-Lopez, L.; Jing, Y.; Michalak, P. W.; Gordon, R. G.; Aziz, M. J., Near Neutral pH Redox Flow Battery with Low Permeability and Long-Lifetime Phosphonated Viologen Active Species. *Adv Energy Mater* **2020,** *10* (20), 2000100.

56. Yu, X. W.; Manthiram, A., A strategically managed rechargeable battery system with a neutral methyl viologen anolyte and an acidic air-cathode enabled by a mediator-ion solid electrolyte. *Sustain Energ Fuels* **2018,** *2* (7), 1452-1457.

57. Liu, T. B.; Wei, X. L.; Nie, Z. M.; Sprenkle, V.; Wang, W., A Total Organic Aqueous Redox Flow Battery Employing a Low Cost and Sustainable Methyl Viologen Anolyte and 4-HO-TEMPO Catholyte. *Adv Energy Mater* **2015,** *6* (3), 1501449.

58. Janoschka, T.; Morgenstern, S.; Hiller, H.; Friebe, C.; Wolkersdorfer, K.; Haupler, B.; Hager, M. D.; Schubert, U. S., Synthesis and characterization of TEMPO- and viologen-polymers for water-based redox-flow batteries. *Polym Chem-Uk* **2015,** *6* (45), 7801-7811.

59. Winsberg, J.; Janoschka, T.; Morgenstern, S.; Hagemann, T.; Muench, S.; Hauffman, G.; Gohy, J. F.; Hager, M. D.; Schubert, U. S., Poly(TEMPO)/Zinc Hybrid-Flow Battery: A Novel, "Green," High Voltage, and Safe Energy Storage System. *Adv Mater* **2016,** *28* (11), 2238-43.

60. Winsberg, J.; Stolze, C.; Schwenke, A.; Muench, S.; Hager, M. D.; Schubert, U. S., Aqueous 2,2,6,6-Tetramethylpiperidine-N-oxyl Catholytes for a High-Capacity and High Current Density Oxygen-Insensitive Hybrid-Flow Battery. *Acs Energy Lett* **2017,** *2* (2), 411-416.

61. Li, Y.; Xu, Z.; Liu, Y.; Jin, S.; Fell, E. M.; Wang, B.; Gordon, R. G.; Aziz, M. J.; Yang, Z.; Xu, T., Functioning water-insoluble ferrocenes for aqueous organic flow battery via host-guest inclusion. *ChemSusChem* **2020**.

62. Zhao, Z.; Zhang, B.; Schrage, B. R.; Ziegler, C. J.; Boika, A., Investigations Into Aqueous Redox Flow Batteries Based on Ferrocene Bisulfonate. *ACS Applied Energy Materials* **2020,** *3* (10), 10270-10277.

63. Yu, J.; Salla, M.; Zhang, H.; Ji, Y.; Zhang, F.; Zhou, M.; Wang, Q., A robust anionic sulfonated ferrocene derivative for pH-neutral aqueous flow battery. *Energy Storage Mater* **2020,** *29*, 216-222.

64. Hu, B.; DeBruler, C.; Rhodes, Z.; Liu, T. L., Long-Cycling Aqueous Organic Redox Flow Battery (AORFB) toward Sustainable and Safe Energy Storage. *J Am Chem Soc* **2017,** *139* (3), 1207-1214.

65. Hudnall, P. M., Hydroquinone. In *Ullmann's Encyclopedia of Industrial Chemistry*, Wiley: 2000.

66. Anand, A. Respiratory quinone diversification to rise to the challenge. https://microbiologycommunity.nature.com/posts/56749-respiratory-quinone-diversification-to-rise-to-the-challenge.

67. Bien, H.-S.; Stawitz, J.; Wunderlich, K., Anthraquinone Dyes and Intermediates. In *Ullmann's Encyclopedia of Industrial Chemistry*, 2000.

68. Hattori, M., Dyes, Anthraquinone. In *Kirk-Othmer Encyclopedia of Chemical Technology*, 2004.

69. Goulet, M. A.; Tong, L.; Pollack, D. A.; Tabor, D. P.; Odom, S. A.; Aspuru-Guzik, A.; Kwan, E. E.; Gordon, R. G.; Aziz, M. J., Correction to "Extending the Lifetime of Organic Flow Batteries via Redox State Management". *J. Am. Chem. Soc.* **2021,** *143*, 14019-14020.

70. Goulet, M. A.; Tong, L.; Pollack, D. A.; Tabor, D. P.; Odom, S. A.; Aspuru-Guzik, A.; Kwan, E. E.; Gordon, R. G.; Aziz, M. J., Extending the Lifetime of Organic Flow Batteries via Redox State Management. *J Am Chem Soc* **2019,** *141* (20), 8014-8019.

71. Yang, B.; Murali, A.; Nirmalchandar, A.; Jayathilake, B.; Prakash, G. K. S.; Narayanan, S. R., A Durable, Inexpensive and Scalable Redox Flow Battery Based on Iron Sulfate and Anthraquinone Disulfonic Acid. *Journal of The Electrochemical Society* **2020,** *167* (6).

72. Huskinson, B. T.; Marshak, M. P.; Gerhardt, M. R.; Aziz, M. J., Cycling of a Quinone-Bromide Flow Battery for Large-Scale Electrochemical Energy Storage. *ECS Transactions* **2014,** *61* (37), 27-30.

73. Chen, Q.; Eisenach, L.; Aziz, M. J., Cycling Analysis of a Quinone-Bromide Redox Flow Battery. *Journal of the Electrochemical Society* **2016,** *163* (1), A5057-A5063.

74. Hoober-Burkhardt, L.; Krishnamoorthy, S.; Yang, B.; Murali, A.; Nirmalchandar, A.; Prakash, G. K. S.; Narayanan, S. R., A New Michael-Reaction-Resistant Benzoquinone for Aqueous Organic Redox Flow Batteries. *Journal of the Electrochemical Society* **2017,** *164* (4), A600-A607.

75. Tong, L.; Goulet, M.-A.; Tabor, D. P.; Kerr, E. F.; De Porcellinis, D.; Fell, E. M.; Aspuru-Guzik, A.; Gordon, R. G.; Aziz, M. J., Molecular Engineering of an Alkaline Naphthoquinone Flow Battery. *Acs Energy Lett* **2019,** *4* (8), 1880-1887.

76. Sun, P.; Liu, Y. H.; Li, Y. Y.; Shehzad, M. A.; Liu, Y. Z.; Zuo, P. P.; Chen, Q. R.; Yang, Z. J.; Xu, T. W., 110th Anniversary: Unleashing the Full Potential of Quinones for High Performance Aqueous Organic Flow Battery. *Ind Eng Chem Res* **2019,** *58* (10), 3994-3999.

77. Zhang, S.; Li, X.; Chu, D. D., An Organic Electroactive Material for Flow Batteries. *Electrochim Acta* **2016,** *190*, 737-743.

78. Liu, Y. Y.; Lu, S. F.; Chen, S.; Wang, H. N.; Zhang, J.; Xiang, Y., A Sustainable Redox Flow Battery with Alizarin-Based Aqueous Organic Electrolyte. *Acs Applied Energy Materials* **2019,** *2* (4), 2469-2474.

79. Gavezzotti, A.; Rizzato, S., Are Racemic Crystals Favored over Homochiral Crystals by Higher Stability or by Kinetics? Insights from Comparative Studies of Crystalline Stereoisomers. *Journal of Organic Chemistry* **2014,** *79* (11), 4809–4816.

80. Ornella E. Y. Kilinkissa, O. E. Y.; Govender, K. K.; Báthori, N. B., Melting point–solubility–structure correlations in chiral and racemic model cocrystals. *CrystEngComm* **2020,** *22*, 2766–2771.

81. Kwabi, D. G.; Ji, Y.; Aziz, M. J., Electrolyte lifetime in aqueous organic redox flow batteries: A critical review. *Chem. Rev.* **2020,** *120* (14), 6467–6489.

82. Vercillo, P.; Trant, C.; Gilespie, M., Solubility of Sodium Ferrocyanide in Sodium Hydroxide and Potassium Ferrocyanide in Potassium Hydroxide. University of Rochester, 2011.

83. Esswein, A. J.; Goeltz, J.; Amadeo, D. High Solubility Iron Hexacyanides. Application 2014/0051003 A1, 2/20/2014, 2014.

84. Bard, A. J.; Faulkner, L. R., *Electrochemical methods : fundamentals and applications / Allen J. Bard, Larry R. Faulkner, Department of Chemistry and Biochemistry, University of Texas at Austin*. Second edition. ed.; John Wiley & Sons, Inc.: Hoboken, NJ, 2001.

85. Hollas, A.; Wei, X. L.; Murugesan, V.; Nie, Z. M.; Li, B.; Reed, D.; Liu, J.; Sprenkle, V.; Wang, W., A biomimetic high-capacity phenazine-based anolyte for aqueous organic redox flow batteries. *Nat Energy* **2018,** *3* (6), 508-514.

86. Luo, J.; Hu, B.; Debruler, C.; Liu, T. L., A pi-Conjugation Extended Viologen as a Two-Electron Storage Anolyte for Total Organic Aqueous Redox Flow Batteries. *Angew Chem Int Ed* **2018,** *57* (1), 231-235.

87. Hu, B.; Tang, Y.; Luo, J.; Grove, G.; Guo, Y.; Liu, T. L., Improved radical stability of viologen anolytes in aqueous organic redox flow batteries. *Chem Commun* **2018,** *54* (50), 6871-6874.

88. DeBruler, C.; Hu, B.; Moss, J.; Liu, X. A.; Luo, J. A.; Sun, Y. J.; Liu, T. L., Designer Two-Electron Storage Viologen Anolyte Materials for Neutral Aqueous Organic Redox Flow Batteries. *Chem* **2017,** *3* (6), 961-978.

89. Liu, X.; Zhang, X.; Li, G.; Zhang, S.; Zhang, B.; Ma, W.; Wang, Z.; Zhang, Y.; He, G., Thienoviologen anolytes for aqueous organic redox flow batteries with simultaneously enhanced capacity utilization and capacity retention. *Journal of Materials Chemistry A* **2022**.

90. Liu, B.; Tang, C. W.; Jiang, H.; Guocheng, J.; Zhao, T., An aqueous organic redox flow battery employing a trifunctional electroactive compound as anolyte, catholyte and supporting electrolyte. *Journal of Power Sources* **2020**.

91. Lai, Y. Y.; Li, X.; Liu, K.; Tung, W.-Y.; Cheng, C.-F.; Zhu, Y., Stable Low-Cost Organic Dye Anolyte for Aqueous Organic Redox Flow Battery. *ACS Applied Energy Materials* **2020,** *3* (3), 2290-2295.

92. Huang, J. H.; Yang, Z.; Murugesan, V.; Walter, E.; Hollas, A.; Pan, B. F.; Assary, R. S.; Shkrob, I. A.; Wei, X. L.; Zhang, Z. C., Spatially Constrained Organic Diquat Anolyte for Stable Aqueous Flow Batteries. *Acs Energy Lett* **2018,** *3* (10), 2533-2538.

93. Orita, A.; Verde, M. G.; Sakai, M.; Meng, Y. S., A biomimetic redox flow battery based on flavin mononucleotide. *Nat Commun* **2016,** *7*, 13230.

94. Janoschka, T.; Martin, N.; Hager, M. D.; Schubert, U. S., An Aqueous Redox-Flow Battery with High Capacity and Power: The TEMPTMA/MV System. *Angew Chem Int Ed Engl* **2016,** *55* (46), 14427-14430.

95. Luo, J.; Wu, W. D.; Debruler, C.; Hu, B.; Hu, M. W.; Liu, T. L., A 1.51 V pH neutral redox flow battery towards scalable energy storage. *Journal of Materials Chemistry A* **2019,** *7* (15), 9130-9136.

96. Chen, Q.; Li, Y.; Liu, Y.; Sun, P.; Yang, Z.; Xu, T., Designer Ferrocene Catholyte for Aqueous Organic Flow Batteries. *ChemSusChem* **2020**.

97. Feng, R.; Zhang, X.; Murugesan, V.; Hollas, A.; Chen, Y.; Shao, Y.; Walter, E.; Wellala, N. P. N.; Yan, L.; Rosso, K. M.; Wang, W., Reversible ketone hydrogenation and dehydrogenation for aqueous organic redox flow batteries. *Science* **2021,** *372* (6544), 836-840.

98. Wu, M.; Bahari, M.; Jing, Y.; Amini, K.; Fell, E. M.; George, T. Y.; Gordon, R. G.; Aziz, M. J., Highly stable low redox potential quinone for aqueous flow batteries. *ChemRxiv* **2021**, https://doi.org/10.26434/chemrxiv-2021-rjzdn.

99. Tang, G.; Liu, Y.; Li, Y.; Peng, K.; Zuo, P.; Yang, Z.; Xu, T., Designing Robust Two-Electron Storage Extended Bipyridinium Anolytes for pH-Neutral Aqueous Organic Redox Flow Batteries. *JACS Au* **2022,** *2* (5), 1214-1222.

100. Brushett, F. R.; Aziz, M. J.; Rodby, K. E., On lifetime and cost of redox-active organics for aqueous flow batteries. *Acs Energy Lett* **2020,** *5*, 879-884.

101. Mehta, B.; Bhardwaj, S., Microwave induced synthesis of anthraquinone derivatives a solvent free path. *Rasayan Journal of Chemistry* **2009,** *2*, 659-661.

102. Li, Y.; Guo, F.; Chen, T.; Zhang, L.; Wang, Z.; Su, Q.; Feng, L., Design, Synthesis, Molecular Docking, and Biological Evaluation of New Emodin Anthraquinone Derivatives as Potential Antitumor Substances. *Chem. Biodivers* **2020,** *17* (9).

103. Zheng, J.; Zheng, Y.-j.; Wan, X.-h.; Wang, Z. Y., Visible and near-infrared chiroptical gels containing electrochromic anthraquinone imide groups. *Chinese Journal of Polymer Science* **2012,** *30* (2), 328-336.

104. Mukkamala, R.; Weiss, R. G., Physical Gelation of Organic Fluids by Anthraquinone−Steroid-Based Molecules. Structural Features Influencing the Properties of Gels. *Langmuir* **1996,** *12* (6), 1474-1482.

105. Mukkamala, R.; Weiss, R. G., Anthraquinone–steroid based gelators of alcohols and alkanes. *Journal of the Chemical Society, Chemical Communications* **1995,** (3), 375-376.

106. Mondal, S.; Ghosh, K., Anthraquinone Derived Cholesterol Linked Imidazole Gelator in Visual Sensing of Picric Acid. *ChemSelect 2017*.

107. Ostuni, E.; Kamaras, P.; Weiss, R. G., Novel X-ray Method for In Situ Determination of Gelator Strand Structure: Polymorphism of Cholesteryl Anthraquinone-2-carboxylate†. *ACIE* **1996,** *35* (12), 1324-1326.

108. Džolić, Z.; Cametti, M.; Dalla Cort, A.; Mandolini, L.; Žinić, M., Fluoride-responsive organogelator based on oxalamide-derived anthraquinone. *Chemical Communications* **2007,** (34), 3535-3537.

109. Cametti, M.; Cetina, M.; Džolić, Z., Cu(ii)-specific metallogel formation by an amido-anthraquinone-pyridyloxalamide ligand in DMSO–water. *Dalton Transactions* **2015,** *44* (16), 7223-7229.

110. Jones, S. L.; Wong, K. H.; Thordarson, P.; Ladouceur, F., Self-assembling electroactive hydrogels for flexible display technology. *Journal of Physics: Condensed Matter* **2010,** *22* (49), 494105.

111. Zheng, J.; Fan, R.; Wu, H.; Yao, H.; Yan, Y.; Liu, J.; Ran, L.; Sun, Z.; Yi, L.; Dang, L.; Gan, P.; Zheng, P.; Yang, T.; Zhang, Y.; Tang, T.; Wang, Y., Directed self-assembly of

herbal small molecules into sustained release hydrogels for treating neural inflammation. *Nature Communications* **2019,** *10* (1), 1604.

112. Du, X.; Zhou, J.; Shi, J.; Xu, B., Supramolecular Hydrogelators and Hydrogels: From Soft Matter to Molecular Biomaterials. *Chem. Rev.* **2015,** *115* (24), 13165-13307.

113. Zhang, J.; Hu, Y.; Li, Y., *Gel Chemistry: Interactions, Structures and Properties* Springer Singapore: 2018.

114. Wehner, L. A.; Mittal, N.; Liu, T.; Niederberger, M., Multifunctional Batteries: Flexible, Transient, and Transparent. *ACS Central Science* **2021,** *7* (2), 231-244.

115. Bandodkar, A. J.; Jeerapan, I.; Wang, J., Wearable Chemical Sensors: Present Challenges and Future Prospects. *ACS Sensors* **2016,** *1* (5), 464-482.

116. Guo, Y.; Bae, J.; Fang, Z.; Li, P.; Zhao, F.; Yu, G., Hydrogels and Hydrogel-Derived Materials for Energy and Water Sustainability. *Chem. Rev.* **2020,** *120* (15), 7642-7707.

117. Shen, W.; Li, K.; Lv, Y.; Xu, T.; Wei, D.; Liu, Z., Highly-Safe and Ultra-Stable All-Flexible Gel Polymer Lithium Ion Batteries Aiming for Scalable Applications. *Adv Energy Mater* **2020,** *10* (21).

118. Tan, M. J.; Li, B.; Chee, P.; Ge, X.; Liu, Z.; Zong, Y.; Loh, X. J., Acrylamide-derived freestanding polymer gel electrolyte for flexible metal-air batteries. *Journal of Power Sources* **2018,** *400*, 566-571.

119. Zuo, Y.; Wang, K.; Wei, M.; Zhao, S.; Zhang, P.; Pei, P., Starch gel for flexible rechargeable zinc-air batteries. *Cell Reports Physical Science* **2022,** *3* (1), 100687.

120. Wei, D.; Shen, W.; Xu, T.; Li, K.; Yang, L.; Zhou, Y.; Zhong, M.; Yang, F.; Xu, X.; Wang, Y.; Zheng, M.; Zhang, Y.; Li, Q.; Yong, Z.; Li, H.; Wang, Q., Ultra-flexible and foldable gel polymer lithium–ion batteries enabling scalable production. *Materials Today Energy* **2022,** *23*, 100889.

121. Crespilho, F. N.; Sedenho, G. C.; De Porcellinis, D.; Kerr, E.; Granados-Focil, S.; Gordon, R. G.; Aziz, M. J., Non-corrosive, low-toxicity gel-based microbattery from organic and organometallic molecules. *Journal of Materials Chemistry A* **2019,** *7* (43), 24784-24787.

122. Luo, N.; Dai, W.; Li, C.; Zhou, Z.; Lu, L.; Poon, C. C. Y.; Chen, S.-C.; Zhang, Y.; Zhao, N., Flexible Piezoresistive Sensor Patch Enabling Ultralow Power Cuffless Blood Pressure Measurement. *Advanced Functional Materials* **2016,** *26* (8), 1178-1187.

123. Guo, Y.; Zhong, M.; Fang, Z.; Wan, P.; Yu, G., A Wearable Transient Pressure Sensor Made with MXene Nanosheets for Sensitive Broad-Range Human–Machine Interfacing. *Nano Letters* **2019,** *19* (2), 1143-1150.

124. Zhan, Z.; Lin, R.; Tran, V.-T.; An, J.; Wei, Y.; Du, H.; Tran, T.; Lu, W., Paper/Carbon Nanotube-Based Wearable Pressure Sensor for Physiological Signal Acquisition and Soft Robotic Skin. *ACS Applied Materials & Interfaces* **2017,** *9* (43), 37921-37928.

125. Liu, M.; Pu, X.; Jiang, C.; Liu, T.; Huang, X.; Chen, L.; Du, C.; Sun, J.; Hu, W.; Wang, Z. L., Large-Area All-Textile Pressure Sensors for Monitoring Human Motion and Physiological Signals. *Advanced Materials* **2017,** *29* (41), 1703700.

126. Wang, X.; Wang, P. H. P.; Cao, Y.; Mercier, P. P., A 0.6V 75nW All-CMOS Temperature Sensor With 1.67m°C/mV Supply Sensitivity. *IEEE Transactions on Circuits and Systems I: Regular Papers* **2017,** *64* (9), 2274-2283.

127. Lin, K. Organic Molecule-based Electrolyte Materials for Aqueous Redox Flow Battery. Harvard University, http://nrs.harvard.edu/urn-3:HUL.InstRepos:39987931, 2017.

128. Benkhaya, S.; M' rabet, S.; El Harfi, A., A review on classifications, recent synthesis and applications of textile dyes. *Inorganic Chemistry Communications* **2020,** *115*, 107891.

129. Dapson, R., The history, chemistry and modes of action of carmine and related dyes. *Biotechnic & Histochemistry* **2007,** *82* (4-5), 173-187.

130. Gorbunova, S. A. Electrochemical characterization of carminic acid towards the use as an electrochemical molecular beacon for nucleic acid detection. University of British Columbia 2011.

131. Sedenho, G. C.; De Porcellinis, D.; Jing, Y.; Kerr, E.; Mejia-Mendoza, L. M.; Vazquez-Mayagoitia, Á.; Aspuru-Guzik, A.; Gordon, R. G.; Crespilho, F. N.; Aziz, M. J., Effect of Molecular Structure of Quinones and Carbon Electrode Surfaces on the Interfacial Electron Transfer Process. *ACS Applied Energy Materials* **2020,** *3* (2), 1933-1943.

132. Mehandale, A. R.; Rao, A. V. R.; Shaikh, I. N.; Venkataraman, K., Desoxyerythrolaccin and laccaic acid D. *Tetrahedron Letters* **1968,** *9* (18), 2231-2234.

133. Wouters, J.; Verhecken, A., The chemical nature of flavokermesic acid. *Tetrahedron Letters* **1987,** *28* (11), 1199-1202.

134. Orska-Gawryś, J.; Surowiec, I.; Kehl, J.; Rejniak, H.; Urbaniak-Walczak, K.; Trojanowicz, M., Identification of natural dyes in archeological Coptic textiles by liquid chromatography with diode array detection. *Journal of Chromatography A* **2003,** *989* (2), 239-248.

135. Kongkachuichay, P.; Shitangkoon, A.; Chinwongamorn, N., Thermodynamics of adsorption of laccaic acid on silk. *Dyes and Pigments* **2002,** *53* (2), 179-185.